Shaping Nanostructure Using Molecules

Shih-Hsuan Hung

PhD

University of York

Department of Physics

December 2018

Abstract

Metallic nanoparticles are widely used for technological applications in catalysis, data storage and medicine. There are many experimental and theoretical investigations studying promising materials for new applications and understanding how they work. A number of strategies are also employed to improve performance for specific applications including doping, annealing and chemical processing. In this thesis we have investigated the influence of external factors (such as adsorbed molecules or substrate materials) on the structure and properties of four different nanoparticle systems. First, we have investigated the morphology of $L1_0$ ordered FePt nanoparticles supported on various $Mg_{(1-x)}Ti_xO$ substrates. The adhesion energy between FePt and the MgTiO slabs is found to decrease with the increasing number of TiO layers due to Ti-Fe bond formation. In addition, the Fe-Ti interaction hinders the growth of the FePt nanoparticle in [001] direction and reduces the density of information storage. Next, we have studied the oxidation of Ti and TiPt nanoparticles. We find oxygen atoms should adsorb on the three-fold follow sites on Ti nanoparticles and linear O_{ads}-Ti-O_{ads} structures minimise the adsorption energy. Increasing oxygen coverage leads an increase of surface strain on the Ti nanoparticle. For each 1 % increase in surface strain the energy barrier for subsurface oxygen diffusion in the middle of the facets decreases by 0.1 eV. Oxidation of TiPt nanoparticles results in an atomic rearrangement of the bimetallic nanoparticle that can be controlled by the oxygen coverage. With increased oxygen adsorption, the atomic arrangement transforms from Pt atoms segregated to the vertices to a core-shell configuration. Finally, we have investigated Au nanoparticles supported on ZnO nanorods for CO oxidation. We demonstrate zinc interstitials in bulk ZnO can lead to the formation of a ZnO encapsulation layer around the Au nanoparticles under oxygen-rich conditions. Moreover, the ZnO encapsulation provides alternative adsorption sites for oxygen molecules and further increases the number of possible reaction pathways for CO oxidation, explaining the experimentally observed enhanced activity.

Contents

List of Tables

List of Figures

Acknowledgements

My deepest gratitude goes first and foremost to Dr Keith McKenna, my supervisor, for his constant encouragement and guidance. He has helped me through all the stages of the writing of this thesis. Without his consistent instruction, this thesis could not have been completed. Second, I would like to express my heartfelt gratitude to my parents, Benjamin, Chien-Jyun and Mickey for the unconditional support and encouragement. I am also greatly indebted to my colleagues in room N005, Adam, Claudio, James, Jia, John, Jonathan, and Razak, for every discussion and their company. I would like to thank administration staff and IT service at Department of Physics at University of York. Finally, I would like to acknowledge funding from the EPSRC for the Polaris supercomputer at the University of Leeds and ARCHER at the University of Edinburgh.

Declaration

I declare that this thesis is a presentation of original work and I am the sole author. This work has not previously been presented for an award at this, or any other, University. All sources are acknowledged.

Publications

The content of this thesis is based on the following published papers. The results in Chapter 4 are published in the first paper which discusses the change in morphology of granular FePt on different MgTiO substrates. The results in Chapter 5 are published in the second and third papers. The former one investigates the oxidation of Ti nanoparticles and the latter studies the atomic arrangement of bimetallic TiPt nanoparticles for different amounts of oxygen adsorbed on(in) the nanoparticle. The results in Chapter 6 are currently being written up for publication.

1. Shih-Hsuan Hung and Keith P. McKenna, "First-principles prediction of the morphology of $L1_0$ FePt nanoparticles supported on Mg(Ti)O for heat-assisted magnetic recording applications," Phys. Rev. Mat., **1**, 024405, (2017)

2. Shih-Hsuan Hung and Keith P. McKenna, "First principles investigation of titanium nanoparticle oxidation," J. Phys. Chem. C, **122**, 3107-3114, (2018)

3. Saeed Gholhaki, Shih-Hsuan Hung, David J. H. Cant, Caroline E. Blackmore, Alex G. Shard, Quanmin Guo, Keith P. McKenna and Richard E. Palmer, "Exposure of mass-selected bimetallic Pt-Ti to oxygen explored using the scanning transmission electron microscopy and density functional theory," RSC Adv., **8**, 27276-27282, (2018)

Chapter 1

Introduction

1.1 Nanostructure

Metallic nanoparticles are widely used for applications such as magnetic recording, catalysis, solar energy and surface coatings [1, 2]. Due to their reduced size and high surface-to-volume ratio, nanoparticles exhibit different physical and chemical properties compared to materials in the bulk phase. For example, Au nanoparticles have been well-studied and demonstrate size and shape dependant optical properties [3]. The most stable configurations of metallic nanoparticles are dependent on the atomic composition and the number of atoms in nanoparticle. Fig. 1.1 shows the general trend of the morphology with respect to different sizes of metallic nanoparticles in the range from $N = 10$ to $N = 10^5$, where N is the number of atoms in nanoparticle [4]. Common morphologies of nanoparticles can be categorised into three types: icosahedron, decahedron and octahedron. Icosahedral nanoparticles are often stable in the range of $N \leq 10^2$, and consist of twenty (111) facets with 12 vertices. For larger nanoparticles the decahedral morphology becomes more stable, which includes ten (111) facets with 7 vertices. Both icosahedral and decahedral morphologies are non-crystalline, with twin boundaries inside the nanoparticle and volume-dependent strain. For larger sizes the octahedral morphology becomes the most stable, which consists of single crystalline face-centred cubic (fcc) structure without any internal boundaries. Besides these morphologies, there are many variants with different terminations, such as Ino-decahedral, Marks-decahedral and truncated-octahedral shapes.

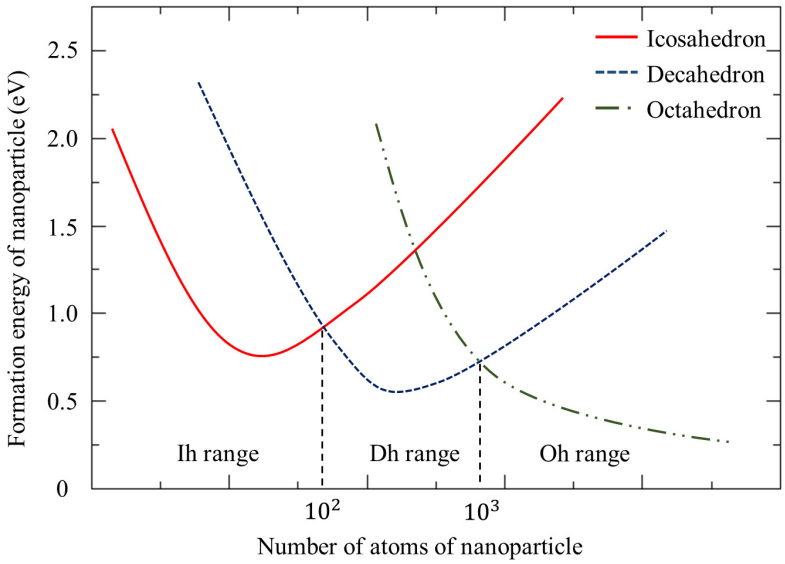

Figure 1.1: Formation energy of icosahedral, decahedral and octahedral nanoparticles as a function of number of atoms in the nanoparticle.

For crystalline nanoparticles the Wulff construction provides a general method to predict the equilibrium morphology that minimises the total energy. In addition, the morphology of supported nanoparticles can be obtained using Wulff-Kaishew construction. These two methods will be discussed in chapter 3.

Functional nanoparticles are usually designed with an optimal morphology and size on different supporting underlayers to achieve the best performance [5]. For example, FePt magnetic recording media should be deposited as individual nanoparticles (or grains) with a small size to increase the information storage, while remaining large enough in size to overcome the superparamagnetic limit. Different morphologies of Pt nanoparticles, such as sphere, cube and tetrahedron, determine the rate of catalytic reaction (e.g. the conversion between trans-2-butene and cis-2-butene) due to the different ratios of exposed (100) and (111) facets [6]. Alloyed nanoparticles add compositional flexibility to size and shape to tune properties further. For example, bimetallic nanoparticles may present different compositions on each of their facets which can affect reactivity (e.g. for CO oxidation on RhPt nanoparticles [7]). An important issue is that the shape and therefore properties of nanoparticles can be modified by interactions with their environment. For example, the morphology of the nanoparticles can reconstruct due to facet dependent molecular adsorption and in the presence of solvents [8]. Au nanoparticles are predicted to switch

between icosahedral and truncated-octahedral shapes under different polar solvents [9]. Different substrates for supported nanoparticles can also significantly affect nanoparticle shape providing another means of tuning properties .

Many experimental tools are available to analyse the structure and properties of nanoparticles and study the effect of different synthesis strategies. For example, transmission electron microscopy (TEM), X-ray photoelectron spectroscopy (XPS) and thermal desorption spectroscopy (TDS) provide information on the atomic structure, electronic properties and chemical reactivity of functional nanoparticles, respectively. Although these analyses can offer a lot of information for understanding interactions between nanoparticles and underlayers (or molecules) they can be challenging to interpret and are not predictive. Therefore, theoretical calculations at the atomic level (such as density functional theory and empirical potential calculations) can be very useful for understanding and improving the functional characteristics of nanoparticles. Simulations are still limited in the number of atoms that can be modelled (N normally less than 10^3). Therefore, to provide insight into an effect one should carefully separate the problem into several intermediate steps, perform calculations and piece together various results to develop a model.

1.2 Aim of This Thesis

The purpose of this thesis is to understand how the presence of different supporting substrates and adsorbed molecules influences the shape of the metallic nanoparticles. The effect of modified shapes on the functional characteristics will also be studied. Although many experimental investigations study the shape of nanoparticles, the atomic structure and interaction between specific atoms are often missing making the story incomplete. In this thesis, we choose four interesting topics (each presented as a separate chapter) to study the effects of changing nanoparticle shapes. First, we study the wetting of $L1_0$ ordered FePt nanoparticles supported on $Mg_{(1-x)}Ti_xO$ substrates for magnetic recording applications. Next, we investigate the fundamental problem of Ti nanoparticle oxidation. Thirdly, we study how oxidation can drive a change in the atomic arrangement of TiPt bimetallic nanoparticles. Finally, we investigate the formation of ZnO encapsulated Au nanoparticles under oxidation and calculate the reaction energy for CO oxidation to as-

sess possible reaction pathways. For each investigation, there is a brief introduction at the beginning of every chapter to describe the motivation and the necessity of the specific research.

Chapter 2

Background

There are three main investigations in this thesis, the experimental and theoretical background of those investigations are detailed in the following sections. Section 2.1 describes previous work on heat-assisted magnetic recording with FePt media and Mg(Ti)O substrates. Section 2.2 details recent work on Ti nanoparticles and their oxidation. In addition, bulk Ti has been discussed as well. Finally, section 2.3 discusses previous investigations on Au nanoparticles, wurtzite ZnO and the strong metal-support interaction between them.

2.1 $L1_0$ Ordered FePt for Heat-assisted Magnetic Recording Media

Magnetic recording is widely used for information storage. In early hard disk drives (HDDs), longitudinally magnetised bits, lying in the disk plane, were used to store the digital information. In order to increase capacity, the physical dimension of the magnetic bits have continued to shrink. However, strong dipole coupling between ferromagnetic grains of longitudinally magnetised bits limits the range of the size reduction [10]. Therefore, perpendicular magnetic recording was introduced in 1978 [11]. Toshiba produced the first commercially hard disk drive using perpendicular magnetic recording technology in 2005. Materials possessing high magnetocrystalline anisotropy (K_{u}) in one axis are

most promising candidates for perpendicular magnetic recording, for example FePd, FePt and CoPt provide 10^7 erg/cm^3 magnetocrystalline anisotropy along the c-axis [12, 13]. Materials with high magnetocrystalline anisotropy (also called hard ferromagnetic materials) usually have high coercivity (H_c) and it takes significant effort to demagnetise in order to change the magnetisation direction. Although those kind of materials have an advantage for decreasing the size of one magnetic domain, it is impractical and impossible to reverse the magnetisation with a small write field in HDDs. In fact, the coercivity of many materials depends on the temperature of the magnetic region. Hence, if the magnetic domain is heated up to the Curie temperature of the material, the high thermal energy makes the ferromagnetic material become paramagnetic. Once the material is temporarily paramagnetic, it is easy to apply a magnetic field to align their magnetisation along particular direction. The magnetic field will maintain the direction of alignment after the temperature of the local region cools down. Combining a ferromagnetic material with high magnetocrystalline anisotropy with the above heating procedure is called heat-assisted magnetic recording (HAMR). Due to the hard ferromagnetic property, a magnetic grain of HAMR media can be deposited in a very small diameter parallel to the surface compared to traditional recording media. Thus, HAMR media delivers higher information density than others.

The rest of this section is on $L1_0$ ordered FePt nanoparticles as HAMR media and is organized as follows. Section 2.1.1 introduces the fundamental properties of FePt and MgO. Next, section 2.1.2 and 2.1.3 summarise the different methods to stabilise the supported FePt on MgO with desired magnetic properties and the conductive MgTiO material as the underlayer of sputtered FePt, respectively. Finally, section 2.1.4 details the morphology and wetting of FePt on different underlayers.

2.1.1 Fundamental properties of $L1_0$ ordered FePt and MgO

$L1_0$ ordered FePt is a periodic structure with alternating atomic layers of Fe and Pt in the [001] direction as shown in Fig. 2.1(a). The lattice constants of $L1_0$ ordered FePt structures in experimental observation are $a = b = 3.84$ and $c = 3.71$ Å [14, 15]. The space group of the FePt structure is P4/mmm [16]. FePt is a candidate for HAMR media with $7{\times}10^7$ ergs/cm^3 magnetrocrystalline anisotropy along the c-axis ([001] direction) in the

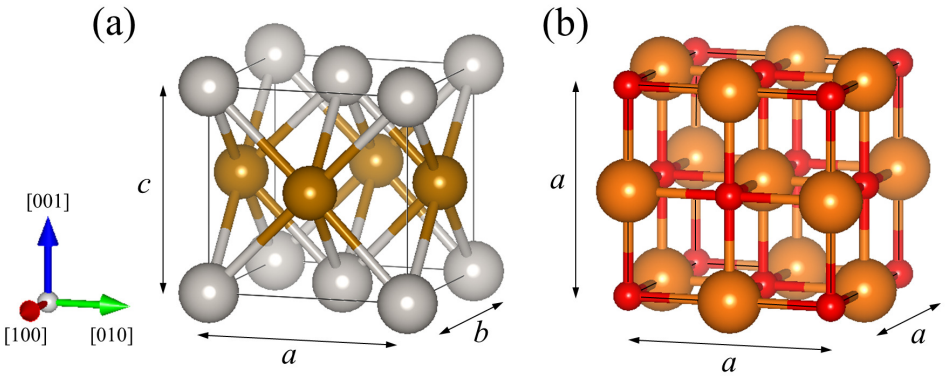

Figure 2.1: The structures of (a) $L1_0$ ordered FePt and (b) rock-salt MgO. The brass, sliver, orange and red spheres represent the Fe, Pt, Mg and O atoms.

bulk. By using a superconducting quantum interference device (SQUID) magnetometer, FePt thin films (10 nm thick) supported by Si wafers have been shown to achieve 50 kOe out-of plane coercivity depending on the specific annealing temperature and time [17]. In addition, FePt nanoparticles in the range of 2 to 8 nm diameter have large coercivity (22.3 kOe) at room temperature as well [18]. With the high coercivity, $L1_0$ ordered FePt can provide good performance for HAMR media in HDDs. Therefore, experimental investigations focus on finding the substrates for FePt deposition with good (001) texture and out-of-plane coercivity, such as Si, MgO, TiN, TiNO and FeCoNi [17]. Furthermore, the increased in-plane coercivity usually leads to the decrease of out-of-plane coercivity due to the misorientation of the FePt grains. Thus, both in-plane and out-of-plane coercivities are always measured in magnetic hysteresis (M-H) loops after sputtering.

One of the most popular substrates for growing FePt grains is rock-salt MgO with (001)-texture. Rock-salt MgO consists of a pair of Mg and O atoms at a lattice points of the face-centred cubic (fcc) lattice as shown in Fig. 2.1(b). The experimental lattice constant of MgO is $a = 4.21$ Å [19]. The experimental band gap of rock-salt MgO is 7.8 eV at $\Gamma-$point [20]. However, the theoretical band gap is in the range of 3 to 8 eV depending on the method of calculation [19, 21]. There are two types of (001)-textured MgO substrates, one is polycrystalline and the other is single crystalline. The experiment reveals the polycrystalline MgO including grain boundaries (GBs) between different MgO orientation (normal to the surface), such as (100), (101) and (111) orientations [22]. DFT calculation shows that polycrystalline MgO forms particular geometries of grain boundaries reducing

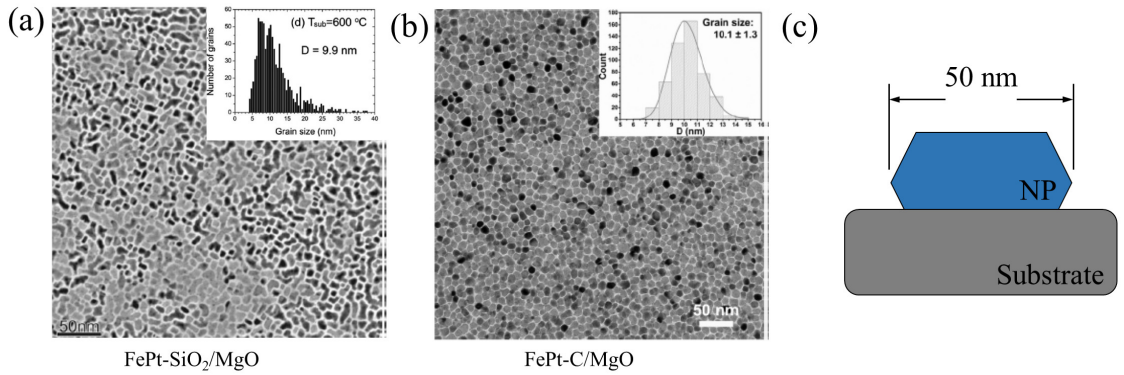

Figure 2.2: TEM images and diameter distributions of (a) FePt-SiO_2 and (b) FePt-C granular film. Both diameters of FePt grains approximates to 10 nm. (c) Visualization of faceted grain 50 nm in diameter deposited on MgO substrate (a) is reproduced from Ref. 28 and (b) is reproduced from Ref. 22.

the local band gap by up to 3 eV [23].

2.1.2 Epitaxial growth of FePt on MgO underlayer

A huge out-of-plane coercivity, as high as 70 kOe, is measured at room temperature when 10 nm thick FePt grains are deposited on MgO substrates. The diameter of the grains are about 50 nm parallel to the surface (shown in Fig. 2.2(c)) [24]. The large diameter of the grains decreases the density of information storage, hence much research is aimed at reducing the grain size. Finite size effects suggest that a grain size less than 5 nm may lead a significant decrease of the magnetocrystalline anisotropy [25]. Meanwhile, the thermal effect suggests the stability ratio ($K_{\mathrm{u}}V/k_{\mathrm{B}}T$, where V is the volume of grain) should be larger than 60 for long recording time. Considering the balance of life time, stability and storage density, an optimal FePt grain size on MgO is about 6 nm. In order to decrease the size of the FePt grains and also isolate them from each other, segregants are often used. SiO_2, C and Ag are used as segregants for the FePt/MgO system, while ZrO_2 is the segregant for the FePt/TiON system [26–28]. SiO_2 successfully segregates and separates the FePt grains into a fine structure with diameter 6.2 nm. However, the TEM images shows interconnected FePt grains (Fig. 2.2(a)) yielding a poor out-of plane coercivity.

By co-sputtering Fe, Pt, and C on heated MgO (001) underlayer (FePt-C/MgO), the

$L1_0$ ordered FePt can be successfully deposited on MgO with 5.5 nm grain diameter [29]. The formation of granular FePt is shown in 2.2(b) using TEM. The experiment observes that the C forms an amorphous structure and is insoluble into the FePt grains. However, microstructure analysis reveals that the increase of C concentration decreases the $L1_0$ ordering of FePt grain due to the interfacial strain. The increased disorder of FePt results in a decrease in the out-of-plane coercivity [30]. In addition, the FePt grain is not able to grow up to the second layer of FePt since the amorphous carbon channel (upon the first layer grains) prohibits the (001) texture of FePt structure and reduces the perpendicular ferromagnetic property significantly. In order to increase the $L1_0$ ordering of FePt grains in the FePt-C/MgO system, Platt et al. shows using additional Au and Ag can enhance the $L1_0$ ordering and result in an additional 1 to 2 kOe coercivity compared to pure FePt grains [31]. Moreover, the Au and Ag additives also chemically segregate from FePt grains. Therefore, Ag additive is introduced in the FePt-C/MgO system and responsible for increasing the $L1_0$ ordering. By using scanning transmission electron microscope-energy dispersive X-ray spectroscopy (STEMEDS), elemental mapping shows the Ag forming as shells surrounding the FePt grains in the FePtAg-C/MgO system [32]. In consequence, the average grain size of FePt is 6.1 nm with the perpendicular coercivity of 37 kOe [33]. Recent (theoretical and experimental) works show the magnetic property of (001)-textured polycrystalline and single-crystalline MgO underlayers for sputtered FePt-C grains using transmission electron microscopy (TEM) for texture analysis. The result indicating the polycrystalline MgO leads to misorientation of the FePt grains introducing an in-plane coercivity in the FePt-C/MgO system [22]. Later, Hono et al. deposited granular FePt-C on single-crystalline MgO underlayer eliminating the in-plane ferromagnetism and further improving the perpendicular coercivity [34]. However, due to the industrial viability, it is impractical to use single crystal MgO in the HAMR media.

There are a few theoretical studies of the interface between FePt and MgO slabs. The DFT results show that the most energetically stable configuration is Fe atoms directly adsorbing on top of O atoms with 10 % in-plane strain [35, 36]. The geometry (Fe atom lies on O atom) is also the favourable configuration of small FePt alloys (Fe_2Pt and Fe_2Pt_2) adsorbing on the MgO (001) surface [37]. The deposition reduces the net magnetic moment (MM) of the interfacial Fe $3d$ state transferring part of the charge from the Fe atoms to the near Pt and O atoms.

2.1.3 Conductive $Mg_{(1-x)}Ti_xO$ underlayer

Since MgO is an insulator, radio frequency (RF) sputtering must be used to deposit Fe and Pt on the MgO (001) surface. However, this method limits the sputtering rate and is impractical for industrial applications. Recent work reported (001)-textured FePt grains are able to grow on a Ti doped MgO underlayer ($Mg_{(1-x)}Ti_xO$) [38]. The $Mg_{(1-x)}Ti_xO$ is rock-salt structure as well, but acquires an electrical conductive property rather than insulating MgO. In addition, the $Mg_{(1-x)}Ti_xO$ can maintain the rock-salt structure with a wide range of x, $0 \leq x \leq 0.8$. It is not surprising incorporation Ti atoms into the MgO substrate can improve the conductivity. Investigations first found that the existence of rock-salt TiO and indicated the metal-oxide π-bond stabilising the formation [39, 40]. Morin also found that rock-salt TiO is a metal over the whole temperature range (1.5 K to 300 K) [41]. Due to the good conductivity of MgTiO, the substrate permits deposition of FePt by direct current (DC) sputtering, which accelerates the deposition rate and offers better control over grain size of FePt. However, the morphologies of FePt nanoparticles grown on MgTiO are significantly different to those grown on MgO. In particular, the contact angles are smaller for FePt grain growth on MgTiO compared to on MgO (shown in Fig. 2 in Ref. 38). That indicates the FePt has larger interfacial energy between FePt and MgTiO instead of MgO. The doped Ti atoms increase the wetting of FePt on MgTiO reducing the height of FePt grains. The height reduction along the [001] direction decreases the perpendicular coercivity and leads to interconnected FePt grains, offsetting any benefit obtained by the use of DC sputtering.

2.1.4 Morphology of $L1_0$ ordered FePt nanoparticles

There are many theoretical investigations of $L1_0$ ordered FePt surfaces for understanding the morphology of FePt nanoparticles relative to FePt HAMR media. The surface energies of low-index FePt calculated using first-principles methods indicates the (111) surface has the lowest surface energy (1.87 J/m^2) [42]. In addition, the FePt phase diagram shows that the non-stoichiometric (001) surface is Pt-terminated and the termination of (110) depends on the chemical potential of either Fe and Pt atoms. Thus, the equilibrium shape of the free FePt nanoparticle includes (100), (111) and Pt-terminated (001) facets. Monte Carlo

simulations indicate the morphology of $L1_0$ ordered FePt is truncated-octahedral, but the Pt-terminated (001) surface may include some disordered atoms due to thermal effects [43]. The $L1_0$ to $A1$ order transition of 5 nm FePt nanoparticles occurs at about 1300 K and the lower boundary of nanoparticle size is 4.4 nm overcoming the superparamagnetic limit [43, 44]. Apart from the truncated-octahedral shape, experimentally free FePt nanoparticles can be synthesised in various kinds of nanocrystals (such as nanorods, nanocubes, spherical nanoparticles, etc) depending on the size without any temperature treatment. Those FePt nanoparticles are superparamagnetic unless the nanocrystals transform into $L1_0$ order with annealing process [45].

2.2 Ti and TiPt Nanoparticles Oxidation

Metallic nanoparticles are widely used in many catalytic applications due to the high surface-to-volume ratio. The $3d$-electrons of Ti atoms make it popular for catalytic nanoparticles for oxidation, reduction and photocatalytic reaction. For example, small Ti nanoparticles (13 Ti atoms) show superior performance for hydrogen exchange reaction in $NaAlH_4$ for producing H_2 compared to other catalysts (such as $TiCl_3$) [46]. In addition, Ti-containing bimetallic nanoparticles also show promising catalytic performance for other reactions. TiNi nanoparticles provide better photodecomposition ability for methylene blue than the generally used commercial TiO_2 nanoparticles [47]. TiPt nanoparticles theoretically demonstrate better oxygen reduction reaction (ORR) in proton exchange membrane fuel cells (PEMFCs) [48]. Nanoparticles for particular applications are normally exposed to an oxygen-rich environment, such as an ambient atmosphere, water and oxide substrate [49–51]. Therefore, for improving the performance of catalytic reactivity, understanding the oxidation of metallic nanoparticles is an important issue.

The rest of this sections are organised as follows. Section 2.2.1 discusses fundamental properties of pure Ti nanoparticles. Next, section 2.2.2 details the previous works of oxygen adsorption on Ti (0001) surface. Section 2.2.3 summarises the recent works on TiPt binary nanoparticles. Finally, section 2.2.4 provides the investigations of atomic arrangement of bimetallic nanoparticles with and without oxidation.

2.2.1 Fundamental properties of Ti nanoparticles

There are numerous studies investigating the morphologies and properties of Ti and Ti-based nanoparticles. Guided ion beam mass spectrometry and photoelectron spectroscopy shows that stable Ti nanoparticles favour icosahedral shape in the range of $1 \leq N \leq 130$, where N is the number of Ti atoms [52, 53]. Extended X-ray absorption fine structure (EXAFS) analysis also indicates the morphology of a 13 atom Ti nanoparticle is a distorted icosahedron [46]. DFT calculations show that very small Ti nanoparticles ($2 \leq N \leq 13$) possess numerous isomers with similar energy [54]. The calculated stability of Ti nanoparticles with more atoms ($13 \leq N \leq 55$) suggests the Ti nanoparticles of icosahedral symmetry are the most energetically favourable, consistent with experimental observations [55, 56]. In addition, the comparison between nanoparticles consisting of either hexagonal close-packed (hcp) or fcc close-packed structure suggests that the fcc structure dominates the morphology of Ti nanoparticles in the range of $1 \leq N \leq 55$ [56]. Theoretical investigations show that Ti nanoparticles are highly magnetic when $N \leq 8$, but the magnetic moment rapidly approaches to zero (bulk-like) when $N = 13$ [54, 57]. Moreover, the electronic property of Ti nanoparticles becomes bulk-like for $N \geq 8$ [57].

The morphology of nanoparticles depends on the formation energy which is sensitive to the elastic strain energy. For example, the strain energy per atom of Ni nanoparticles are 0.033 and 0.001 eV for icosahedral and decahedral, respectively [58]. Due to the increased number of atoms, the elastic strain on the nanoparticle dominates the morphology, thus icosahedral nanoparticles become relatively unstable and transform into the decahedral or truncated-octahedral depending on the species of atom [4]. Therefore, nanoparticles in decahedral shape up to micrometer size are usually found in the experimental observations [59–61]. As nanoparticles grows larger, the additional adatoms try to minimise the large stain of nanoparticles particularly at the edge and centre of the nanoparticle [62]. For example, decahedral nanoparticles may transform into Ino-decahedral or Marks-decahedral morphologies [59]. Eventually, very large Ti nanoparticles should consist of hcp structure and the morphology of nanoparticles in the nm size range can be predicted using the Wulff construction based on surface formation energies.

2.2.2 Oxidation of the pure Ti (0001) surface

There have been few experiments studying the oxidation on Ti nanoparticles. However, surface oxidation of the Ti bulk metal has been systematically studied both experimentally and theoretically providing constructive information [63, 64]. Auger electron spectroscopy (AES) and low-energy electron diffraction (LEED) reveals at low concentration a $p(2\times2)$ oxygen adsorption on the single crystalline Ti (0001) surface [65, 66], which corresponds to a 1/4 monolayer (ML) coverage. Ultraviolet photoemission spectroscopy (UPS) and X-ray photoelectron spectroscopy (XPS) demonstrates the oxidation states of Ti may be Ti^{II}, Ti^{III} and Ti^{IV} depending on the temperature and oxygen concentration [67–71]. The initial oxygen absorption completes in a very short time period on the Ti surface, but the following oxidation further into the bulk Ti is a much slower process [72–74]. In addition, AES observation shows that the diffusion of the oxidation front can be significantly accelerated by heating up the temperature greater than 500 K [63, 70, 75].

Although the experimental observations do not provide the desired identification of the O adsorption site on the Ti (0001) surface, theoretical calculations do investigate the adsorption sites. DFT calculations show O atoms incorporate in the octahedral interstitial site in bulk Ti [76], while O atoms adsorb on the three-fold hollow sites on the Ti (0001) surface [64, 76, 77]. The calculations also indicate two O atoms should not adsorb on two adjoining hollow sites on the surface, otherwise there will be a significant electronic density deformation between two adsorbing O atoms [77]. The calculated energy barrier of O atom diffusion between the octahedral sites in bulk Ti is approximately 2.1 eV [76]. However, the energy barrier for O atom penetration from surface to subsurface is in the range of 0.14 to 4.42 eV depending on the O concentration on the Ti surface [64]. The investigation of the oxidation of a 13-atom Ti nanoparticle shows oxygen atoms adsorb on the three-fold hollow sites on the fcc (111) facet similar to the oxygen adsorption on Ti (0001) surface [78].

2.2.3 Oxygen adsorption on TiPt nanoparticles

Apart from the pure Ti nanoparticle, Ti-containing nanoparticles is also a promising catalyst in many applications. One of the bimetallic nanoparticles studied is TiPt which plays

important roles in proton exchange membrane fuel cells (PEMFCs). Pure Pt nanoparticles are used for the oxygen reduction reaction (ORR) at the cathode in PEM fuel cells [79]. However, the scarcity and cost of pure Pt has driven both experimental and theoretical investigation on Pt-containing alloy nanoparticles. Theoretical calculations indicate that the Pt_3Ti (111) surface provides a weaker bond between the Pt_3Ti surface and O_2 molecule reducing the activation energies for the ORR mechanism [80]. In addition, the core-shell TiPt nanoparticles are also predicted to exhibit weaker Pt-O bond reducing the activation energy and improving catalytic performance for PEM fuel cells [48]. Experimental investigations show that TiPt nanoparticles can be synthesised on carbon-black supports with controlled-size and compositional uniformity [81]. The TiPt nanoparticles may detach from the carbon support and coalesce together during catalytic cycles [82]. Thus, recent works suggested replacing the support from carbon-black to TiO_x oxide preventing the loss of electrochemical surface area [83]. The experimental investigation demonstrates that the $Pt_{75}Ti_{25}$ nanoparticles exhibit a good catalytic performance with respect to other atomic ratios. Hence, there are many theoretical calculations studying oxygen adsorption for ORR mechanisms on TiPt nanoparticles. DFT calculations reveal the O_2-induced surface strain (1.83 %) on TiPt nanoparticle is greater than the strain on pure Pt nanoparticle (0.00 %). The larger strain enhances the O_2 dissociation further improving the ORR on TiPt nanoparticles [84]. Moreover, the electron accumulation on the adsorbing O atom for TiPt nanoparticles facilitates the protonation of O adatoms forming H_2O [84]. Therefore, theoretical calculations showing the bond formation between TiPt nanoparticles and molecules plays a important role on the catalytic characteristics of nanoparticles.

2.2.4 Atomic arrangements of bimetallic nanoparticles

According to the theoretical investigation described in section 2.2.3, the catalytic performance of TiPt nanoparticles is significantly dependent on oxygen bond formation. In order to understand the bond formation between nanoparticles and reacting molecules, many investigations study the atomic arrangement of bimetallic nanoparticles. By using magnetron sputtering and size-selective techniques, TiPt nanoparticles can be deposited on holey carbon TEM films with very specific size and weight [85]. High-angle annular dark-field (HAADF) STEM images show the morphologies of oxidised TiPt nanoparticles

can be both single and multiple core(s)-shell structures [86]. The geometric structure (core-shell) is a common atomic arrangement for alloyed nanoparticles (such as AuAg, TiNi and TiAuPt nanoparticles) observed using STEM [61, 87–89]. The core of TiPt nanoparticles solely consists of Pt atoms and the shell is made of TiO_2. The number of cores relates to the size of the TiPt nanoparticles, small (2 nm) and large (5 nm) nanoparticles contain single and multiple Pt core(s), respectively. Blackmore et al. suggest that each co-sputtering TiPt nanoparticle initially includes one Pt core, then the nanoparticle-nanoparticle collisions in the gas phase cause coalescence, introducing the multiple cores in nanoparticles [86]. Besides the experimental observation, theoretical calculations summarise the stabilities of various atomic arrangements of pure metallic nanoparticles (TiNi) [90]. The bimetallic nanoparticles preferentially segregate the two species from each other (two sides of the nanoparticle) to minimise the formation energy instead of forming a core-shell structure [90]. Due to the contradiction between the theoretical investigation and the experimental observation, the adsorbed molecule in reality may dominate the atomic arrangement, further influencing the catalytic reactivity.

2.3 Au Nanoparticle Supported on ZnO for CO Oxidation

Besides the Pt nanoparticles discussed in section 2.2, many other metal nanoparticles are used as catalysts to accelerate reactions, such as Rh, Pd and Au [91]. Au nanoparticles are promising catalysts for improving the performance of CO conversion to CO_2. Au nanoparticles supported on ZnO tetrapods demonstrate particularly high reactivity for CO oxidation compared to other catalytic systems (such as Au/TiO_2 and CeO/CuO) [92]. In Chapter 6 we present theoretical calculations to provide insight into the structures and properties of this system. Here we provide some discussion of the previous work related to this topic.

The rest of this section is organized as follows. Section 2.3.1 summaries the fundamental properties of Au surfaces and Au nanoparticles. Next, section 2.3.2 details the DFT functionals used for ZnO calculations, observations of ZnO nanorods and the defect in bulk ZnO. Finally, section 2.3.3 discusses molecular adsorption (such as O_2 and CO) on Au nanoparticles and the reaction path of CO oxidation on the Au_{NP}/ZnO system.

2.3.1 Morphology of Au nanoparticles

The experimental lattice constant of fcc Au is 4.08 Å and a slightly larger lattice constant is usually obtained from DFT calculations [93, 94]. The three low-index surfaces of the Au fcc structure are (100), (110) and (111) and the calculated formation energies are 0.85, 0.90 and 0.74 J/m^2, respectively [93, 95]. Theoretical calculations assess the stability of Au nanoparticles in different morphologies demonstrating the truncated-octahedral Au nanoparticle (consisting of (100) and (111) facets) is the most energetically stable morphology, which shows a good arrangement with experimental observations [96]. The calculations further indicate the Au nanoparticle in truncated-octahedral shape should consist of 90 % by area of (111) facets to minimise the surface free energy. Moreover, the experimental observation shows the morphology of the Au nanoparticles can be reversibly transformed between truncated-octahedron and decahedron in different ambient gasses and liquids [9]. The transformation relies on the bond formation between Au facets and polar solvents (such as water) changing the surface formation energy.

The catalytic Au nanoparticle used for CO oxidation can be deposited on different underlayers, such as surfaces and nanorods of TiO_2, MgO, SiO_2 and ZnO [9, 92, 97, 98]. One of the most important phenomena of metallic nanoparticles deposited on oxide substrates is the strong metal-support interaction (SMSI). SMSI can give rise to drastic changes in the chemisorption properties of noble metals supported by oxides [99]. Besides the difference of the chemisorption, the SMSI affects the wetting of nanoparticles reconstructing the morphology of the nanostructure [100]. By using TEM, recent work shows that annealing ZnO-supported Au nanoparticles at 500 K and 600 K with O-rich environment (oxygen gas flow) for one hour can lead to the formation of a ZnO encapsulation layer around the nanoparticles [101]. The encapsulated Au nanoparticles shows 1.5 times greater CO conversion compared to the non-encapsulated Au nanoparticles at room temperature (300 K). The TEM images show the supported Au nanoparticle is a single crystal and its (111) plane parallel to the ZnO (0002) surface [92]. Moreover, recent observations provide other orientations of Au nanoparticles supported by ZnO [101]. However, there are presently no theoretical studies addressing this topic.

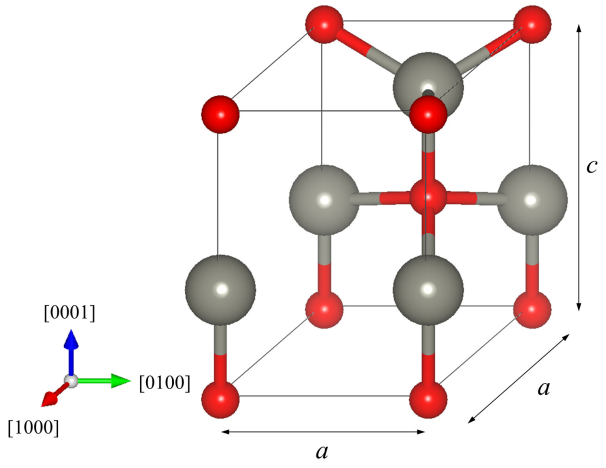

Figure 2.3: The atomic structure of wurtzite ZnO (primitive cell). The grey and red spheres represent the Zn and O atoms.

2.3.2 Defects and surfaces of wurtzite ZnO

Fundamental properties of ZnO

XRD shows that ZnO nanorods (including tetrapod morphologies) have a wurtzite crystal structure. The primitive cell of wurtzite ZnO is shown in Fig. 2.3 [92, 102]. The experimental lattice constants of wurtzite ZnO are $a = 3.24$ and $c/a = 1.60$. DFT calculations using the LDA exchange-correlation functional obtain lattice constants of wurtzite ZnO of $a = 3.20$ and $c/a = 1.61$, while the formation enthalpy of ZnO is -3.4 eV [103, 104]. The experimental band gap of wurtzite ZnO is 3.44 eV, whereas the gap energy for standard DFT calculations is significantly underestimated (0.80 eV) [105]. Therefore, there are many works that try to improve the band gap using different methods. Table 2.1 summarises the lattice constants and band gaps obtained by recent works on ZnO with different functionals. Although the GGA+U method predicts a larger band gap compared to standard DFT calculations, it is still underestimated about 1.7 eV. The most accurate prediction of lattice constants and band gap is given by the hybrid functional HSE, while the GGA+NLEP+U method also provides acceptable values.

Functional	a (Å)	c/a	Band gap E_g (eV)
LDA [106]	3.19	1.62	0.80
GGA	3.29	1.62	0.75
GGA+U [107]	3.20	1.61	1.7
GGA+NLEP+U [108]	3.20	1.58	3.23
HSE [109]	3.25	1.60	3.4
Experiment	3.24	1.60	3.44

Table 2.1: Calculated and experimental fundamental properties of ZnO. a and c are the lattice constants, while the band gap is the difference between CBM and VBM at the Γ-point.

Structure of ZnO nanorods

XRD and Raman spectroscopy show that ZnO nanorods (tetrapods) are wurtzite structured and consists of $(10\bar{1}0)$ and $(11\bar{2}0)$ side surfaces [92]. In addition, TEM also demonstrates the ZnO nanorods grow in the [0001] direction with the characteristic distance $d_{[0002]} = 2.6$ Å[110]. For the three surfaces of ZnO (0001), $(10\bar{1}0)$ and $(11\bar{2}0)$, only (0001) surface is a polar surface, whereas $(10\bar{1}0)$ and $(11\bar{2}0)$ surfaces are not. The calculated formation energy (using the PBE functional) of ZnO $(10\bar{1}0)$ and $(11\bar{2}0)$ surfaces are 1.6 and 1.7 J/m^2, respectively [105]. Investigations also demonstrate the formation energy of the polar ZnO (0001) surface is twice as large than that of the ZnO $(10\bar{1}0)$ surface. This theoretical result implies nanorod formation should consist of both non-polar surfaces which is consistent with the XRD results. SEM shows the formation of wurtzite ZnO nanorod is hexagonal shape in cross-section to the [0001] direction [111]. The shape of the tips of the ZnO nanorod (such as flat and needle-like shape) depends on the synthesis conditions.

There are many methods for preparing ZnO structures in naonometre size, such as chemical vapor deposition (CVD), electrochemical methods, hydrothermal synthesis and wet-chemical approaches [110–114]. However, the morphology of the synthesised ZnO may differ significantly by controlling one parameter in the preparation. For example, the ZnO nanostructure can transform from a needle-like shape to a spherical shape with increased annealing temperature by using the solgel method [115]. Apart from the temperature control, the pH (from 6 to 9) of the solution at a given temperature yields different mor-

phologies of ZnO, such as tube-like, flower-like and star-like (tetrapod) [116]. In addition, the comparison between CVD and hydrothermal synthesis shows the latter one provides better crystal quality [114]. In spite of the geometrical variants for different synthesis methods, most nanostructures of ZnO involve $(10\bar{1}0)$ and $(11\bar{2}0)$ side surfaces and (0001) surfaces for top and bottom of the nanorods.

Native point defects in ZnO

Zinc oxide is a typical n-type semiconductor and many experimental and theoretical works have studied its defect properties (such as stability and mobility). Oxygen vacancies and zinc interstitials are two common defects in bulk ZnO leading to intrinsic n-type conductivity [117]. The former and latter defect is denoted as V_O and Zn_i using KrögerVink notation, respectively. There are many experimental observations of the ionisation energy of electrons or holes in defect levels can correspond to thermodynamic transition level in theoretical calculations [118–120]. Electron paramagnetic resonance (EPR) spectroscopy identifies the donor level of the metastable $V_O^{\cdot}$ at 0.92 eV below the conduction band minimum (CBM) [121]. In addition, photoluminescence studies observe a green 510 nm emission from the excited state to conduction band associated with the oxygen vacancy [122]. Both studies indicate the oxygen vacancy is a deep donor with a defect level located in the energy range 1 eV below the CBM. By using Hall-effect measurements, Hutson reported the zinc interstitial as a shallow donor with low ionisation energy (0.05 eV), while Look and Hemsky suggested the dominant shallow donor is zinc interstitial at 0.03 eV below the CBM [117, 123]. The concentration of the donors in n-type ZnO is approximately 10^{17} cm^{-3} and the density of oxygen vacancies is slightly greater than that of zinc interstitials [123, 124].

Besides the experimental observations, there are may first-principles investigations predicting the charge transition levels as a function of Fermi energy in bulk ZnO. Table 2.2 summarises the transition levels of the three native defects (including the oxygen vacancy, zinc vacancy and zinc interstitial) using different functionals. Standard DFT calculations (LDA and GGA) shows similar transition levels for oxygen and zinc vacancies, except for $\varepsilon(1-/2-)$. The LDA+U and GGA+U show a similar trend to the standard DFT calculations, but the exact transition levels are shifted closer to the middle of the

Defect	q/q'	LDA	LDA+U	GGA	GGA+U	hybrid(HSE)
V_O	$\varepsilon(2+/0)$	0.50	1.10	0.74	1.22	2.20
V_{Zn}	$\varepsilon(0/1-)$	0.08	0.11	0.22	0.30	0.80
	$\varepsilon(1-/2-)$	0.29	0.45	0.75	1.10	2.50
Zn_i	$\varepsilon(2+/1+)$	1.41	2.01	0.65	1.67	3.35
	$\varepsilon(1+/0)$	1.41	2.06	1.52	2.5	3.35
Reference		[106, 125]		[107, 125]		[109, 126]

Table 2.2: The transition levels of point defects in ZnO. The listed energies are the position of the defect level above the valence band maximum (VBM) of bulk ZnO.

gap (considering the experimental value). However, the underestimated band gap makes it difficult to predict accurate ionisation energies for electrons and holes. Hybrid calculations demonstrate ε(2+/0) of oxygen vacancy is 1.0 eV below the CBM, which is in good agreement with experimental results [126]. The ε(0/1-) and ε(1-/2-) transition levels of the zinc vacancy are 0.8 and 2.50 eV above the valence band maximum. The zinc interstitial can incorporate on both octahedral and tetrahedral sites in bulk ZnO, whereas the octahedral zinc interstitial is approximately 1 eV more stable than tetrahedral zinc interstitial [127, 128]. Most standard DFT and $+U$ calculations show the transition levels of zinc interstitial around the middle of the band gap (1.5 eV above the VBM). Hybrid calculations predict that the transition levels are very close to the CBM [107, 109]. These investigations indicate the calculation method not only influences the bulk properties but also affects the stability of the defect state.

Apart from the stability of the defect, the mobility of diffusing native defects are also investigated in first-principles calculations. The energy barriers for both oxygen vacancies and zinc interstitials in bulk ZnO are dependent on both the defect charge state and the migration pathway. For the oxygen vacancy, $V_O^{\cdot\cdot}$ has the smallest energy barrier (1.09 eV) in the out-of plane pathway ([0001] direction) with a barrier of 1.5 eV for in plane diffusion [106, 129]. The investigation of zinc interstitial diffusion indicates the $Zn_i^{\cdot\cdot}$ has the smallest energy barrier. The diffusion barrier to the second nearest neighbour site for the out-of plane and in plane pathway are 0.22 and 0.33 eV, respectively [128]. Both oxygen vacancy and zinc interstitial diffuse most easily in the 2+ charge state due to the smaller ion size.

2.3.3 Molecular adsorption on Au nanoparticles

O_2 molecular adsorption

DFT calculations show the O_2 molecule can weakly adsorb on Au (111) surfaces ($E_{ads} = -0.08$ eV), while the adsorption energy of a single O atom on the Au surface ($E_{ads} = -2.54$ eV) is more stable than molecular adsorption [130]. Catalytic cycles usually involve pairs of oxygen atoms instead of single oxygen atoms, therefore most theoretical investigations focus on oxygen molecule adsorption. Theoretical calculations show the oxygen molecule preferentially adsorbs on the top of an Au atom on small Au nanoparticles ($N \leq 6$) and the O-O bond length is approximately 1.3 Å (slightly dependant on the coordination of the adjacent Au atom) [131, 132]. In addition, theoretical calculations found that charged Au nanoparticles (Au_n^-) offer more stable binding sites for oxygen molecules than neutral Au nanoparticles [131]. The enhanced bond formation between oxygen molecules and Au nanoparticles weakens the O-O interaction improving the ORR for catalytic performance. Dissociated oxygen atoms from an oxygen molecule energetically prefer adsorption on the bridge sites of Au atoms rather than top sites [133]. Although Ref. 130 demonstrates that single oxygen adsorption is more stable than oxygen molecule adsorption, the oxygen molecule adsorption is more stable than dissociative molecular adsorption by at least 0.3 eV per molecule (for Au nanoparticle with more than 4 atoms) [133]. Modelling of nm-sized nanoparticles found oxygen molecules adsorb on Au nanoparticles in metastable states with positive adsorption energy ($E_{ads} \approx 0.1$ eV) [134].

It is hard to directly observe oxygen molecule adsorption on Au nanoparticles. Thus experiments usually investigate oxygen adsorption through the measurement of gas reactions. High pressure flow-reactor methods demonstrate the size-dependent reactivity between oxygen molecules and Au_N^- nanoparticles ($N \leq 22$) [135]. This experiment also indicates the oxygen molecule acts like a single-electron acceptor during the adsorption on charged Au nanoparticle. Photoelectron spectroscopy (PES) also shows oxygen molecule adsorption depends on the size of the Au_N^- nanoparticle. The oxygen molecule chemisorbs on even-sized Au nanoparticles ($N = 2, 4, 6$), whereas oxygen molecules physisorbs on odd-sized Au nanoparticles ($N = 1, 3, 5, 7$) as determined by the vibrational structure of O-O bond [136].

Encapsulated Au nanoparticles and CO oxidation reactions

There are many underlayers for depositing the catalytic Au nanoparticle, such as TiO_2, MgO, ZnO, CeO_2, Fe_2O_3 and nonoxides [137–140]. Castillejos reported Au nanoparticles grown on ZnO tetrapod supports provide very high catalytic performance compared to other catalytic systems [92]. In addition, TEM images show ZnO encapsulation around the Au nanoparticles with annealing at 500 and 600 K [101]. The CO conversion measurement reveals the encapsulated Au nanoparticles (annealed at 500 K) provides higher catalytic performance compared to the non-encapsulated Au nanoparticles. Encapsulation can also been observed in the Au_{NP}/TiO_2 catalytic systems during heating by electron irradiation [141]. In addition, theoretical calculations suggest the oxygen molecule adsorbs at the interface between Au and oxide support reducing the activation energy for the formation of $CO+O_2$, which further enhances performance for catalytic reactions [134]. Besides the configuration of oxygen adsorption, voltammetric measurement also shows the Au_2/TiO_2 system with relative higher concentration of oxygen vacancy on TiO_2 substrate may lead a better ORR activity [142].

There are two different reaction cycles for CO oxidation on Au nanoparticles, one is the Langmuir-Hinshelwood (LH) mechanism and the other is the Eley-Rideal (ER) mechanism. The former mechanism suggests the oxygen molecule and CO both adsorb on the Au nanoparticle at neighboring sites, then the two molecules undergo a bimolecular reaction. The latter mechanism assumes one molecule adsorbs on the Au nanoparticle and the adsorbing molecule directly reacts with the other molecule from the gas phase. In the last section, experiment and theoretical calculations show oxygen molecules do adsorb on the Au nanoparticle chemically and physically. For CO adsorption, thermal desorption spectroscopy (TDS) indicates the adsorption energy of CO on the Au (111) surface is about -0.40 eV and the theoretical calculation shows good agreement with the experimental observations [134, 143]. For unsupported Au nanoparticles, DFT calculations predict a 0.4 eV reaction barrier for CO oxidation via LH mechanism [144]. Theoretical investigation of the energy barrier for the two mechanisms for CO oxidation on the Au_{NP}/ZnO system, the LH mechanism and ER mechanism cost approximately 3.00 and 0.31 eV, respectively [145]. In addition, recent work suggested the possibility of CO oxidation involving lattice O atoms on the ZnO surface with a 0.32 eV reaction barrier for CO oxidation [146]. The

oxygen vacancy can also play a role in the CO oxidation providing adsorption sites for oxygen molecules, which is known as the Mars-van Krevelen mechanism. DFT calculations predict 0.30 and 0.48 eV as the energy barrier for transition states of molecules (CO and CO_2). The above experimental and theoretical observations both demonstrate the CO oxidation process is able to proceed at room temperature and the predicted energy barrier for CO oxidation is approximately 0.3 - 0.4 eV [137].

Chapter 3

Methodology

Since predicting the structures and properties of materials is interesting for fundamental studies and applications, many simulation methods are rapidly developed to provide accurate models for atomic structure from small to large scale. With the mature theory and high computational performance, materials science is able to be further understood through fundamental insight. Although experimental observations are the mainstream method of research, some drawbacks, such as resolution of images and difficulty in measurement, limit their utility and authenticity. However, combining computational modelling together with experiment can provide more detailed insight into structural properties, atomistic mechanisms and material phenomena than experiment alone. Once the computational modelling is consistent with experiment, it enhances the reliability for both sides. Moreover, computational material design can also offer predictions of desired properties for reducing the wasted resource. Due to the above benefits, materials modelling should be improved in the accuracy and modelling size for further investigation. In this thesis, density functional theory is used to calculate the total energies of systems with interfaces, which includes molecules adsorbed on metallic nanoparticles and nanoparticle growth on various substrates.

This section is organised in the following way. Section 3.1 introduces the fundamental properties of periodic crystalline lattices. Section 3.2 describes density functional theory. Section 3.3 details some methods beyond density functional theory for correcting the band gap problem. Finally, section 3.4 introduces the analysis methods used in this thesis.

3.1 Crystal Lattices and Electronic Structure

3.1.1 Bravais lattice and reciprocal lattice

Atoms in a crystal are arranged periodically in space. The discrete lattice points can be fundamentally described by a Bravais lattice ($\boldsymbol{R}$),

$$\boldsymbol{R} = n_1\boldsymbol{a}_1 + n_2\boldsymbol{a}_2 + n_3\boldsymbol{a}_3, \tag{3.1}$$

where n_i are integers and $\boldsymbol{a}_i$ represent the three crystallographic translation vectors (which are not on the same plane). Each lattice point may include one or more atoms (basis), for example, the face-centred cubic (fcc) MgO has one Mg and one O atom at each lattice point. The reciprocal lattice ($\boldsymbol{G}$) represents the Fourier transform of the Bravais lattice. The formula of the reciprocal lattice is the following,

$$\boldsymbol{G} = k_1\boldsymbol{b}_1 + k_2\boldsymbol{b}_2 + k_3\boldsymbol{b}_3, \tag{3.2}$$

where the k_i are integers and the $\boldsymbol{b}_i$ are the reciprocal lattice vectors generated by $\boldsymbol{a}_1$, $\boldsymbol{a}_2$ and $\boldsymbol{a}_3$[147]. Which satisfy,

$$\boldsymbol{b}_i \cdot \boldsymbol{a}_j = 2\pi\delta_{ij}, \tag{3.3}$$

where the δ_{ij} is the Kronecker delta function ($\delta_{ij} = 1(if i = j)$ and $\delta_{ij} = 0, (if i \neq j)$).

3.1.2 Bloch's theorem

Bloch's theorem states that one electron wavefunctions propagating in a crystal can be represented as,

$$\psi_{\boldsymbol{k}}(\boldsymbol{r}) = e^{i\boldsymbol{k}\cdot\boldsymbol{r}}u(\boldsymbol{r}), \tag{3.4}$$

where $u(\boldsymbol{r})$ is a function with the same periodicity as the crystal, $\boldsymbol{k}$ is the wave vector and $\boldsymbol{r}$ represents the position. The function $u(\boldsymbol{r})$ follows the periodic boundary condition corresponding to the Bravais lattice $\boldsymbol{R}$,

$$u(\boldsymbol{r} + \boldsymbol{R}) = u(\boldsymbol{r}). \tag{3.5}$$

Eq. 3.4 can be rewritten using Eq. 3.5 as,

$$\psi_{\boldsymbol{k}}(\boldsymbol{r} + \boldsymbol{R}) = e^{i\boldsymbol{k}\cdot\boldsymbol{R}}\psi_{\boldsymbol{k}}(\boldsymbol{r}). \tag{3.6}$$

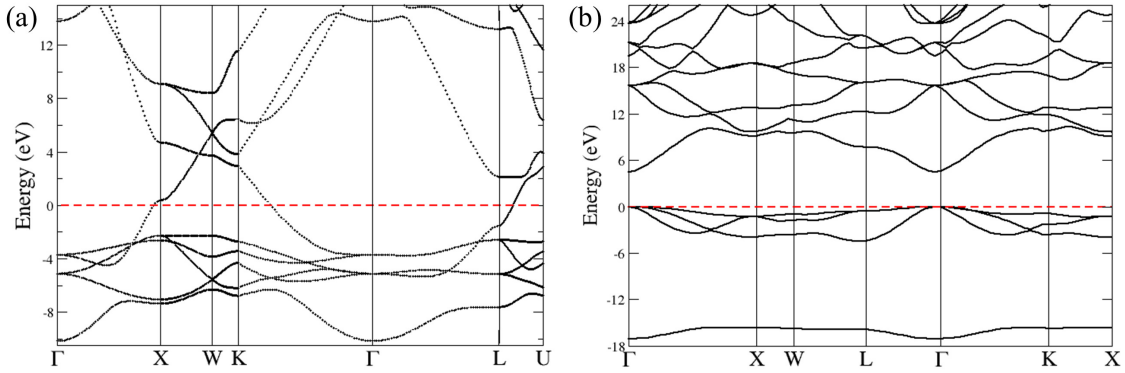

Figure 3.1: Illustration of the band structures of (a) fcc Au and (b) rock-salt MgO. The red dashed line is the Fermi energy and the insulating MgO has a 3.4 eV band gap in a density functional theory calculation with the GGA exchange-correlation functional.

Bloch's theorem shows the representation of one-electron wavefunctions in a periodic crystal.

Band structure

By placing the Bloch's wavefunction (Eq. 3.4) into the Schrödinger equation with a constant potential U (here and in the following atomic units are used),

$$\left(-\frac{1}{2}\nabla^2 + U \right)\psi_{\boldsymbol{k}}(\boldsymbol{r}) = \varepsilon_{\boldsymbol{k}}\psi_{\boldsymbol{k}}(\boldsymbol{r}), \tag{3.7}$$

the calculated eigenenergy is as follows,

$$\varepsilon_{\boldsymbol{k}} = \boldsymbol{k}^2/2 + u. \tag{3.8}$$

Thus, the eigenenergy of an electron in a periodic crystal depends on the wave vector $\boldsymbol{k}$. Once a realistic crystal potential is included, the band structure can be much more complicated and may also involve energy gaps between bands. Two examples are shown in Fig. 3.1 illustrating the band structure for fcc Au and rock-salt MgO crystal.

3.1.3 Brillouin zone

Using band structure to characterise the electronic features of a crystal is an important method. Due to the periodicity, it is not necessary to sample all $\boldsymbol{k}$ points. The first

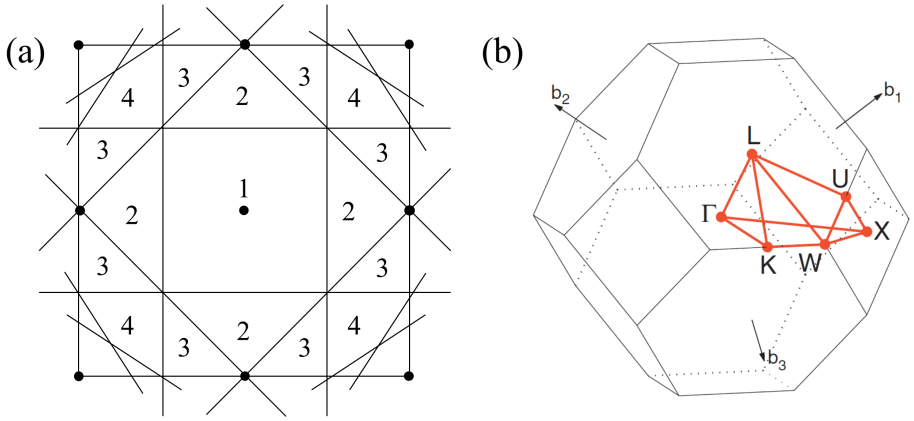

Figure 3.2: (a) An illustration of a two dimensional square reciprocal lattice. The solid lines represent the Bragg planes and the numbers label the n^{th} Brillouin zone. (b) The reciprocal lattice of a fcc Bravais lattice and the figure reproduced from Ref. 148.

Brillouin zone is a region in reciprocal space that includes all electronic information for the periodic crystal. The first Brillouin zone is uniquely determined by the primitive cell in reciprocal space. The Brillouin zone is defined using the Bragg planes (when $|\boldsymbol{k}| = |\boldsymbol{k}-\boldsymbol{G}|$) as follows: The first Brillouin zone is a region in k-space that can be reached from the origin ($\boldsymbol{k} = 0$) without crossing any Bragg plane. Fig. 3.2(a) shows an illustration for a square reciprocal lattice, the points represent the lattice points in the reciprocal lattice and the lines are the Bragg planes. The numbers in the regions represent the n^{th} Brillouin zone indicating the region can be reached from the origin crossing $n-1$ Bragg planes. Fig. 3.2(b) illustrates a sketch of the three-dimensional first Brillouin zone of the Au fcc structure. The letters on(in) the surface of the Brillouin zone represent highly symmetric points and red lines indicate a typical pathway for band structure calculations (e.g. see Fig. 3.2).

3.2 Density Functional Theory

3.2.1 Density functional theory

In principle, the Schrödinger equation can describe the properties of physical systems such as crystals. However, it is challenging to solve the many-body problem for a system with N electrons exactly if $N > 2$. Developing a method to reduce the order of variables is im-

portant. Hence, the density functional theory is established and widely used for electronic structure calculations. The concept of DFT is to replace the many-body wavefunction by the electron density. This replacement reduces the $4N$ variables ($3N$ spatial and N spin coordinates) to 4 variables (3 spatial and 1 spin coordinate(s)) increasing the feasibility of computation. Thomas originally presented the idea that the energy of system can be described as a functional of electron density in 1927 [149]. Thereafter Hohenberg and Kohn showed that the ground state energy of a system is determined by the ground state electron density in 1964 [150]. There are two theorems proven by Hohenberg and Kohn:

(1) For any system of interacting electrons in an external potential (V_{ext}), the total energy of a system can be represented as,

$$E[n(\boldsymbol{r})] = \langle\Psi|F + V_{\text{ext}}|\Psi\rangle = \langle\Psi|\hat{H}|\Psi\rangle, \tag{3.9}$$

where F is the combination of the kinetic energy and electron-electron Coulomb interaction, and V_{ext} is the external potential such as the Coulomb interaction from nuclei. If we imagine there are two different external potentials ($V_{\text{ext},1}$ and $V_{\text{ext},2}$) corresponding to the same density $n_0(\boldsymbol{r})$. The associated Hamiltonians ($\hat{H}_1$ and $\hat{H}_2$) have different ground-state wavefunctions (Ψ_1 and Ψ_2). The ground-state energy can be denoted as follows,

$$E = \langle\Psi_1|\hat{H}_1|\Psi_1\rangle < \langle\Psi_2|\hat{H}_1|\Psi_2\rangle, \tag{3.10}$$

so that,

$$E_1 < E_2 + \int n_0(\boldsymbol{r})(V_{\text{ext},1}(\boldsymbol{r}) - V_{\text{ext},2}(\boldsymbol{r}))d\boldsymbol{r}. \tag{3.11}$$

By interchanging Ψ_1 to Ψ_2 and $\hat{H}_1$ to $\hat{H}_2$, Eq. 3.10 becomes,

$$E_2 < E_1 + \int n_0(\boldsymbol{r})(V_{\text{ext},2}(\boldsymbol{r}) - V_{\text{ext},1}(\boldsymbol{r}))d\boldsymbol{r}. \tag{3.12}$$

Adding Eq. 3.11 and Eq. 3.12 bring us to an inconsistency,

$$E_1 + E_2 < E_2 + E_1. \tag{3.13}$$

Hence V_{ext} must be uniquely determined by the ground state electron density ($n_0(\boldsymbol{r})$)

(2) Since the theorem 1 proves that for any system the external potential is unique, the Hamiltonian of any system is unique as well. By using the variational method, the ground state total energy can be solved self-consistently,

$$E_0 = \langle\Psi_0|\hat{H}|\Psi_0\rangle < \langle\Psi_1|\hat{H}|\Psi_1\rangle = E_1, \tag{3.14}$$

where Ψ_0 and is the ground state wavefunction and E_0 represents the ground state total energy. However, Hohenberg and Kohn still left the interacting electron problem in the kinetic energy term.

Kohn and Sham determined a practical method for carrying out calculations based on the Hohenberg-Kohn theory in 1965. The kinetic energy, $\langle\psi(\boldsymbol{r}_1, \boldsymbol{r}_2 ... \boldsymbol{r}_N)|\hat{T}|\psi(\boldsymbol{r}_1, \boldsymbol{r}_2 ... \boldsymbol{r}_N)\rangle$, with interacting electrons is unknown. Rather than considering a system with interacting electrons, the Kohn-Sham model replaces the kinetic energy with many-body wavefunction into a kinetic energy using non-interacting wavefunctions (ψ_i) with same density as interacting wavefunctions. Next, the Kohn-Sham model established an exchange-correlation term involving the energy difference between many-body and non-interacting system. Hence, the total energy (in atomic units) is rewritten into,

$$E[n] = T_{\mathrm{s}}[n] + \int V_{\mathrm{ext}}(\boldsymbol{r}) n(\boldsymbol{r}) d\boldsymbol{r} + \frac{1}{2}\int\int \frac{n(\boldsymbol{r}) n(\boldsymbol{r}')}{|\boldsymbol{r} - \boldsymbol{r}'|} d\boldsymbol{r} d\boldsymbol{r}' + E_{\mathrm{xc}}[n], \tag{3.15}$$

where the T_{s} represents the kinetic energy of non-interacting electrons, the E_{xc} is the exchange-correlation energy and the third term on the right is the mean-field Coulomb (Hartree) interaction energy. The electron density of the system is given by,

$$n(\boldsymbol{r}) = \sum_{i}^{N} |\psi_i(\boldsymbol{r})|^2. \tag{3.16}$$

The independent-electron kinetic energy in Eq. 3.15 can be written as,

$$T_{\mathrm{s}}[n(\boldsymbol{r})] = -\frac{1}{2}\sum_{i}^{N} \nabla^2 \psi_i(\boldsymbol{r}), \tag{3.17}$$

where the ψ_i are the non-interacting electron wavefunctions and N is the total number of electrons in the system. Since the external energy, Hartree energy and exchange-correlation energy are an integral over the electron density, these energies can be written into a effective potential felt by the non-interacting electrons in the following way,

$$V_{\mathrm{eff}}(\boldsymbol{r}) = V_{\mathrm{ext}}(\boldsymbol{r}) + \frac{1}{2}\int \frac{n(\boldsymbol{r}')}{|\boldsymbol{r} - \boldsymbol{r}'|} d\boldsymbol{r}' + V_{\mathrm{xc}}[n(\boldsymbol{r})], \tag{3.18}$$

where the external potential (V_{ext}) represents the attractive potential between electrons and nuclei and the V_{xc} is the exchange-correlation potential and the second term on the right represents the mean-field Hartree potential. The Schrödinger-like equation for the Kohn-Sham method using non-interacting electrons i is shown below,

$$\big(-\frac{1}{2}\nabla^2 + V_{\mathrm{eff}}(\boldsymbol{r})\big)\psi_i(\boldsymbol{r}) = \varepsilon_i \psi_i(\boldsymbol{r}), \tag{3.19}$$

where the ε_i represents the single electron eigenenergy. The equation can be solved using the self-consistent field (SCF) method to find the ground state total energy. The SCF method is an iterative procedure, which involves selecting an initial electron density solving the Kohn-Sham equation to obtain an electron density corresponding to more stable system energy. The new electron density and effective potential are used to solve the equation again and repeated until the total energy is within a convergence tolerance.

3.2.2 Exchange-correlation functional

The Kohn-Sham method provides an explicit form using non-interacting electron wave-functions for solving the ground-state energy of a system. The exchange-correlation approximation controls the accuracy of the Kohn-Sham method and there are many good approximations of exchange-correlation functional. The simplest one is the local density approximation (LDA), the XC energy of the functional only depends on the electron density at the given point ($\boldsymbol{r}$) as follows,

$$E_{\mathrm{XC}}^{\mathrm{LDA}}[n(\boldsymbol{r})] = \int n[\boldsymbol{r}]\varepsilon_{\mathrm{XC}}^{\mathrm{LDA}}[n(\boldsymbol{r})]d\boldsymbol{r}, \tag{3.20}$$

where the $\varepsilon_{XC}^{LDA}[n(\boldsymbol{r})]$ is a XC density of the LDA functional. Eq. 3.20 can be separated into exchange and correlation terms,

$$E_{\mathrm{XC}}^{\mathrm{LDA}} = E_{\mathrm{X}}^{\mathrm{LDA}} + E_{\mathrm{C}}^{\mathrm{LDA}}. \tag{3.21}$$

Dirac developed an approximation for the exchange interaction based on the homogeneous electron gas yielding the expression, [151]

$$E_{\mathrm{X}}^{\mathrm{LDA}}[n(\boldsymbol{r})] = -\frac{3}{4}(\frac{3}{\pi})^{(1/3)}\int n(\boldsymbol{r})^{(4/3)}d\boldsymbol{r}^3. \tag{3.22}$$

Accurate values for correlation energy ($E_{\mathrm{C}}^{\mathrm{LDA}}$) for LDA have been determined using quantum Monte Carlo calculation [152]. Although the LDA functional works well, magnetic and open-shell properties require consideration of spins. Therefore, the LDA functional is extended into spin-polarised expression,

$$E_{\mathrm{XC}}^{\mathrm{LSDA}}[n_\alpha(\boldsymbol{r}), n_\beta(\boldsymbol{r})] = \int n[\boldsymbol{r}]\varepsilon_{\mathrm{XC}}^{\mathrm{LSDA}}[n_\alpha(\boldsymbol{r}), n_\beta(\boldsymbol{r})]d\boldsymbol{r}, \tag{3.23}$$

where $\varepsilon_{\mathrm{XC}}^{\mathrm{LSDA}}$ is a XC density of the local spin density approximation (LSDA) functional, the $n_\alpha(\boldsymbol{r})$ and $n_\beta(\boldsymbol{r})$ represent the spin up and spin down electron densities.

The LDA (LDSA) functional is based on a homogeneous electron gas and describes XC energy solely on the value of electron density at each point in space. The LDA (LDSA) functional usually predicts too large binding energy and underestimates the lattice parameters (bond lengths) and band gaps. In order to overcome the underestimation from LDA (LDSA) functional, Langreth and Mehl applied gradient corrections to the LDA (LDSA) functional [153]. Hence, the generalised gradient approximation (GGA) including a first order derivative of the density is introduced as another approximation of the XC functional. Moreover, the parameter of electron spin is also included in GGA XC functional. Many different GGA functionals have been determined by fitting to the experimental data or first principles calculations [154]. The general formulation of the GGA functional is as follows,

$$E_{\mathrm{XC}}^{\mathrm{GGA}}[n(\boldsymbol{r})] = \int n(\boldsymbol{r})\varepsilon_{XC}^{GGA}[n(\boldsymbol{r}), \nabla n(\boldsymbol{r})]d\boldsymbol{r}, \tag{3.24}$$

where $\varepsilon_{XC}^{GGA}[n(\boldsymbol{r}), \nabla n(\boldsymbol{r})]$ represent the exchange correlation density of GGA function and $\nabla n(\boldsymbol{r})$ indicates the functional depending not only on electron density at a given point and also on derivatives of the density. It decreases the error about two orders magnitude in exchange correlation energy relative to the LDA result. In this thesis, the main exchange-correlation functional used is the GGA by John P. Perdew, Kieron Burke and Matthias Ernzerhof (PBE) [155].

3.2.3 Brillouin zone sampling

The total energy of DFT calculations are an integral over the Brillouin zone. However, it is impossible to sample all k-points for each electron. Monkhorst and Pack determined a method for generating sets of special points in the Brillouin zone (Monkhorst-Pack (MP) grid) in order to sample the wave vector $\boldsymbol{k}$ in reciprocal space [156]. The $k-$point sampling uses an equally spaced mesh sampling the Brillouin zone and applying point-group symmetry to significantly reduce the number of distinct sampled points. Fig. 3.3 illustrates the total sampled k-points and the reduced k-points in a square reciprocal lattice. The figure shows the reduction can decrease the calculation times depending on the shape of the Brillouin zone. After the reduction, all points are irreducible in three dimensions. In the computation, each dimension (x, y and z) of the supercell should be assigned a number representing the sampling grids. The representation of the total energy

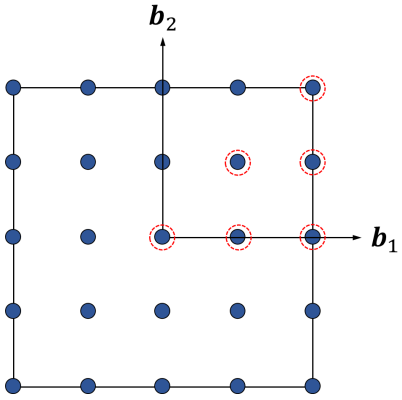

Figure 3.3: Illustration of k-point sampling. The blue points represent the sampling points in the first Brillouin zone (black squared line) for a total energy calculation. The red dashed circles indicate the irreducible points for the Brillouin zone.

is in the following,

$$E = \sum_{i,k} \frac{1}{N_k} \varepsilon_{i,k} f_{i,k}, \tag{3.25}$$

where N_k is the total number of $k-$points, k represent the $k-$points and the f_i is the Fermi-Dirac occupation coefficient ($0 \leq f_i \leq 1$). The energy convergence with respect to the number of k-points should be examined in calculations. For bulk calculations, it is necessary to use three integer values for three-dimensional k-point sampling. However, for a surface calculation with a vacuum gap along the z-axis normal to the surface, the k-point mesh should only lie on xy plane to decouple the energy influence of the repeated slabs in z-direction.

3.2.4 Plane wave basis set

In order to carry out calculations using DFT, a basis set is used to represent single-particle wavefunctions in the Kohn-Sham equations. There are several basis functions developed, such as plane-waves and atomic orbitals. The former one using the superposition principle assembles many periodic plane-waves together to describe the wavefunction in a crystal. The latter one uses functions (such as hydrogen orbitals or Gaussian functions) to imitate the complicated atomic orbitals. Since the plane-wave basis set offers good symmetric convergence and computational feasibility, the calculations in this thesis use a plane wave basis set.

Since $u(\boldsymbol{r})$ is a periodic potential, it can be expanded into a terms of a Fourier series with the reciprocal lattice $\boldsymbol{G}$,

$$u(\boldsymbol{r}) = \sum_{\boldsymbol{G}} C_{\boldsymbol{k},\boldsymbol{G}} e^{-i\boldsymbol{G}\cdot\boldsymbol{r}}. \tag{3.26}$$

where $C_{\boldsymbol{k},\boldsymbol{G}}$ are the plane wave expansion coefficients. Thus, the wavefunction of one electron of Eq. 3.4 can be rewritten as a linear combination of plane waves,

$$\psi_{\boldsymbol{k}}(\boldsymbol{r}) = \sum_{\boldsymbol{G}} C_{\boldsymbol{k},\boldsymbol{G}} e^{i(\boldsymbol{k}+\boldsymbol{G})\cdot\boldsymbol{r}}. \tag{3.27}$$

The periodic function sums over all space and the $\boldsymbol{k}+\boldsymbol{G}$ controls the accuracy of the calculation. Assuming the coefficient decreases rapidly with increased $\boldsymbol{k}+\boldsymbol{G}$, a cut-off value is defined to improve the calculation in accuracy. Therefore, the kinetic energy of plane wave $e^{i(\boldsymbol{k}+\boldsymbol{G})\cdot\boldsymbol{r}}$ is used to determine the truncation of number of plane waves required,

$$E_{\text{cut}} \geq \frac{|\boldsymbol{k}+\boldsymbol{G}|^2}{2}. \tag{3.28}$$

where the E_{cut} is the cut-off energy. The cut-off specifies that plane waves with energies less than E_{cut} are included in a calculation. Although reducing the cut-off energy can improve the computational performance, the result may be not properly converged if the cut-off energy is too low. A total energy convergence should be examined before any calculations.

3.2.5 Pseudopotential

The total effective potential in the Kohn-Sham equations is a summation of mean field Coulomb potential from the valence electrons (the Hartree potential), exchange-correlation potential and the external potential. The external potential represents the Coulomb interaction between electron and nuclei. Due to the $1/r$ attraction from nucleus to electron, the wavefunction varies vary quickly near the nucleus. It would take many plane-waves to model the wavefunction in this region for a precise description. Fortunately, the core electrons (which are closest to the nucleus) are tightly bound to the ion and most of the interesting properties and interactions are between the valence electrons. Therefore, the dramatically attractive Coulomb potential can be replaced by a smooth pseudopotential (PP). By using a pseudopotential the core states are explicitly included (but not the same

as all-electron situation), thus the pseudo-wavefunction becomes smoother near the nucleus. A cut-off distance (r_c) is defined such that the pseudo-wavefunction has the same behaviour as the all-electron wavefunction when $r > r_c$,

$$\psi^{PP}(r > r_c) = \psi^{AE}(r > r_c), \tag{3.29}$$

where ψ^{PP} and ψ^{AE} represent the pseudo-wavefunction and the all-electron wavefunction, respectively. In addition, the eigenvalues of the pseudopotential method are the same as the all electron calculation,

$$\varepsilon_i^{PP} = \varepsilon_i^{AE}. \tag{3.30}$$

There are a few types of pseudopotential, such as norm-conserving, ultrasoft and projector augmented wave methods. The norm-conserving method, shown in Fig. 3.4(a), ensures that the integrated charge for each pseudo-wavefunction (ψ^{PS}) is consistent with the all electron wavefunction (ψ^{AE}) in the region ($r > r_c$),

$$\int_0^r |\psi^{PS}|^2 r^2 dr = \int_0^r |\psi^{AE}|^2 r^2 dr. \tag{3.31}$$

The pseudo-wavefunction in the norm-conserving method is much smoother than the full atomic potential, though still requires a high plane-wave cutoff. Therefore, the ultrasoft method, shown in Fig. 3.4(b), is introduced to reduce the number of plane-waves in the calculation. In order to make the pseudo-wavefunction smoother, Vanderbilt split the pseudo-wavefunction into a pseudo-wavefunction, which does not fulfil the norm conservation (Eq. 3.31), and a core augmentation charge (which is not involved in the calculation) [157]. Hence, the pseudo-wavefunction in the ultrasoft method becomes very smooth and the calculation time can be speeded up by use of a reduced cut-off energy.

In 1994, Blochl introduced the projector augmented wave (PAW) method to offer a elegant approximation to the pseudo-wavefunction. The approach is to use pseudo-wavefunction ($\tilde{\psi}$) to represent the all electron wavefunction [158]. The representation is,

$$|\psi\rangle = \mathcal{T}|\tilde{\psi}\rangle, \tag{3.32}$$

where ψ is the all electron wavefunction and $\mathcal{T}$ is the linear transformation from pseudo-wavefunction to all electron wavefunction. The two wavefunctions only differ in the region Ω_R near to the ion. The pseudo-wavefunction can be expanded into partial waves in Ω_R,

$$|\tilde{\psi}\rangle = \sum_i |\tilde{\phi}_i\rangle c_i. \tag{3.33}$$

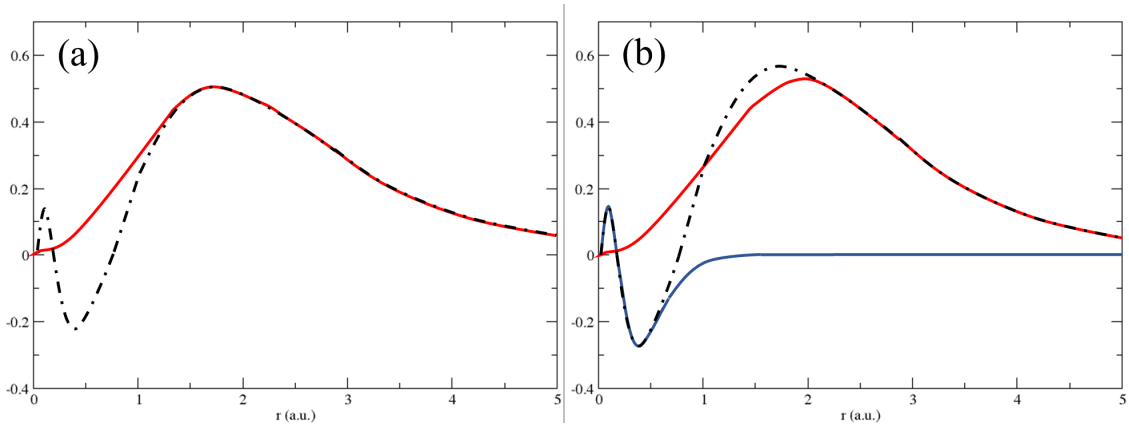

Figure 3.4: Illustration of the pseudo wavefunctions (red solid lines) and all-electron wavefunctions (black dashed line). (a) and (b) represent the the norm-conserving and ultrasoft method. The blue solid line in (b) represents the core augmentation charge which is the difference between the all-electron and the pseudo wavefunctions in ultrasoft method.

The all electron wavefunction can be expanded into,

$$|\psi\rangle = \sum_i |\phi_i\rangle c_i, \tag{3.34}$$

where $\tilde{\phi}_i$, ϕ_i and c_i are the partial waves of the pseudo-wavefunction, partial wave of all electron wavefunction and the coefficients, respectively. Therefore, the all electron wavefunction can be written as,

$$|\psi\rangle = |\tilde{\psi}\rangle + \sum_i |\phi_i\rangle c_i - \sum_i |\tilde{\phi}_i\rangle c_i. \tag{3.35}$$

c_i are given by a scalar product,

$$c_i = \langle p_i|\tilde{\psi}\rangle, \tag{3.36}$$

where p_i is the projector functions and $\langle p_i|\tilde{\phi}_j\rangle = \delta_{ij}$. Eq. 3.35 can be rewritten into,

$$|\psi\rangle = |\tilde{\psi}\rangle + \sum_i \big(|\phi_i\rangle - |\tilde{\phi}_i\rangle\big)\langle p_i|\tilde{\psi}\rangle. \tag{3.37}$$

Then T is equal to,

$$\mathcal{T} = 1 + \sum_i \big(|\phi_i\rangle - |\tilde{\phi}_i\rangle\big)\langle p_i|. \tag{3.38}$$

The three quantities determine this transformation and access to the all electron wavefunction using the pseudo-wavefunction and partial waves.

3.3 Beyond Standard DFT

3.3.1 Hubbard U correction

DFT calculations using LDA and GGA exchange-correlation functionals are successful in predicting many physical properties e.g. lattice constant and formation enthalpy. The electron-electron interaction energies in DFT are defined as the Hartree term (classical Coulomb interaction) and exchange-correlation energy approximating the many-body interaction. However, the former Hartree energy involves a mean-field electrostatic energy introducing electron self-interaction, resulting in incorrectly delocalised electrons in many cases. The delocalisation fails to describe the defect formation energy in some transition metal oxides as well as underestimates the band gap of insulators, such as CoO, NiO, FeO and ZnO [108, 159]. In order to localise the electrons correcting the self-interaction especially for open shells, Liechtenstein et al. applied a Hubbard-like term within the DFT calculation [160]. The Hubbard U parameter is an on-site electron-electron interaction to enhance the correlation energy between electrons especially for d and f orbitals. The general expression for the Hubbard-like U correction is,

$$E_{\mathrm{LDA+U}}[n(\boldsymbol{r})] = E_{\mathrm{LDA}}[n(\boldsymbol{r})] + E_{\mathrm{Hub}}[n^{I\sigma}_{mm\prime}] - E_{\mathrm{dc}}[n^{I\sigma}], \tag{3.39}$$

where the E_{Hub} represents the on-site electron-electron interaction energy for atomic site I, the σ indicates the spin state, the $n^{I\sigma}_{mm\prime}$ is the occupation number of localised states and the E_{dc} is the double-counting term for cancelling the correlation energy as a mean-field approximation contributed by E_{Hub} term. The occupation number is defined as a projection of Kohn-Sham wavefunctions, $\psi^{I\sigma}_{kv}$, on localised states, such as atomic orbitals ϕ^{I}_{m},

$$n^{I\sigma}_{mm\prime} = \sum_{i} f^{\sigma}_{kv} \langle \psi^{\sigma}_{i} | \phi^{I}_{m\prime} \rangle \langle \phi^{I}_{m} | \psi^{\sigma}_{i} \rangle, \tag{3.40}$$

where the f^{σ}_{kv} are the Fermi-Dirac occupations of the localised states ($0 \leq f^{\sigma}_{kv} \leq 1$), k and v are the k-point and band indexes, respectively. A simplified representation of Hubbard

U method is determined by Dudarev et al, the formulation is as follows [161],

$$\begin{aligned} E_{\mathrm{U}} &= E_{Hub}[n^I_{mm'}] - E_{dc}[n^I] \\ &= \sum_I \frac{U^I}{2}\left[(n^I)^2 - \sum_\sigma \mathrm{Tr}\big[(\boldsymbol{n}^{I\sigma})^2\big]\right] - \sum_I \frac{U^I}{2} n^I(n^I-1) \\ &= \sum_{I\sigma} \frac{U^I}{2}\mathrm{Tr}\Big[\boldsymbol{n}^{I\sigma}(1-\boldsymbol{n}^{I\sigma})\Big]. \end{aligned} \tag{3.41}$$

where the Tr represents the trace of the occupation number matrix ($\boldsymbol{n}^{I\sigma}$). The corresponding potential due to the Hubbard U is given by the derivative of Eq. 3.41 with respect to the atomic occupation number,

$$V_{\mathrm{U}} = U^I(\frac{1}{2}\delta_{mm'} - \boldsymbol{n}^{\sigma}_{mm'}). \tag{3.42}$$

Therefore, if an orbital is more than half occupied by electrons ($\boldsymbol{n}^{\sigma}_{mm'} > \frac{1}{2}$), the Hubbard potential localises these electrons by reducing their total energy. Conversely, the electrons are delocalised when an orbital is less than half-filled ($\boldsymbol{n}^{\sigma}_{mm'} < \frac{1}{2}$).

3.3.2 Non-local external potential (NLEP)

A notable failure of standard DFT calculations is the significantly underestimated band gap for the transition-metal oxides, such as CoO, NiO, FeO and ZnO. Although the Hubbard U method is able to localise the d and f electrons expanding the band gap to a certain extent, the gap energy is still too small with respect to experimental observations. The incorrect band gap may lead an unexpected charge transfer at an interface (especially the calculation in Chapter 6). In addition, the Hubbard U method can distort the O-p bands in a uncontrolled way e.g. in doped SiO_2 calculations [162]. To address this issue, Christensen applied an external potential (δ function-like) on s orbitals producing an up-shift of the s-like conduction band to adjust the gap energy for GaAs calculation [163]. Although the potential is Hubbard U like, it is independent on the orbital occupancy. Wang followed a similar approach but using the non-local external potential to modify the pseudopotential on s, p and d orbitals with respective fitted parameters for $GaAs_{(1-x)}N_x$ calculation [164]. The calculation shows good agreement of band gap with experiment and additionally obtained a localised nitrogen state in GaAsN. However, in order to allow more flexibility in fitting experimental value of ZnO gap, the formulation is rewritten as an

angular-momentum-dependent (nonlocal) potentials [108]. The expression of the potential is as follows,

$$V_{\mathrm{NLEP}}(r') = \beta \sin(r'\pi/r_{\mathrm{nlep}})/r', \tag{3.43}$$

where β is a fitted parameter, r' equals the distance between electron and nucleus and r_{nlep} represents a cut-off distance. The external potential vanishes to zero outside r_{nelp}, the usual cut-off distance range is between 0.8 to 1.1 Å. In addition, the non-local external potential depends upon different atomic types and angular momenta. Using the combination of LDA, NLEP and the Hubbard U method (LDA+NLEP+U), the band gap is corrected self-consistently for transition metal oxides and uncontrolled bands are restored as well [108, 164].

3.3.3 Hartree-Fock theory and hybrid DFT

This subsection briefly describes Hartree-Fock theory and hybrid DFT. Although these methods are not implemented in any study in this thesis, it still plays an important role in first principle calculations with hybrid functionals.

The Hartree-Fock method is an approximation to the many electron Schrödinger equation using a single Slater determinant of single-particle wavefunctions as an approximation to the many-particles wavefunction [165]. The Slater determinant is written as,

$$\Psi_{Slater}(\boldsymbol{r}_1, \boldsymbol{r}_2, \boldsymbol{r}_3, ...\boldsymbol{r}_n) = \frac{1}{\sqrt{N!}} \begin{bmatrix} \phi_1(\boldsymbol{r}_1) & \phi_2(\boldsymbol{r}_1) & \cdots & \phi_N(\boldsymbol{r}_1) \\ \phi_1(\boldsymbol{r}_2) & \phi_2(\boldsymbol{r}_2) & \cdots & \phi_N(\boldsymbol{r}_2) \\ \vdots & \vdots & \ddots & \vdots \\ \phi_1(\boldsymbol{r}_N) & \phi_2(\boldsymbol{r}_N) & \cdots & \phi_N(\boldsymbol{r}_N) \end{bmatrix}, \tag{3.44}$$

where N is the number of total electrons and ϕ_i represents the spin-orbital and each function is a product of a spatial part ψ_i and a spin variable σ (where the σ represents the spin up, α, or spin down, β). By applying the single Slater determinant as a wavefunction to the Hamiltonian,

$$\hat{H} = \Big(-\frac{1}{2}\nabla^2 + V_{\mathrm{ext}}(\boldsymbol{r}) + \frac{1}{|\boldsymbol{r} - \boldsymbol{r}'|} \Big), \tag{3.45}$$

The total energy of Hartree-Fock approximation results in the following,

$$\begin{aligned} E_{\mathrm{HF}} = \langle\Psi|\hat{H}_{HF}|\Psi\rangle = \sum_i \int \psi_i{}^*(\boldsymbol{r}_i)[-\frac{1}{2}\nabla^2 + V_{\mathrm{ext}}(\boldsymbol{r})]\psi_i(\boldsymbol{r}_i)d\boldsymbol{r} \\ + \frac{1}{2}\sum_{i,j}\int \psi_i{}^*(\boldsymbol{r}_i)\psi_j{}^*(\boldsymbol{r}_j)\frac{1}{|\boldsymbol{r}_i - \boldsymbol{r}_j|}\psi_i(\boldsymbol{r}_i)\psi_j(\boldsymbol{r}_j)d\boldsymbol{r}_i d\boldsymbol{r}_j \\ - \frac{1}{2}\sum_{i,j}\int \psi_i{}^*(\boldsymbol{r}_i)\psi_j{}^*(\boldsymbol{r}_j)\frac{1}{|\boldsymbol{r}_i - \boldsymbol{r}_j|}\psi_j(\boldsymbol{r}_i)\psi_i(\boldsymbol{r}_j)d\boldsymbol{r}_i d\boldsymbol{r}_j, \end{aligned} \tag{3.46}$$

where $-\frac{1}{2}\nabla^2$ and $V_{\mathrm{ext}}(\boldsymbol{r})$ represent the kinetic energy and external potential, respectively, the second term on the right is the Hartree energy and the third term indicates the exchange energy. Therefore, Hartree-Fock method can be rewritten as a Schrödinger-like equation,

$$\big[-\frac{1}{2}\nabla^2 + V_{\mathrm{ext}}(\boldsymbol{r}) + \hat{J} + \hat{K}\big]\psi_i(\boldsymbol{r}) = \varepsilon_i\psi_i(\boldsymbol{r}). \tag{3.47}$$

where $\hat{J}$ is the Coulomb operator and $\hat{K}$ represents the exchange operator. Eq. 3.47 is also presented as,

$$\hat{\mathrm{F}}\psi_i(\boldsymbol{r}) = \varepsilon_i\psi_i(\boldsymbol{r}), \tag{3.48}$$

where $\hat{\mathrm{F}}$ is the Fock operator. The expensive calculation of exchange integration means it is not a feasible method for many material studies. In Hartree-Fock theory, the exchange energy is explicitly determined in an *ab initio* calculation. Therefore, the correlation energy can be defined as,

$$E_{\mathrm{c}} = E_{\mathrm{exact}} - E_{\mathrm{HF}}, \tag{3.49}$$

where E_{exact} represents the total energy of the exact result from the many-body wave-function.

In order to improve the calculation accuracy, Axel introduced the hybridisation of standard DFT and some Hartree-Fock (exact) exchange energy [166]. The formulation of the hybrid is usually a linear combination of the exact exchange and other explicit exchange and correlation energy (such as LDA and GGA). One example of hybrid DFT is PBE0, the exchange-correlation energy of PBE0 functional is expressed as [167],

$$E_{\mathrm{xc}}^{\mathrm{PBE0}} = \frac{1}{4}E_{\mathrm{x}}^{\mathrm{HF}} + \frac{3}{4}E_{\mathrm{x}}^{\mathrm{PBE}} + E_{\mathrm{c}}^{\mathrm{PBE}}, \tag{3.50}$$

where $E_{\mathrm{x}}^{\mathrm{HF}}$ is the HF exchange energy shown in Eq. 3.46 (the third term on the right side), $E_{\mathrm{x}}^{\mathrm{PBE}}$ and $E_{\mathrm{c}}^{\mathrm{PBE}}$ are the exchange and correlation energy of PBE functional, respectively. Each coefficient determines the weight of either the exchange and correlation energy in the calculation. The empirical parameters are usually fitted to experimental observations.

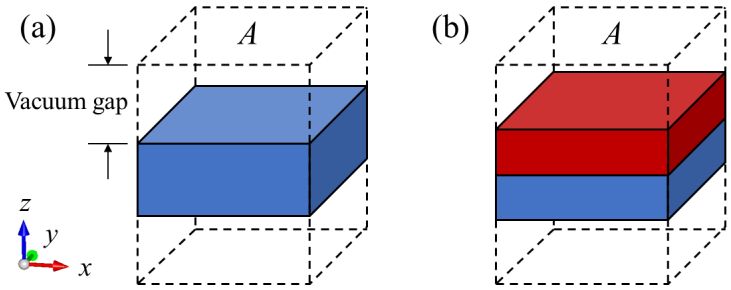

Figure 3.5: Sketches show (a) single slab and (b) double slabs in the supercell approach with the vacuum gap along the z-axis. A represents the cross-sectional area of the supercells.

3.4 Analysis and Prediction of Nanostructures

3.4.1 Surface formation energy and adhesion energy

In order to assess the stability of different cleaved surfaces, especially the low-index surfaces in this thesis, the formation energy is the simplest quantity for comparison. In addition, the formation energy can be used for predicting the morphology of specific nanoparticles which will be discussed in later section 3.4.4. Fig. 3.5(a) demonstrates the slab approach in a supercell (black-dashed box), while (b) showing two slabs attaching together. The surfaces of the slab are perpendicular to the vacuum gap along the z-axis and periodic in xy plane. The formation energy is given as follows,

$$\gamma = \frac{1}{2A}(E_{\text{slab}} - \sum_i N_i \mu_i), \tag{3.51}$$

where A is the cross-sectional area of the surface of the supercell normal to the vacuum gap, E_{slab} is the total energy of the specific slab, N_i and μ_i represent the number of atoms and the chemical potential of material component i, respectively. The unit of the formation energy is usually J/m^2 and the calculated formation energy of surfaces should always be positive indicating that it is less stable than the bulk.

Generally, surface terminations of binary materials can be inequivalent leading different surface configurations depending on the chemical potential. Chemical potentials in compounds can adopt a range of values depending on the ambient environment. For

example, the chemical potentials of bcc Fe and fcc Pt in the bulk configurations are,

$$\mu_{\mathrm{Fe}}^{\mathrm{bulk}} = E_{\mathrm{Fe}}^{\mathrm{bcc}}, \qquad \mu_{\mathrm{Pt}}^{\mathrm{bulk}} = E_{\mathrm{Pt}}^{\mathrm{fcc}}, \tag{3.52}$$

where $E_{\mathrm{Fe}}^{\mathrm{bcc}}$ and $E_{\mathrm{Pt}}^{\mathrm{fcc}}$ are the total energy of bulk Fe and Pt. The chemical potentials between Fe and Pt are independent. However, once Fe and Pt form the bulk alloy FePt, both chemical potentials corresponds to the total energy of Fe-Pt pair in bulk FePt, E_{FePt}. The chemical potential of FePt is defined,

$$\mu_{\mathrm{FePt}}^{\mathrm{bulk}} = \mu_{\mathrm{Fe}} + \mu_{\mathrm{Pt}} = \mu_{\mathrm{Fe}}^{\mathrm{bulk}} + \mu_{\mathrm{Pt}}^{\mathrm{bulk}} - \Delta\mu_{\mathrm{FePt}}, \tag{3.53}$$

where, $\Delta\mu_{\mathrm{FePt}}$ is the formation energy of FePt. Therefore, the available μ_{Fe} and μ_{Pt} are the values in the ranges,

$$\mu_{\mathrm{Fe}}^{\mathrm{bulk}} - \Delta\mu_{\mathrm{FePt}} \leq \mu_{\mathrm{Fe}} \leq \mu_{\mathrm{Fe}}^{\mathrm{bulk}}, \tag{3.54}$$

and

$$\mu_{\mathrm{Pt}}^{\mathrm{bulk}} \geq \mu_{\mathrm{Pt}} \geq \mu_{\mathrm{Pt}}^{\mathrm{bulk}} - \Delta\mu_{\mathrm{FePt}}. \tag{3.55}$$

The choice of the chemical potentials are dependent on the ambient environment, if the system is Fe-rich, then μ_{Fe} is close to $\mu_{\mathrm{Fe}}^{\mathrm{bulk}}$ and μ_{Pt} close to $\mu_{\mathrm{Pt}} - \Delta\mu_{\mathrm{FePt}}$.

Apart from the surface stability, the interaction between two different surfaces is also an important issue for understanding epitaxial growth and lattice mismatch. In order to quantify surface interactions and interfacial geometry, we calculate the adhesion energy to describe the stability further predicting the favourable orientations for two surfaces. The adhesion calculation involves three total energies, which are two isolated surfaces in individual supercells and one supercell including two surfaces attaching together,

$$\gamma_{\mathrm{ad}} = \frac{1}{A}(E_{\mathrm{tot}} - E_{\mathrm{B}} - E_{\mathrm{C}}), \tag{3.56}$$

where E_{tot} is the total energy of the system with two slabs attaching together, E_{B} and E_{C} are the total energy of isolated slabs and A is the cross-sectional area of attaching region. The conventional unit for the adhesion energy is also $\mathrm{J/m^2}$. A negative adhesion energy characterises two slabs that preferentially attach together, whereas a positive result showing the interfacial structure is unstable.

3.4.2 Native point defect formation energy

The defect formation energy determines the equilibrium concentration and the thermodynamically stable charge state of point defects. The defect formation energy is defined as,

$$E_{\mathrm{f}} = E_{\mathrm{d}}^{q} - E_{\mathrm{p}} + \sum_{i} n_i \mu_i + q(E_{\mathrm{F}} - \Delta V) + E_{\mathrm{ic}} \tag{3.57}$$

where E_{d}^{q} is the total energy of the supercell containing the defect in the charge q and E_{p} represents the total energy of pristine supercell. The chemical potential μ_i relates to the reservoir of atom i, while n_i equals +1 and -1 represent removing or adding atoms to the pristine crystal. E_{F} describes the Fermi energy (highest occupied level). The ΔV is the electrostatic potential correction term. Finally, the E_{ic} represents the energy correction for finite size effects to the point defect under periodic boundary conditions. The electrostatic potential correction, ΔV, aligns the Fermi energy between the defect and pristine calculations defined as follows,

$$\Delta V = V_{\mathrm{i}}^{\mathrm{d}} - V_{\mathrm{i}}^{\mathrm{p}}, \tag{3.58}$$

where $V_{\mathrm{i}}^{\mathrm{p}}$ and $V_{\mathrm{i}}^{\mathrm{d}}$ are the electrostatic potential for particular atom i of the pristine and defected system (the atom i is both systems must be the same atom). The chosen atom i should be far from the defect preventing the influence from the defect. In the ideal case, the point defect calculation is modelling a single defect in a perfect crystalline structure. In the neutral defect calculation, the periodic boundary conditions do not significantly impact the calculated formation energy. However, the charged defect feels the electrostatic interaction from the other defects which belongs to the periodic images. The simplest and original energy correction for this effect uses the Madelung energy to describe the interaction energy (E_{ic}^{1}) of an array of point charges with neutralising jellium [168]. Later on, Makov and Payne introduced a third order point-charge image term (E_{ic}^{3}) of defect [169]. Hence, the image charge correction can be written as,

$$E_{\mathrm{ic}} = E_{\mathrm{ic}}^{1} + E_{\mathrm{ic}}^{3} = \frac{q^2 \alpha}{2\varepsilon L} + \frac{2\pi q Q}{3\varepsilon L^3} \tag{3.59}$$

where $L = \Omega^{-1/3}$ is the linear supercell dimension (Ω is the supercell volume), q is the charge of the point defect, ε represents the static dielectric constant of the material and Q is the integral $\int_{\Omega} \rho(\boldsymbol{r}) r^2 dr^2$ (where $\rho(\boldsymbol{r})$ is the charge density within the supercell). The first term on the right of Eq. 3.59 is the Madelung-like energy, E_{ic}^{1}, is the dipole correction.

The second term, $E^3_{\rm ic}$, represents the interaction of point-charge images. However, the delocalised electron screening significantly reduces the magnitude of the second term. Lany and Zunger rewrote a simpler expression for the finite size correction [162, 170],

$$E_{ic} = \frac{2}{3} E^1_{\rm ic}. \tag{3.60}$$

Finally, the modified formula yields a simple but accurate image-charge correction for predicting the formation energy of point defects.

3.4.3 Adsorption energy, strain energy and free energy

In order to compare the stabilities of different molecular adsorptions (with the same number of adsorbed atoms) on the nanoparticles, the average adsorption energy is used to capture the most stable configuration. The average adsorption energy is defined as,

$$E_{\rm ad} = \frac{1}{N_{\rm ad}} (E^{\rm ad}_{\rm NP} - E_{\rm NP}), \tag{3.61}$$

where $E^{\rm ad}_{\rm np}$ is the total energy of a nanoparticle with adsorbed atoms, $E_{\rm np}$ represents the total energy of a pure nanoparticle and $N_{\rm ad}$ means the number of adsorbed atoms. Atoms adsorbing on a nanoparticle may contribute strain on a nanoparticle. Hence, the strain energy is calculated to characterise the distortion on the nanoparticle due to the adsorption. The strain energy involves two total energies,

$$E_{\rm strain} = E^{\rm ad\,\prime}_{\rm NP} - E_{\rm NP}, \tag{3.62}$$

where $E^{\rm ad\,\prime}_{\rm NP}$ is the total energy of a bare nanoparticle but its geometry is optimised corresponding to the adsorbed nanoparticle. To assess the thermodynamic stability for nanoparticles with different number of adsorbed atoms, we computed the free energy,

$$G = E^{\rm ad}_{\rm np} - N_{\rm ad}\mu_{\rm ad} \tag{3.63}$$

where $N_{\rm ad}$ represents the number of adsorbed atoms on a nanoparticle and $\mu_{\rm ad}$ indicates the chemical potential of an adsorbed atom. The chemical potential depends on the ambient conditions (such as temperature and pressure). Therefore, a phase diagram can be used to illustrate the thermodynamic stability of nanoparticles for a range of chemical potential. The range of a chemical potential is usually between upper and lower boundaries as discussed in section 3.4.1.

3.4.4 Wulff and Wulff-Kaichew construction

The surface formation energy of a facet plays a significant role in the formation of nanoparticles [171]. The surface free energy of a nanoparticle is defined as,

$$G_{\mathrm{s}} = \int \gamma(\theta, \phi) dA, \tag{3.64}$$

where $\gamma(\theta, \phi)$ is a polar function describing a distance of a facet normal from a common centre in a nanoparticle and A is the area of the facet. With the integration for a faceted nanoparticle, Eq. 3.64 becomes a function of surface formation energies,

$$G_{\mathrm{s}} = \sum_{i} \gamma_i A_i, \tag{3.65}$$

where γ_i is a surface formation energy which is calculated using Eq. 3.51 with particular miller index i and A_i represents the area of the particular facet. The Wulff construction determines the shape of nanoparticle which minimises the total surface energy for a given volume. The Wulff construction of an equilibrium shape is illustrated in Fig. 3.6(a). The vectors from the centre point to the surfaces (dashed lines) indicating the possible surfaces for a nanoparticle and the lengths of vectors are proportional to their respective surface formation energy (γ_i). The area (volume) enclosed by the most inner dashed lines is the Wulff shape (solid lines) which minimises the total surface energy. The surface (12) possesses a relatively high formation energy, so it is not present on the Wulff shape. The above construction in only available for single-crystalline structures and free nanoparticles indicating it cannot predict supported nanoparticles. To model supported nanoparticles, the formation energy of the interface should be rewritten as $\gamma_i + \gamma_{\mathrm{ad}}$ to modify the formation energy in that specific orientation. Fig. 3.6(b) shows the illustration of Wulff-Kaichew construction, the length of the normal distance from the common centre to interface is shorter than the free nanoparticle. The reason is that the attached nanoparticle usually has a negative adhesion energy, thus $\gamma_i + \gamma_{\mathrm{ad}}$ is less than γ_i. The choice of the interface between epitaxial grown nanoparticles and substrates depends on the stability of the adhesion energy.

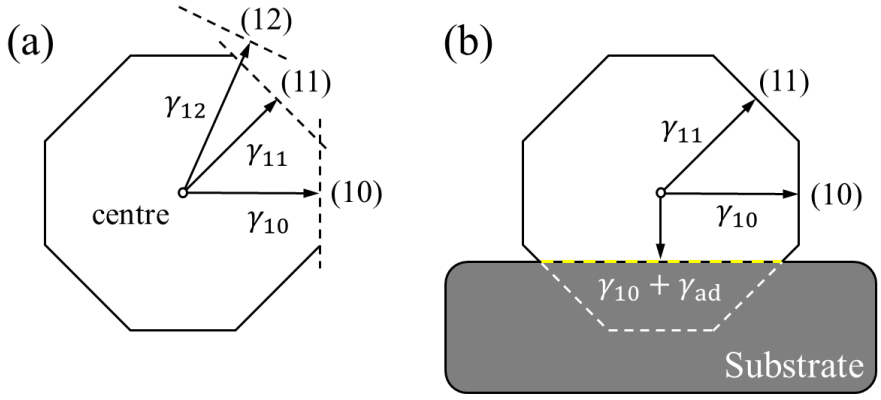

Figure 3.6: An illustration of Wulff construction (a) and Wulff-Kaichew construction (b) in two dimensions. The surface (10) is equivalent to surface (01).

3.4.5 Interpolated images for diffusion calculation

In order to estimate the mobility of atom diffusion in crystals or nanoparticles, we employ the constrained optimisation approach to calculate energy barriers. Before the constrained optimisation, the structures of two endpoints are optimised with only the diffusing atom in the different position. Next, a few intermediate structures involving the diffusing atom along the diffusion pathway are obtained by linear interpolation between initial ($\boldsymbol{R}_\mathrm{i}$) and final ($\boldsymbol{R}_\mathrm{f}$) configurations (endpoints),

$$\boldsymbol{R}(t) = (1-t)\boldsymbol{R}_\mathrm{i} + t\boldsymbol{R}_\mathrm{f} \tag{3.66}$$

where t is an interpolation parameter in the range of 0 to 1 controlling the position of the diffusing atom. For example, if there are three interpolated images between the initial and final structures (shown in Fig. 3.7(a) and (e)), the parameter t is 0.25, 0.50 and 0.75 representing the first, second and third intermediate structure (shown in Fig. 3.7(b)-(d)), respectively. The generation of the interpolated images is performed using VASP Transition State Tools (VTST) script [172]. The total energy of the intermediate configurations are optimised with respect to the position of all atoms within a given radius (with the diffusing atom held fixed) and the atoms outside the sphere also fixed. For demonstrating energy barriers of a diffusing atom, a proper radius should not influence other adatoms during the optimisation. Therefore, a 4 Å radius is selected to apply the constrained optimisation, which provides a good description of the localised distortion with respect to the atom diffusion.

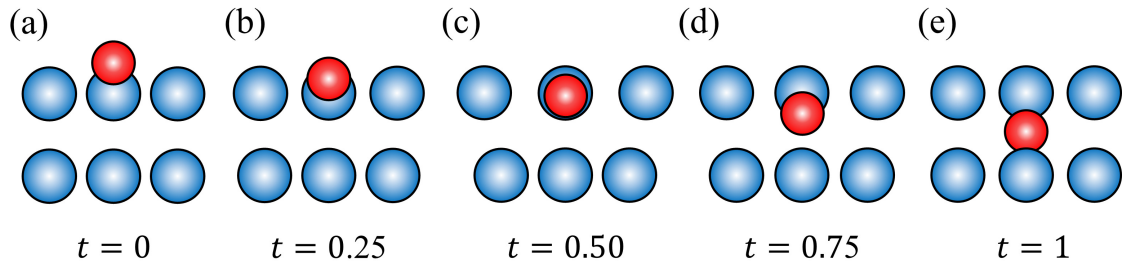

Figure 3.7: The linear interpolated images. (a) and (e) are the initial and final images. (b)-(d) are the intermediate images. The penetration pathway of the red sphere is from top to bottom.

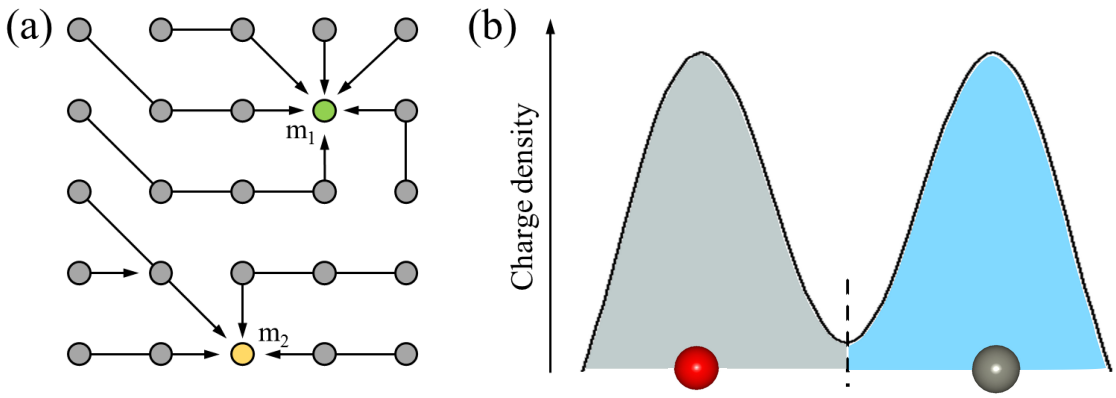

Figure 3.8: Illustration shows (a) the rearrangement of electronic density to the maxima (m_i, green and yellow points) following along the steepest gradient (arrows) and (b) the zero flux surface (black-dashed line) allocating the electronic density into different ions (red and sliver spheres). The coloured spheres in (a) and (b) are inequivalent.

3.4.6 Bader analysis

In DFT calculations, charge densities distribute all over the supercells. Thus, it is difficult to associate charges to specific atoms which can useful for understanding electronic interactions. Bader suggests using two steps to determine the charge of atoms [173, 174]. First using the steepest gradient to reach the charge density maximum from grid to grid. Once the maxima are found, the electronic density along the paths to the maximum (m_i) are assigned into the grid points shown in Fig. 3.8(a). After the electronic densities are rearranged into a simple configuration, zero flux surfaces of the charge density surfaces (black-dashed line in Fig. 3.8(b)) determine the charge to assign each ion in the supercell.

Chapter 4

FePt Nanoparticle Growth on $Mg_{(1-x)}Ti_xO$ Substrates

In section 2.1.3, it was discussed how FePt grains deposited on MgO exhibit good (001) texture and large out-of-plane coercivity for HAMR media. Since MgO is insulating, the FePt can only be deposited using radio frequency sputtering, which makes the deposition rate low and limits granular FePt for industrial applications. It has been suggested that doping Ti into rock-salt MgO to make a conductive MgTiO material with rock-salt structure could be a practical solution. The MgTiO underlayer could enhance the deposition rate by allowing for direct circuit sputtering. However, the FePt grains have increased wetting and smaller out-of plane coercivity. In this section, we aim to investigate the morphology change of granular FePt nanostructures on different Mg(Ti)O substrates to provide insight into their effect. Therefore, we study the formation energies of low-index surfaces of $L1_0$ FePt and their termination as well as predict the morphology of free FePt nanoparticles. Next, in order to describe how rock-salt TiO incorporates with rock-salt MgO structure, we calculate the segregation energies with various MgTiO slabs to determine the most stable MgTiO structure. Finally, we calculate the adhesion energies of FePt/Mg(Ti)O systems with different number of TiO layers to predict the morphologies of supported granular FePt.

4.1 Morphology of FePt Nanoparticles

In this section, we use DFT to calculate the fundamental properties of $L1_0$ ordered FePt to access the formation energies regarding its low index surfaces. We use the unit cell (shown in Fig. 4.1) and optimise the structure of $L1_0$ ordered FePt with 9×9×9 MP grids used for BZ sampling. Plane-waves with energies up to 500 eV are used to expand the wave functions for all FePt/MgTiO calculations. Using this approach the calculated lattice parameters for bulk FePt is 3.83 Å which is consistent with the experimental observation [15]. In order to predict the morphology of free FePt nanoparticles, we chose (100), (001), (110), (011) and (111) surfaces to calculate the formation energy using the supercell approach. The supercells are periodic parallel to the surfaces and a 15 Å vacuum gap is used normal to the surface. 9×9×1 MP grids are used for BZ sampling with 1 k point in the direction normal to the surface of slab. We calculate the formation energy as a function of thickness of FePt slabs using Eq. 3.51. The FePt surfaces with (001), (011) and (111) orientations are stoichiometric, and the two opposite surfaces on the slab are symmetrically equivalent. By using the same number of Fe and Pt atoms, the FePt slabs with (001) and (110) orientation are inequivalent indicating the terminations are different for two surfaces (one is Fe terminated, the other is Pt terminated). Therefore, the calculated formation energies of (001) and (110) surfaces are an average over Fe and Pt terminations. Fig. 4.1 shows representative slabs for the five surfaces. The (100), (001), (110), (011) and (111) slab contains 20, 20, 8, 10 and 10 atoms per supercell, respectively. Table 4.1 summarises the converged formation energies and the average magnetisation for the given surfaces. The results are in a good arrangement with recent work using a similar approach [175]. The highest coordinated surface (111) has the most stable formation energy (γ_{111} = 1.834 J/m^2), while the most unstable one is the (100) surface (γ_{100} = 2.196 J/m^2). The magnetisation of Fe and Pt atoms shown in Table 4.1 are an average over the whole slab. The calculation shows the magnetic moments are comparable for these five surfaces and Bader analysis indicates the magnetic moment of Fe atoms at the outermost layer is increased by 4 % with respect to the bulk. Using the Wulff construction (performed using the VESTA code) the predicted equilibrium morphology of the free FePt nanoparticles is a truncated octahedron. The FePt nanoparticles in octahedral shape consist of eight hexagonal (111) facets, two square (100) facets and two square (001) facets (Fig. 4.2).

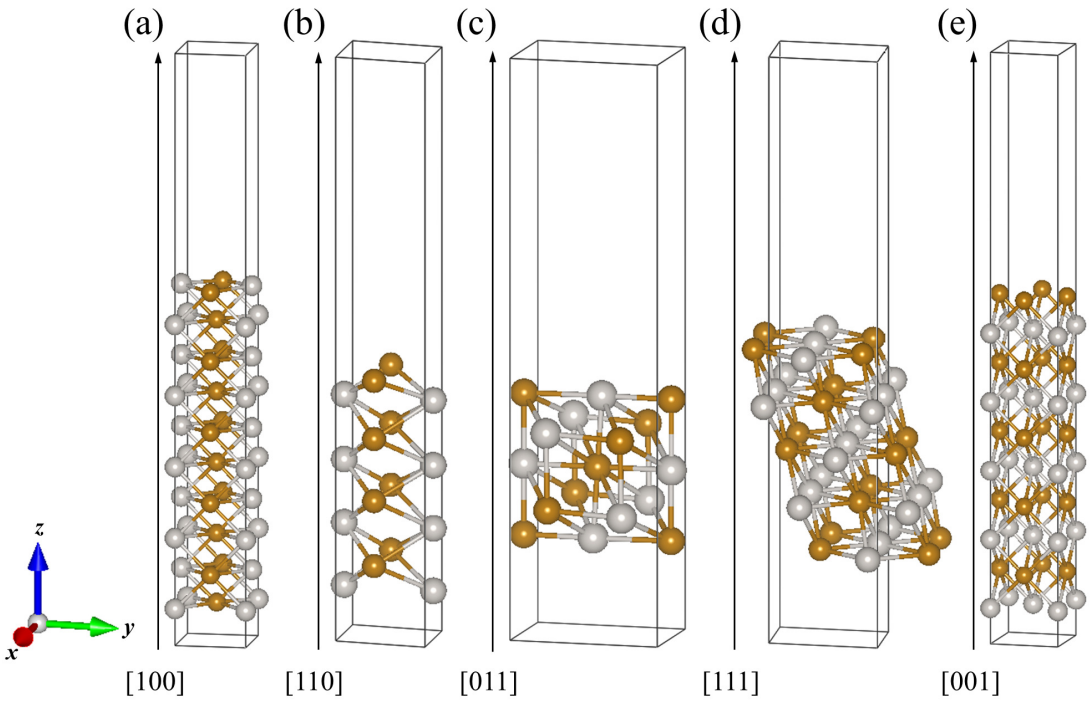

Figure 4.1: Supercells used in the surface calculations of $L1_0$ ordered FePt. The arrows indicate the surface orientation of the low-index surfaces. (a), (b), (c), (d) and (e) are the surfaces of (100), (001), (110), (011) and (111), respectively. The brass and sliver spheres are represented Fe and Pt atoms.

Surface	Formation energy (J/m^2)	Spin moment of Fe (μ_B)	Spin moment of Pt (μ_B)
Bulk	—	3.086	0.339
(100)	2.196	3.135	0.349
(001)	2.195	2.965	0.324
(110)	2.153	3.167	0.381
(011)	2.100	3.195	0.404
(111)	1.834	3.147	0.339

Table 4.1: Surface formation energy and spin moment (SM) for five low-index surfaces of $L1_0$ ordered FePt and bulk FePt. The spin moment of Fe and Pt are the average value over individual species through entire slab. The used supercells are the structures in Fig. 4.1. Therefore, the (100), (011) and (111) surfaces are stoichiometric, (110) and (001) surfaces have Fe and Pt termination at each side.

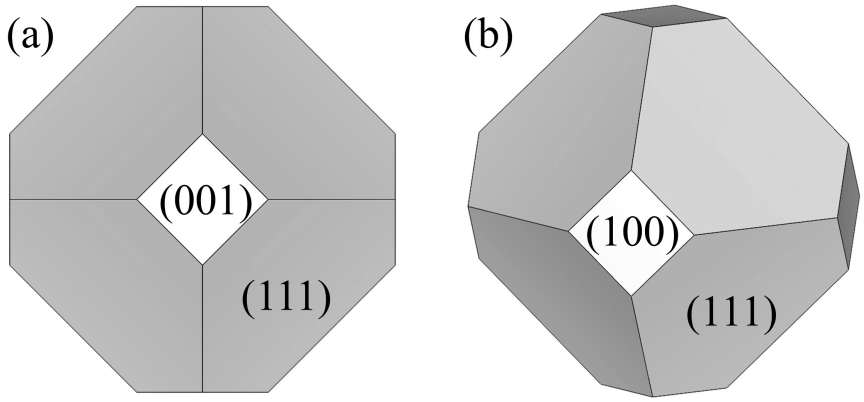

Figure 4.2: The predicted morphology of free FePt nanoparticles is truncated octahedral, which consists of eight (111) surfaces, four (100) surfaces and two (001) surfaces. (a) and (b) is the top and side view of FePt morphology, respectively.

We note that the non-stoichiometric (001) surface appears on the predicted truncated-octahedral nanoparticle. Therefore, it is important to determine the termination of the FePt (001) surface for the following investigation. In order to study the termination of (001) and (110) surfaces, we used the stoichiometric (001) and (110) surfaces to calculate the phase diagram for accessing the stability of Fe and Pt atoms on the surface. The phase diagram is calculated using the formation energy from Eq. 3.51. Fig. 4.3 illustrates the surface formation energy of different termination of non-stoichiometric FePt (001) and (110) surfaces. The surface formation energy is as a function of the Pt chemical potential, the lower and higher boundaries represent the Pt-poor and -rich conditions, respectively. The phase diagram shows that the termination of the FePt (110) surface depends on the chemical potential, the transition of termination happens at $\mu_{\mathrm{Pt}} - \mu_{\mathrm{Pt(bulk)}} = -0.15$ eV. However, the Pt-terminated (001) surface is always more stable than the Fe-terminated (001) surface. Therefore, the thermodynamic stability indicates the (001) truncated surface of FePt nanoparticles should be Pt-terminated.

4.2 Incorporation of TiO into the MgO Substrate

In order to investigate the FePt growth on MgTiO systems, we first need to understand the incorporation of MgO and TiO in the MgTiO substrate. Since the experimental

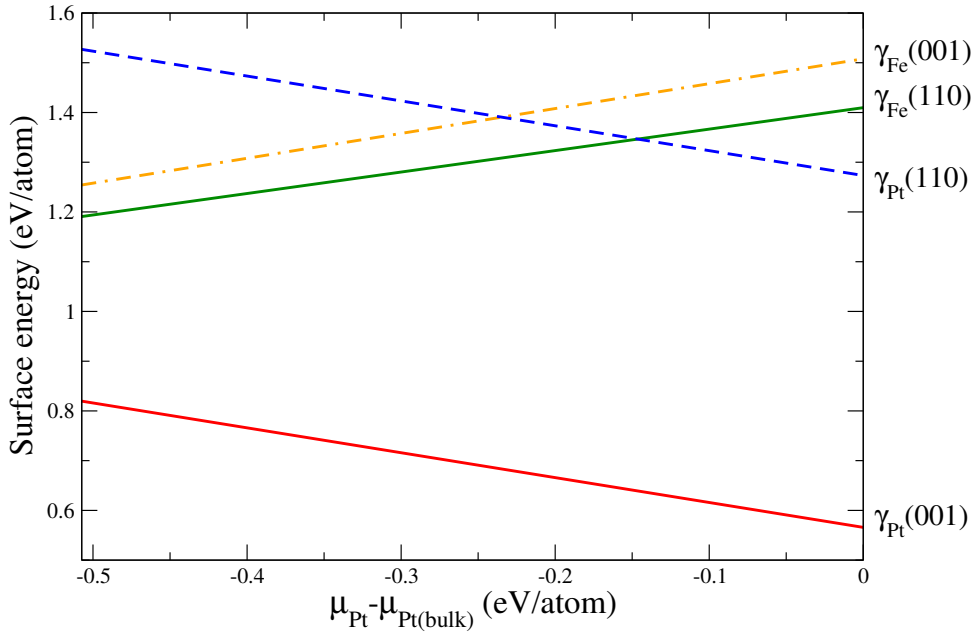

Figure 4.3: Equilibrium surface energy phase diagram of $L1_0$ ordered FePt involving two non-stoichiometric orientations. Each line shows one surface energy for a specific surface (labelling on the right).

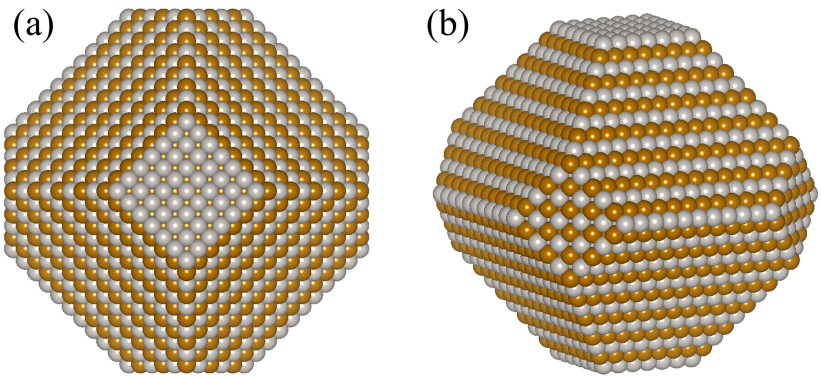

Figure 4.4: Predicted atomic structure of free FePt nanoparticles. Most of the surfaces are stoichiometric. However, the (001) surfaces are Pt terminated due to the relative stability of Pt atoms in the phase diagram (Fig. 4.3). (a) and (b) show different views of the nanoparticles.

observation shows that the MgTiO is a rock-salt structure, we calculate the lattice constant of MgO and TiO in rock-salt structure in advance [38]. We use the primitive unit cell for the optimisation of rock-salt MgO and TiO with 13×13×13 MP grids used for BZ sampling. Using this approach the calculated lattice constants of MgO and TiO are 4.25 and 4.28 Å, respectively. In addition, both of these two structures are non-magnetic. Both TiO and MgTiO slab calculations are performed using the supercell approach with 5×5×1 MP grids for BZ sampling (with 1 k point in the direction perpendicular to the surfaces). In order to understand the stability of pure rock-salt TiO slab with (001) orientation, we optimise the TiO (001) surfaces with various monolayers comparing their formation energy. Fig. 4.5 shows the optimised atomic structures of TiO slabs with different number of TiO monolayers (from 5 to 8 monolayers). All TiO structures show a small ferroelectric distortion normal to the surface. Each atom shows approximately (or less) 0.02 eV energy difference compared to bulk TiO. However, the structural distortions are different between the slabs with even and odd number of TiO monolayers. The distortion of TiO surface with even layers are in one direction, whereas the one with odd layer have two opposite directions and a horizontal structure in the middle of TiO slabs. Therefore we suggest using the following equation to calculate the formation energy,

$$\gamma_{\mathrm{f}} = \frac{E_{\mathrm{tot}} - \sum_i N_i \mu_i + ADt}{2A}, \tag{4.1}$$

where E_{tot} represents the total energy of TiO surface, N_i and μ_i indicate the number of atoms and chemical potential with respect to specific species, A and t represent the area of the supercell and the thickness of the slabs, D is the energy density of distortion due to the ferroelectricity. Fig. 4.6 shows the calculated formation energy of TiO surface as a function of TiO monolayers. The formation energy of surface with even TiO monolayers is 0.70 J/m^2 and the one with odd TiO monolayers is 1.11 J/m^2. The calculation suggests the energy density of ferroelectric distribution is 8.56×10^8 J/m^3. Moreover, the energy density of the boundary formation (odd TiO monolayer) can be related to the formation energy of even and odd layers of TiO,

$$\gamma_{\mathrm{f}}^{\mathrm{even}} + \frac{\Gamma}{2} = \gamma_{\mathrm{f}}^{\mathrm{odd}}, \tag{4.2}$$

where the $E_{\mathrm{f}}^{\mathrm{even}}$ and $E_{\mathrm{f}}^{\mathrm{odd}}$ represent the formation energy of TiO surface with even and odd TiO monolayers and the Γ is the energy density of the boundary formation (horizontal TiO structure in odd layer cases). The calculation suggests the energy density of boundary formation is approximately 0.83 J/m^2. In addition, the representative PDOS (shown in

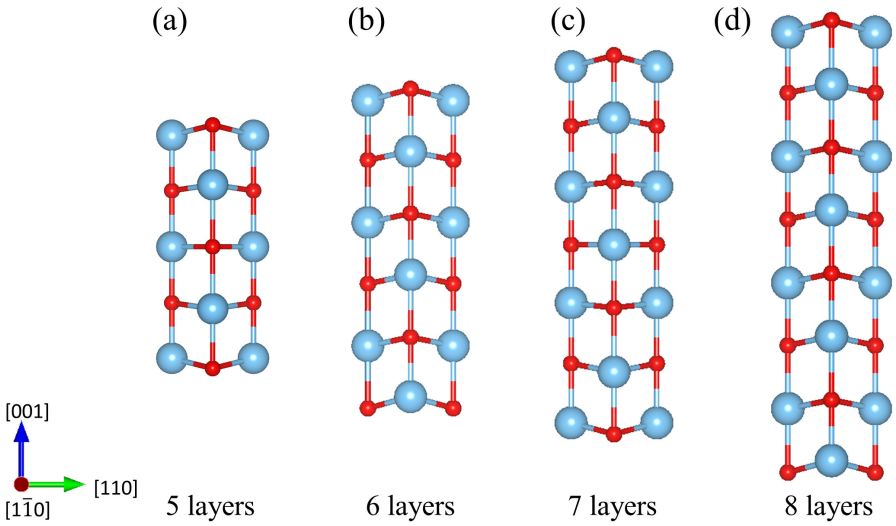

Figure 4.5: Optimised atomic structure of rock-salt TiO in (1$\bar{1}$0) orientation. (a), (b), (c) and (d) are the structures with 5, 6, 7 and 8 TiO monolayers, respectively.

Fig. 4.7.) of two TiO slabs with different number of layers indicates that the rock-salt TiO is metallic and Ti 3d orbitals dominate the valence band around the Fermi level.

Therefore, we consider doping even numbers of TiO layers into the MgTiO substrates due to the stability. In order to predict the stable structure of TiO doped MgO slab, we investigate the slabs involving different configurations of TiO and MgO. The three dimensions of the supercell are used $a = b = 4.25$ Å and $c = 50$ Å, periodic boundary conditions are parallel to the a and b direction and a 15 Å vacuum gap is normal to the surface. Each supercell of different MgTiO configuration consists of ten atomic layers (including TiO and MgO), which means it containing 20 cations (including Mg and Ti atoms) and 20 ions (O atoms) in the supercell. Fig. 4.8 shows three cases of different configurations of MgTiO substrates, each case shows two MgTiO slabs with different arrangements. One is TiO layers dispersed in MgO slab and the other is TiO layers segregated from MgO slab. The segregation energy (ΔE) is defined as,

$$\Delta E = E_{\text{seg}} - E_{\text{dis}}, \tag{4.3}$$

where E_{seg} and E_{dis} represent the total energy of TiO segregates on MgO surface and dispersed in the MgO slab, respectively. The structures in Fig. 4.8 demonstrate the different arrangements of two, four and six substitutional TiO layers in/on MgO slabs (hereafter referred to as MgTi(2)O, MgTi(4)O and MgTi(6)O) and the segregation energies. The

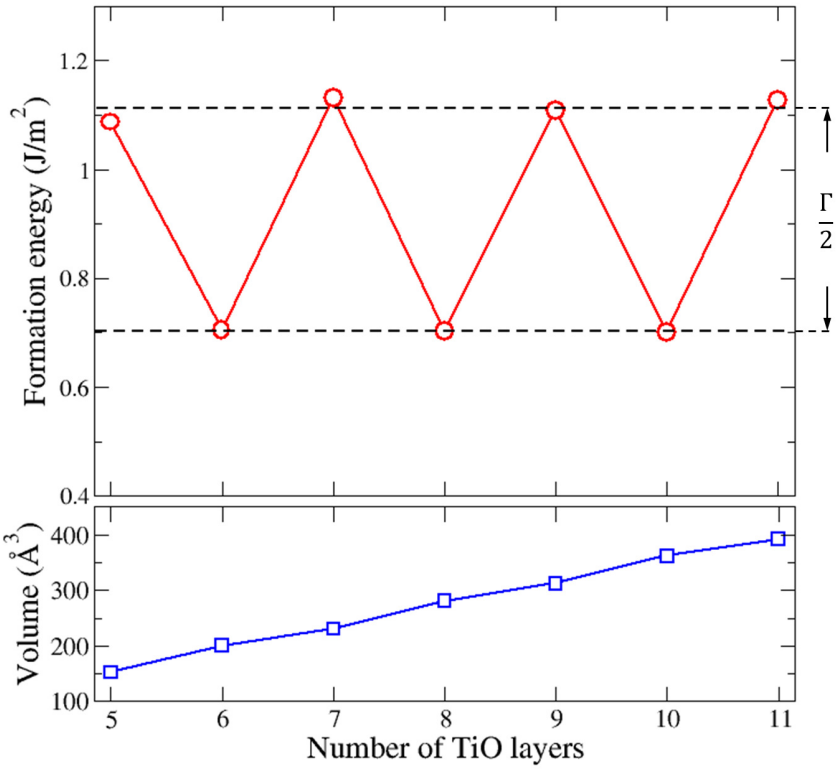

Figure 4.6: (Top) formation energies and (bottom) volume of rock-salt TiO surfaces as a function of number of TiO layers. $\Gamma/2 = 0.42$ J/m^2 represents half of the formation energy of the TiO boundary.

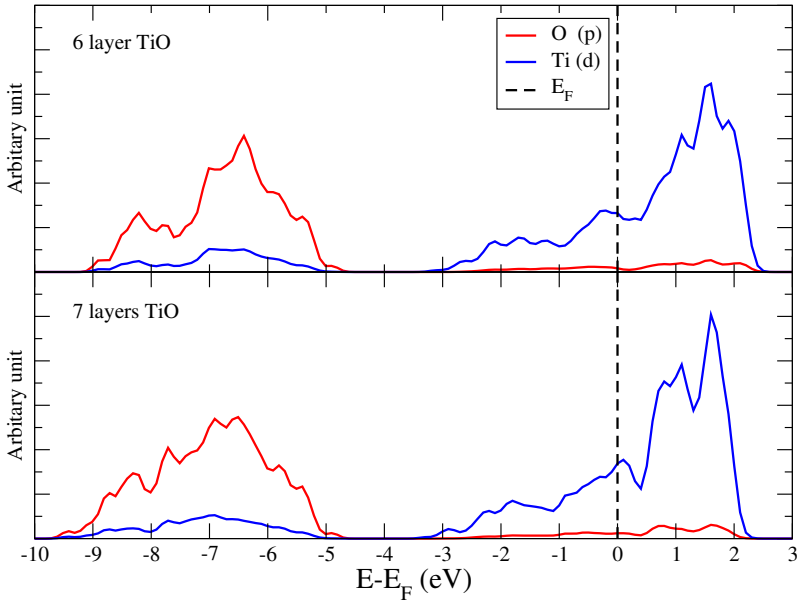

Figure 4.7: Density of states projected on O $2p$ and Ti $3d$ orbitals. The number of TiO layers are labelled in the respective panels.

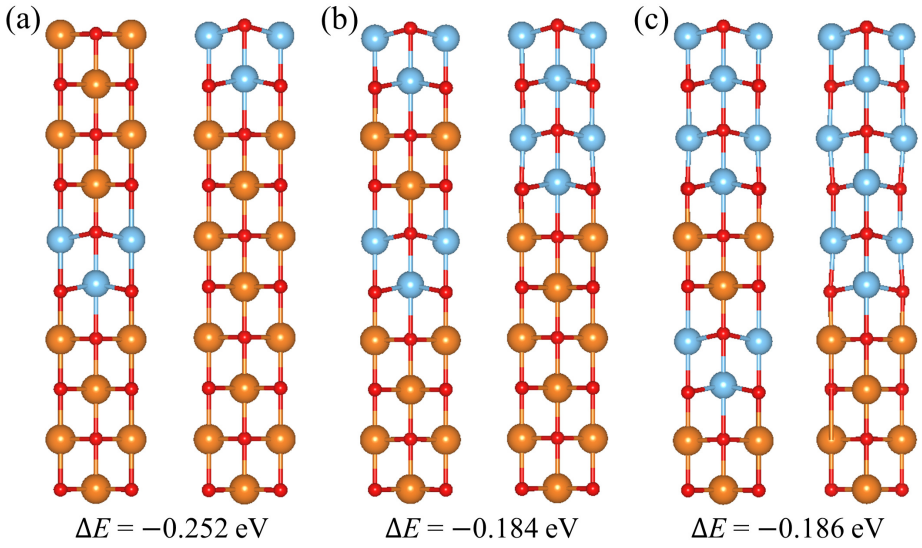

Figure 4.8: Different optimised configurations (in $(1\bar{1}0)$ orientation) of TiO incorporated into MgO slab to assess the preferentially stable configurations of MgTiO structure. (a), (b) and (c) shows the configurations of two, four and six substitutional TiO layer in ten layers MgTiO structure in total. The segregation energy of each case is presented at the bottom. The orange, blue and red spheres represent the Mg and Ti and O atoms, respectively.

calculation shows the segregation energies for two, four and six substitutional TiO layers are -0.252, -0.184 and -0.186 eV, respectively. The negative segregation energies in all cases indicate the substitutional TiO layer prefers to isolate from the MgO. In addition, the small ferroelectric distortion of TiO is found in the MgTiO structure as well. The result shows that the TiO structure should be segregated from the MgO surface to form a more stable MgTiO surface.

4.3 Structure and Adhesion Energy of the FePt/$Mg_{(1-x)}Ti_xO$ Interface

Recent work shows that the geometry of FePt on MgO has Fe atoms directly located above the O atoms for FePt (001) and MgO (001) orientations [35, 176]. Considering the computational cost of calculation, we use $x = y = 4.24$ Å as dimensions of the supercells

of the FePt/MgTiO systems. The used dimensions indicating the MgTiO substrates is fixed without any in-plane strain.

4.3.1 Strained FePt (001) surface

The supercells used for the FePt/MgTiO calculations do not include any lattice dislocations at the interface and so introduces a 10 % in-plane strain on the FePt (001) slab. In order to understand the effect of the 10 % strain on the FePt slab, we optimise the FePt slabs with $x = y = 4.24$ Å (lattice constant of MgO) comparing the spin moment and the vertical displacement. The supercells include ten atomic layers of FePt, the terminations of the top and bottom FePt slab are Pt and Fe atoms, respectively. The choice of non-stoichiometric (001) surface is due to the calculated interface of FePt growth on MgO surface. Table 4.2 summarises the variations of spin moment (ΔSM) of Fe atoms and the vertical displacement of atoms from the centre of the slab. The values are calculated with respect to the fully relaxed FePt (001) slabs ($x = y = 3.83$ Å). ΔMM indicating the strained FePt increases the spin moment by an order of 0.1 μ_B for the surface Fe atoms. In addition, the strained FePt slab reduces the thickness by 3 Å in the [001] direction with respect to relaxed slab.

Atomic layer from centre	ΔMM of Fe atoms (μ_B)	Δl of Fe atoms (%)	Δl of Pt atoms (%)
2 (top)	0.23	-20.27	-18.57
1	0.15	-19.00	-18.26
0	0.06	0.00	0.00
-1	0.02	-17.20	-16.47
-2 (bottom)	0.16	-15.12	-15.08

Table 4.2: Variations of spin moment of Fe atoms from FePt supercell with respect to the relaxed FePt structure. The vertical displacement of the atomic position of constrained FePt slab in terms of relaxed FePt. The reference for the calculated displacements are the central Fe and Pt atoms, which are in the fifth and sixth layer (from bottom to top) for Fe and Pt, respectively.

4.3.2 Adhesion energies of the FePt/MgTiO

In order to predict the morphologies of FePt on various MgTiO substrates, we optimise the structure of $L1_0$ ordered FePt on various Mg(Ti)O substrate and assess their adhesion energy using Eq. 3.56. We use the same dimensions of MgTiO suprecells but extend the supercell size normal to the surface accommodating ten atomic layers of FePt (001) structure. According to the investigation discussed in section 4.1, we suggest the termination of FePt (001) surface to the vacuum is Pt termination, while the termination of FePt to the interfaces is Fe atoms. The supercells contain 10 Fe and 10 Pt atoms as well as 40 atoms of MgTiO. We use the same MP grids for BZ sampling as section 4.2. The FePt layers experience a 10 % in-plane lattice mismatch with respect to the MgO (001) surface. We consider FePt on MgTiO substrate with substitutional TiO layers, the six different substrates contain MgO, MgTi(2)O, MgTi(4)O, MgTi(6)O, MgTi(8)O and TiO substrate. Fig. 4.9 shows the optimised structures of FePt/Mg(Ti)O systems and the vertical distance between Fe and cation (either Mg or Ti atom) at the interface. The vertical distance is decreased from 2.06 Å (FePt/MgO) to 1.65 Å (FePt/TiO) with increase of TiO content. Fig. 4.10 demonstrates the trend of the adhesion energy with various TiO layers. The adhesion energy is as a function of vertical distance. The adhesion energy is -1.3 J/m^2 when FePt grows on MgO substrates, whereas it decreases to -2.4 J/m^2 with increased TiO concentration. The inset indicates that the reduced vertical distance is responsible for a decrease of the adhesion energy.

The results show that the Fe-Ti bond formation strengthens the adhesion energy and reduces the distance between FePt and MgTiO substrates. In order to provide deeper insight into the interaction of FePt/Mg(Ti)O, we perform Bader analysis calculating the charge associated with each atom in the interface. The charge transfers (Δq) are calculated using Bader charge for atomic layer relative to the isolated FePt and Mg(Ti)O slabs. The calculation indicates there is only a small amount of charge transfer through the interface. Fig. 4.11 shows the charge transfer with respect to the specific Fe layer, Pt layer and Mg(Ti)O slabs (labelled in Fig. 4.11). The charge transfer varies with the number of TiO layers and it is negligible for the MgO substrate. The charge transfer of the Fe layer is appreciable for only two TiO layer doped in MgO slab and reaches -0.4 e as a minimal value for the MgTi(4)O substrate. The majority of the additional charge of Fe layer comes

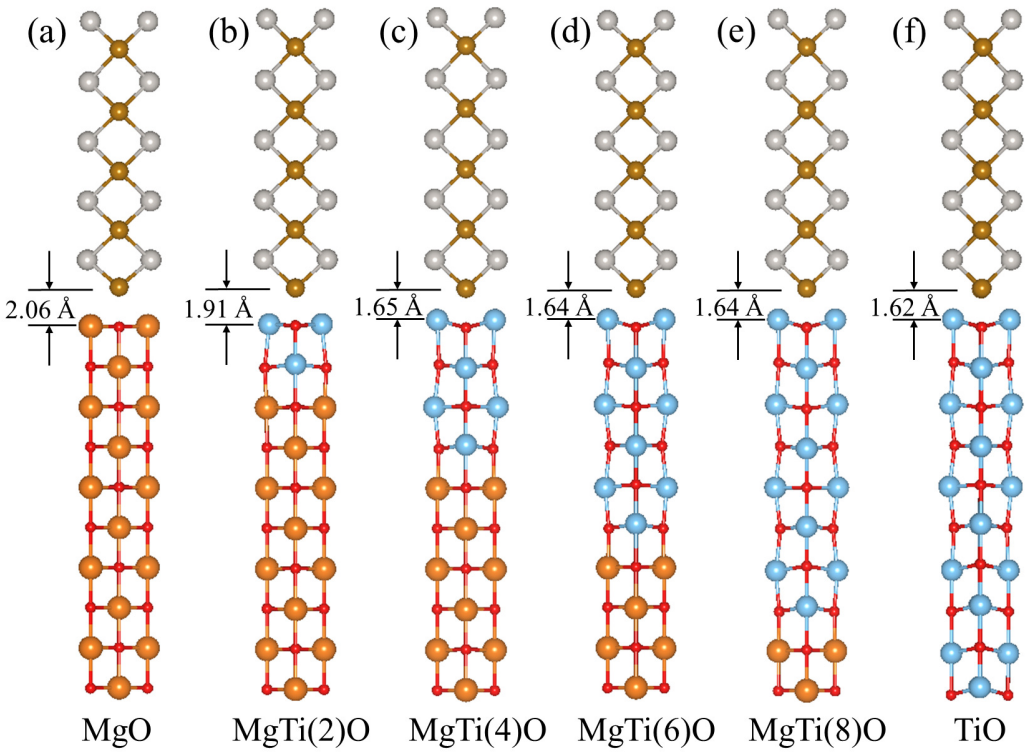

Figure 4.9: Optimised atomic structures of FePt/MgTiO with vertical distance between the FePt and MgTiO slabs are shown in (110) orientation. The distances are from the bottom Fe atom to the adjacent cation (Mg or Ti). (a), (b), (c), (d), (e) and (f) are the system with FePt attached on MgO, MgTi(2)O, MgTi(4)O, MgTi(6)O, MgTi(8)O and TiO substrate, respectively.

from the MgTiO slabs and small contribution from the adjacent Pt layer. The average spin moment of the Fe layer decreases as a function of number of TiO layers from 3.4 to 2.95 μ_B. The reduction of the spin moment is due to the charge transfer form MgTiO and the Pt layer to the Fe 3*d*-orbital offsetting the spin moment. The charge and spin moment of other Fe atoms away form the interface are not significantly influenced. The negatively charged Fe atoms and the positive charged MgTiO slabs increase the ionicity of the Fe-Ti bond and shorten the distance between the FePt and the substrates. We examine the projected density of state (PDOS) for the interfacial Fe atoms. Fig. 4.12 shows that the projected density of state associated with the 3*d* orbitals on the interfacial Fe atoms with various MgTiO substrates, the number in each panel represents the number of substitutional TiO layers. The black, red and blue solid lines represent the PDOS of Fe 3*d* orbital of bare FePt slab, FePt growth on MgO substrate and FePt deposited on

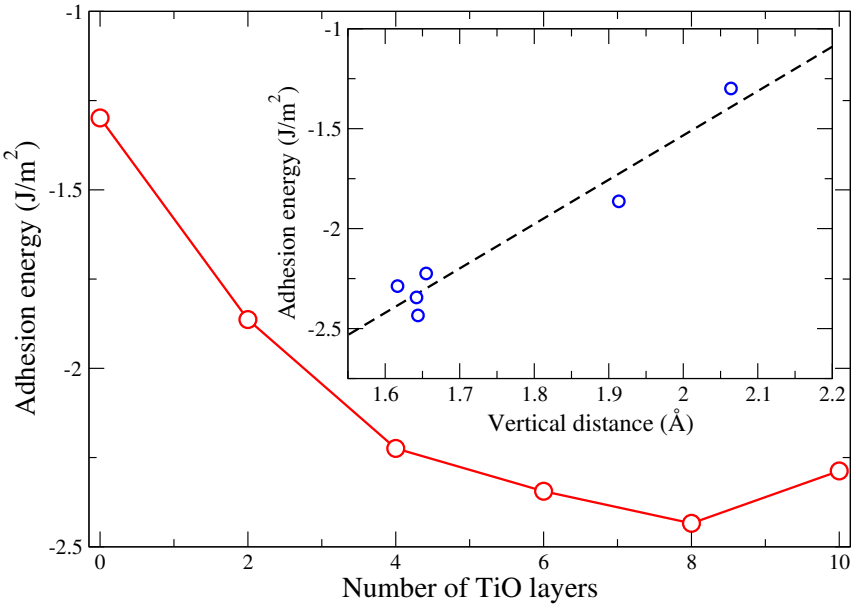

Figure 4.10: Variation of adhesion energy of FePt and MgTiO slabs with the number of TiO layer segregated from the MgO substrate (red line). The inset shows the positive correlation between the adhesion energy and vertical distance. The dashed line is a guide to the eye.

MgTiO substrate, respectively. The green solid line is the PDOS on 3*d* orbital of two topmost TiO layers. Fig. 4.12(a) indicates the electronic structure of the interfacial Fe atoms only show minor perturbation before and after attaching on MgO substrate. As the number of doped TiO layers increases up to 4 layers, a new electronic state in spin down channel appears growing between -1.0 and -2.5 eV in the PDOS of interfacial Fe atoms. The new state increases the population of the spin down channel reducing the spin moment of Fe atoms at the interface, which is consistent with observation in Fig. 4.11. Moreover, the new introduced electronic state of Fe atoms contributes to the same state with the TiO 3*d* channel shown in Fig. 4.12(f) indicating the bond formation between Fe and Ti atoms.

4.4 Morphologies of Supported FePt Nanoparticles

Using the adhesion energies from section 4.3, we predict the equilibrium morphology of FePt nanoparticles on various Mg(Ti)O substrates using Wulff-Kaishew construction. Fig.

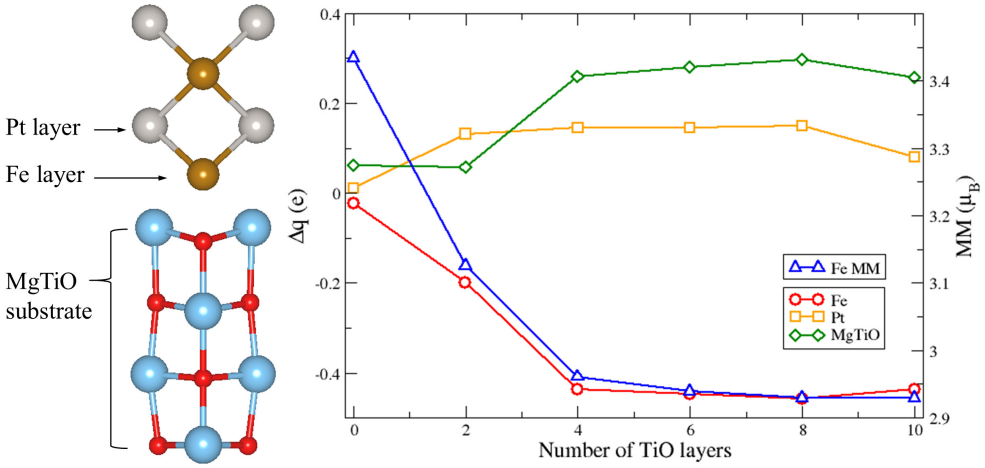

Figure 4.11: (Left) An interfacial atomic sketch of FePt/MgTiO indicates the specified Fe and Pt layers, the MgTiO here represent the entire substrate. (right) Variation of the charge transfers with number of TiO layers associated with the specific Fe, Pt and MgTiO layers. The spin moment of interfacial Fe atom demonstrates as a function of TiO layers (right scale).

4.13 shows the predicted nanoparticles and atomic models for supported FePt nanoparticles. The predicted morphology of the FePt nanoparticle is a height-reduced truncated-octahedron in [001] direction. Fig. 4.13(a) represents the FePt grain growth on single crystalline MgO substrate and Fig. 4.13(b) demonstrates the FePt deposits on MgTi(x)O ($x \geq 4$) substrates. The former morphology has large contact angle (θ_l) between FePt (111) and MgO (001) surfaces, whereas the latter one shows a small contact angle (θ_s) between FePt (111) and MgO (001) surfaces. The morphology of granular FePt on Mg(Ti)O (especially the number of TiO layers ≥ 4) substrate further reduce the height of granular FePt nanoparticles due to the stronger adhesion energy. The stronger Fe-Ti bond formation hinders the growth of granular FePt increasing the wetting between FePt and MgTiO substrate.

4.4.1 Passivation of the Fe-Ti bond formation

In the previous section, the calculated adhesion energy indicates the Fe-Ti bond formation strengthens the interaction between FePt and MgTiO substrates. Therefore, the doped

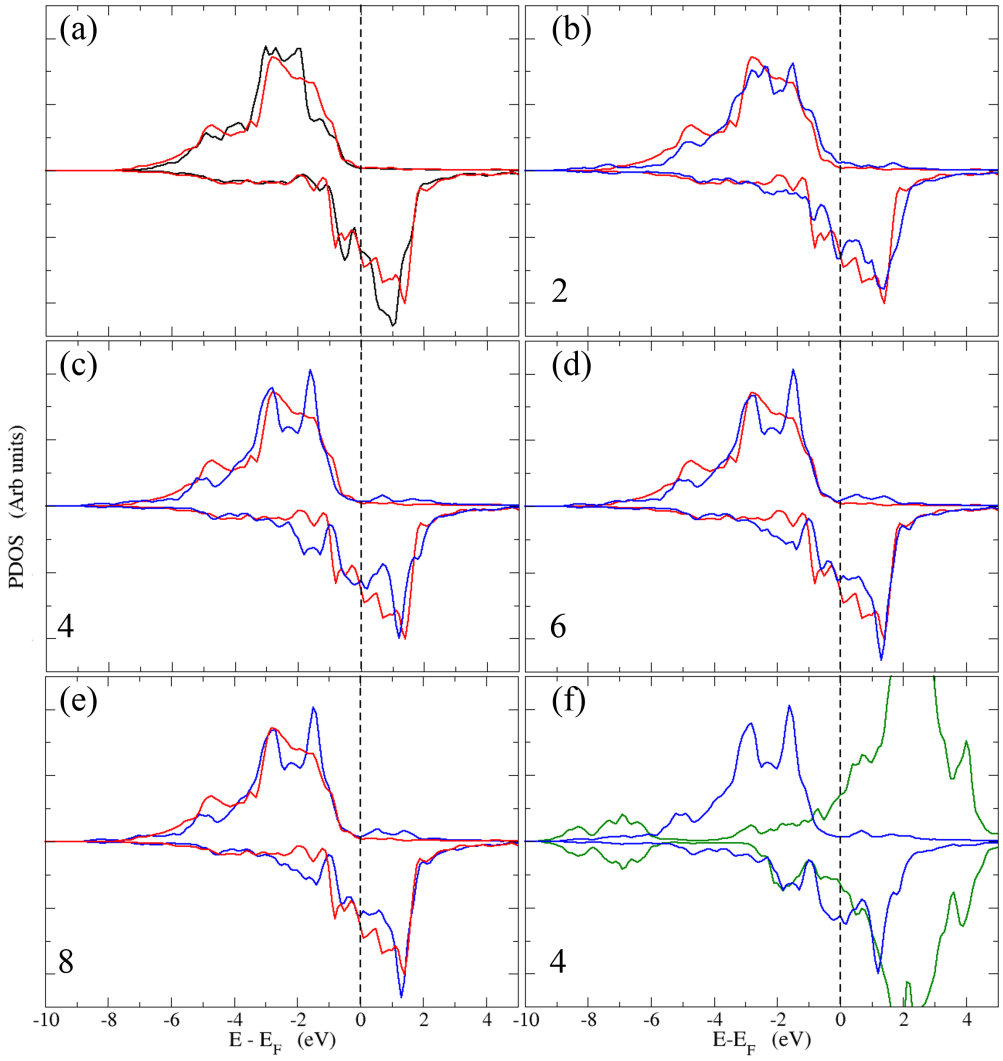

Figure 4.12: The projected density of states (PDOS) with respect to the 3d orbitals for interfacial Fe atoms and TiO layers. (a) The PDOS of interfacial Fe atoms of bare FePt slab (black line) and FePt growth on MgO substrate (red line). (b)-(e) The PDOS of interfacial Fe atoms of FePt growth on Mg(Ti)O substrates (blue lines), the number in the panels represent the number of TiO layers. (f) The PDOS of two topmost TiO layers in MgTi(4)O substrate (green line).

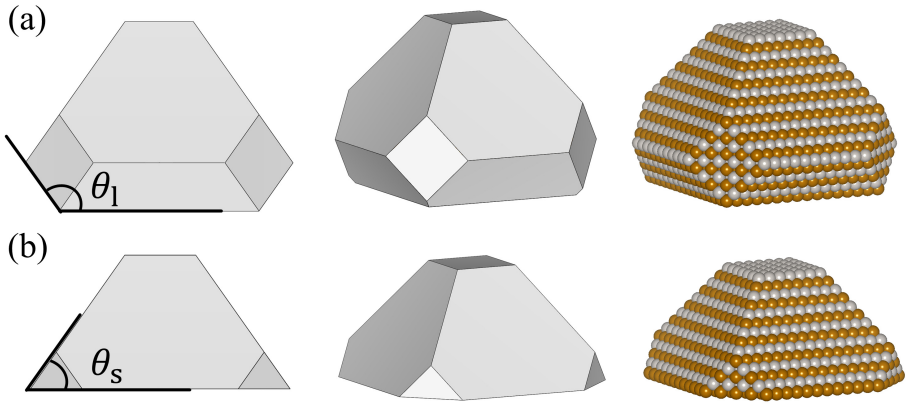

Figure 4.13: (Left two)The predicted morphology and (right) atomic model of supported FePt nanoparticle on different substrate. The shape of the supported nanoparticle is a height-reduced t-Oh in [001] direction. $(00\bar{1})$ surface of the nanoparticle is Fe termination. (a) and (b) represent the growth of FePt nanoparticle on MgO and MgO with more than four layers of TiO on the top, respectively.

TiO layers cause a disadvantage (increased wetting of the FePt grains) offsetting the benefit of using DC sputtering [38]. One strategy to overcome the disadvantage is to introduce an intermediate layer passivating the Fe-Ti bond formation but keeping the conductivity of the underlayer. Therefore, we consider several MgO layers as the intermediate material between FePt and TiO to restore the adhesion energy. We use the same supercell of the previous FePt/Mg(Ti)O calculations, but the Mg(Ti)O slab is replace by the Ti(Mg)O slab. Which means there are substitutional MgO layers at the top of TiO substrate. The optimised FePt/TiMg(x)O (x = 2 and 3) structures are shown in Fig. 4.14. The adhesion energy -1.74 J/m^2 indicates two MgO layers cannot completely block the Fe-Ti bond formation. With the increased substitutional MgO layer up to three, the adhesion energy and vertical distance are -1.30 J/m^2 and 2.05 Å, respectively. Thus, the calculation suggests depositing several thin layers of MgO can hinder the enhanced adhesion between FePt grains and MgTiO substrates for producing good HAMR media.

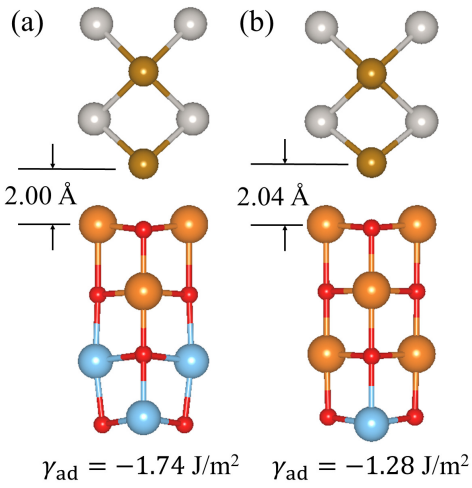

Figure 4.14: The optimised structure of FePt/TiO system with (a) two and (b) three additional MgO monolayers on the top of TiO substrate. The vertical distances and adhesion energies indicate three monolayers of MgO coating incorporated on TiO substrate is similar to that for pure MgO substrate ($l = 2.06$ Å and $\gamma = -1.30$ J/m^2).

4.5 Discussion and Conclusions

There are several factors can influence the accuracy of the result in this chapter. In the adhesion energy calculation, there is a 10 % strain at the interface between FePt (001) and MgO (001) surface. In reality, the strain energy may be relieved by the formation of lattice dislocations at the interface eliminating the strain of the FePt slabs. Considering a supercell 100 times larger than the present one may allow the dislocation at the interface to be modelled. But it is computational prohibitive at the density functional theory level. Although we present the result without dislocations, the interaction between Fe and Ti atoms at the interface does decrease the adhesion and increase the wetting of granular FePt on MgTiO substrate, consistent with the experimental observation. Although the lattice constant of bulk MgTiO must differ from that of bulk MgO, the difference of calculated lattice constants between rock-salt MgO and TiO is less than 1 %. Therefore, the use of lattice parameter of MgO should not significantly influence the results of stabilities of MgTiO slabs as well as the adhesion energies. The PBE functional is well-known to underestimate the band gap for many oxides, but the total energies for calculating the formation energies and the adhesion energies should be accurate to predict the morphology for free and supported FePt nanoparticles.

In the study of MgTiO, we demonstrate several cases of different configurations of TiO layers in MgO substrate to compare the stability. The systematic investigation predicts that TiO should segregate from the MgO surface, which can be observed using electron energy loss spectroscopy mapping within a scanning transmission electron microscope (STEM) [177]. We also predict the significant displacement (0.4 Å) of the FePt to interfacial Ti associated with the content of TiO, the property could be experimentally observed using STEM as well. Finally, the prediction of passivating the Ti-Fe bond formation using additional intermediate MgO layers indicates the MgO thin layer may decreases the wetting of granular FePt nanoparticle and restore the coercivity of FePt nanoparticles.

In this investigation, we focus an granular FePt grain growth on Mg(Ti)O substrates and use the surface energies predicting the morphology of FePt nanoparticles. However, there are alternative substrates as the underlayer for sputtered FePt in HAMR media investigation mentioned in section 2.1, such as TiN [27, 178], TiON [27] and FeCoNi [179]. Ti is a common element involved in these underlayers, which suggests the drawback from Fe-Ti bond formation also dominates the out-of plane coercivity and the wetting of FePt nanoparticle of those HAMR system. The amorphous carbon and SiO_2 are the segregation material used to decouple the FePt grains and reduce the diameter of the grain parallel to the surface in FePt HMAR media. Although the additional segregation significantly influences the diameter of the FePt grain from 20 nm downward to 6 nm, experimental observations show that both materials are insoluble into the FePt/Mg(Ti)O system. Therefore, that suggests the segregations make little influence for the predicted FePt morphology. One of the most important properties of FePt as HAMR media is the magnetic anisotropy energy (MAE). Especially the growth of FePt on modified substrate should exhibit good out-of plane coercivity for stable information recording. Although Fig. 4.11 reveals the decrease of magnetic moment of interfacial Fe atoms, it is not sufficient evidence to explain the reduced MAE. The MAE calculations can be performed using non-collinear calculations, but it is beyond the scope of this work.

In summary, we perform first-principles calculations to investigate the adhesion energy between FePt and Mg(Ti)O substrates. The calculation shows that substitutional TiO layers preferentially segregate to the surface of MgO. Fe-Ti bond formation decreases the adhesion energy from 1.29 to 2.35 J/m^2 between FePt and Mg(Ti)O slabs due to the charge transfer. The vertical distance between FePt and Mg(Ti)O reduces from 2.07 to

1.65 Å with the incorporation of TiO into MgO. By using the Wulff construction, the predicted morphology of free nanoparticle is truncated-octahedral involving (100), (001) and (111) facets. The predicted equilibrium shape (using Wulff-Kaishew construction) of the supported FePt nanoparticles are a height-reduced truncated-octahedron within [001] direction. The nanoparticle with stronger wetting for TiO doped substrate shows a small contact angle relative to the FePt (111) facets. The predicted FePt shapes are in good agreement with experimental cross-sectional transmission electron microscopy images [38]. The original purpose of the doped TiO into MgO is for the conductivity. However, the Fe-Ti bond formation hinders the growth of FePt grains on the substrate and the magnetic property. Thus, we suggest to deposit ultrathin layers of single-crystalline MgO on the Mg(Ti)O underlayer to passivate the interaction.

Chapter 5

Ti and TiPt Nanoparticle Oxidation

5.1 Interaction Between Ti Nanoparticles and Oxygen Atoms

In order to understand the reactivity between metallic nanoparticles and oxygen we consider two example systems of fundamental and technological relevance. We study the most energetically stable configurations of a Ti nanoparticle with various oxygen configurations on the surface. We further investigate the energy barriers to the diffusion of an oxygen atom from the surface to the sub-surface to assess the mobility of oxygen atoms. We also study the atomic arrangement of a TiPt binary nanoparticle for different oxygen molecule concentrations on the surface and subsurface.

We consider a 181-atom Ti nanoparticle with decahedral morphology for the investigation of oxidation. The reasons for selecting this morphology and size is as follows. First, decahedral nanoparticles are experimentally observed in this size range due to their relatively small strain energy relative to the icosahedral shape [180–182]. Second, it is necessary to use a large-enough nanoparticle to capture the complex interplay between oxygen atom adsorption and Ti nanoparticle properties. Considering a Ti nanoparticle with 181 atoms in decahedral morphology (hereafter Dh_{181}) is computationally feasible

and offers sufficient adsorption sites for investigation. The length between any two adjacent vertices of the optimised Dh_{181} is approximately 14 Å and the calculated formation energy of the Dh_{181} with respect to bulk Ti is 0.81 eV per atom.

5.1.1 Oxygen adsorption on the Ti(0001) surface

In order to provide insight into the interaction between oxygen atoms and the Ti nanoparticle, we first consider the simpler case of oxygen adsorbing on the α-Ti (0001) surface, since it only provides two inequivalent three-fold hollow adsorption sites (hcp and fcc sites) on the surface. The supercell used to model single oxygen adsorption on Ti surface consists of 200 Ti atoms (eight monolayers along the c-axis) with the dimensions $x = y = 17.6$ Å and $z = 3$ Å. A 5×5×1 MP grid is used for BZ sampling in these calculations. The difference between the hcp and fcc sites is the number of second nearest-neighbour Ti atoms in the subsurface. The former site contains one Ti atom just below the adsorption site, whereas the latter site has three Ti atom in the subsurface but not directly below the adsorption site. The adsorption energies of oxygen atom adsorbing on the Ti (0001) surface are -5.72 and -6.09 eV for hcp and fcc sites, respectively. To analyse the difference between oxygen adsorption on hcp and fcc sites, we calculate the strain energy with respect to oxygen adsorption. The strain energies for an oxygen adsorbing on hcp and fcc sites are 0.32 and 0.13 eV per system, respectively. However, the 0.19 eV energy difference in geometric strain can only partly explain the 0.37 eV energy difference in adsorption energy.

To provide further insight, we use Bader analysis to calculate the electrostatic energy for the adsorbed oxygen atoms. For both adsorption sites, the oxygen atoms acquire some charge transferred from the surrounding Ti atoms. Table 5.1 summarises the charge of the first and second nearest-neighbour Ti around the oxygen atom. Both oxygen atoms have three first nearest-neighbour Ti with positive charge. The number of the negatively charged second nearest-neighbour Ti on the surface is the same for two adsorption sites. However, oxygen adsorbing on fcc site provides two more second nearest-neighbour Ti in the subsurface. The estimated electrostatic energies for hcp and fcc oxygen adsorption sites are -0.33 and -0.56 eV, hence the difference of electrostatic energy is 0.23 eV. The two energy differences (strain and electrostatic energies) together fully explain the stability of the oxygen adsorptions on two inequivalent sites.

Index	Atom	Layer	hcp site		fcc site	
			distance (Å)	charge (e)	distance (Å)	charge (e)
1	Oxygen	surface	0.00	-1.16	0.00	-1.11
2	Ti-1st	surface	1.96	0.39	1.95	0.41
3	Ti-1st	surface	1.97	0.39	1.94	0.41
4	Ti-1st	surface	1.97	0.35	1.95	0.41
5	Ti-2nd	surface	3.62	-0.12	3.63	-0.12
6	Ti-2nd	surface	3.63	-0.11	3.63	-0.12
7	Ti-2nd	surface	3.62	-0.11	3.63	-0.14
8	Ti-2nd	subsurface	3.34	0.20	3.66	0.03
9	Ti-2nd	subsurface	—	—	3.66	0.10
10	Ti-2nd	subsurface	—	—	3.66	0.13

Table 5.1: The distance between an adsorbed O atom and nearest-neighbour Ti atoms and the net charge on the respective Ti atoms. 1st and 2nd represent the first and second nearest-neighbour, respectively.

5.1.2 Oxygen on the surface and subsurface of the nanoparticle

The Dh_{181} nanoparticle presents 15 inequivalent three-fold hollow sites on the surface (including hcp and fcc sites) shown in Fig. 5.1(a). We optimise the structure for an oxygen atom on each of these adsorption sites and calculate the adsorption energies (E_{ads}). Table 5.2 summarises the adsorption energies and corresponding strain energies for the 15 inequivalent sites on the nanoparticle surface. Site 7 has the most energetically stable configuration for a single oxygen adsorption with $E_{\text{ads}} = -5.96$ eV per oxygen atom. In addition, this configuration also has the smallest strain energy (0.11 eV). An oxygen atom adsorbing on site 1 presents the most energetically unstable configuration with $E_{\text{ads}} = -5.46$ eV per oxygen atom as well as a 0.16 eV strain energy. The more stable configuration corresponds to the smaller strain energy which is similar to the case of single oxygen on Ti(0001) surface, but the complex geometries of the strained configurations lead to a less clear trend for oxygen adsorption on the nanoparticle.

Apart from the oxygen adsorption on the surface of nanoparticle, we also calculate the adsorption energy for oxygen atoms in the subsurface to evaluate the stability for different

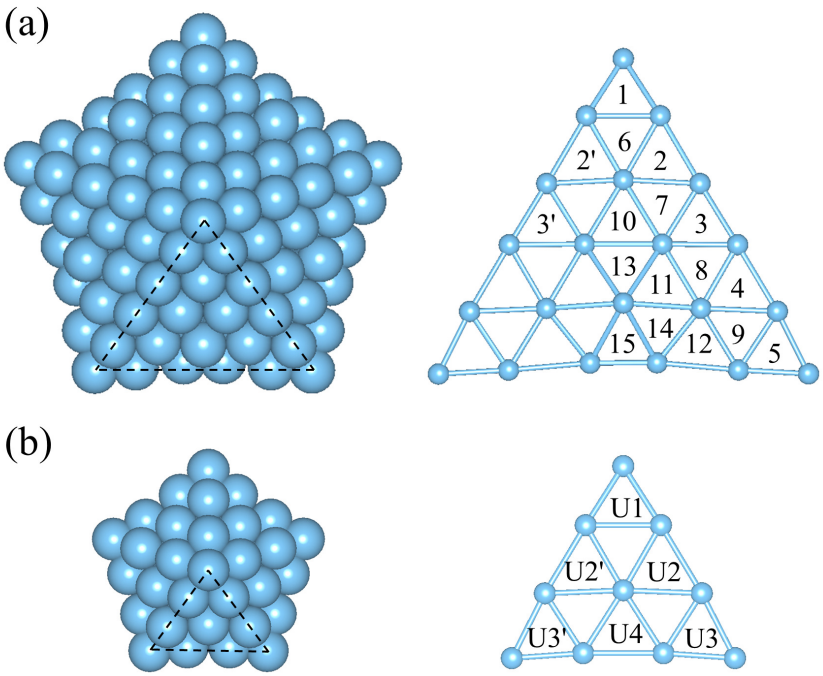

Figure 5.1: Illustration on the left shows the top view of (a) surface and (b) subsurface of the Dh_{181} nanoparticle. The figures on the right represent the partial enlargements of the surface and subsurface facets (see dashed triangles). The labels on the hollow sites indicate the inequivalent adsorption sites from 1 to 15 (surface) and U1 to U4 (subsurface). The adsorption sites with prime are equivalent by mirror symmetry used in the following section.

configurations. The calculation indicates the oxygen atoms prefer to incorporate into the octahedral (oct) interstitial sites of nanoparticles as shown in Fig. 5.1(b) (labeled U1 to U4). Table 5.3 summarises the adsorption energies and strain energies for the subsurface adsorption sites. Site U1 shows the most stable adsorption energy (-5.82 eV) with the smallest strain energy (0.13 eV), while site U4 has the least stable adsorption energy (-5.38 eV) and the largest strain energy (0.36 eV). The adsorption energies show a positive correlation with strain energy. As the adsorption energies in Tables 5.2 and 5.3, the most stable configuration is still oxygen atom on site 7. Which is 0.14 eV stable than site U1 in the subsurface. These results indicate oxygen atoms preferentially adsorb on the surface instead of penetrating into the nanoparticle. These calculations demonstrate that strain energy plays an important role for oxygen adsorption on the surface and subsurface of the nanoparticle, which shows good agreement with recent work investigating the interaction between oxygen atoms and PtCu core/shell nanoparticles [183]. Although we calculate the

Index	Site	E_{ads} (eV)	E_{strain} (eV)	Index	Site	E_{ads} (eV)	E_{strain} (eV)
1	hcp	-5.47	0.16	9	fcc	-5.68	0.22
2	hcp	-5.86	0.19	10	hcp	-5.65	0.37
3	hcp	-5.81	0.15	11	hcp	-5.83	0.17
4	hcp	-5.76	0.18	12	hcp	-5.65	0.27
5	hcp	-5.76	0.17	13	fcc	-5.89	0.18
6	fcc	-5.65	0.21	14	fcc	-5.51	0.24
7	fcc	-5.96	0.11	15	hcp	-5.49	0.35
8	fcc	-5.67	0.26	—	—	—	—

Table 5.2: Adsorption energy and strain energy for single oxygen atoms on the surface and sub-surface layers of the $Dh_{181}Ti$ nanoparticle (see Fig. 5.1 for definition of adsorption sites).

Index	Site	E_{ads} (eV)	E_{strain} (eV)
U1	oct	-5.82	0.13
U2	oct	-5.55	0.22
U3	oct	-5.62	0.21
U4	oct	-5.38	0.36

Table 5.3: Adsorption energy and strain energy for single oxygen atoms in the sub-surface layers of the $Dh_{181}Ti$ nanoparticle (see Fig. 5.1 for definition of adsorption sites).

electrostatic energy for oxygen atom on the nanoparticle, the strained structures make the definition of nearest-neighbour difficult. Therefore, it is hard to summarise any correlation between adsorption and electrostatic energies in the nanoparticle calculations.

5.2 Configurations of Adsorbed Oxygen on the Ti Nanoparticle

In order to investigate the increasing oxygen coverage on the surface of the nanoparticle, we arrange pairs of oxygen atoms adsorbing on the surface of the nanoparticle to assess the stabilities of different configurations. The most energetically stable configurations are then

Index	E_{ads} (eV)	E_{strain} (eV)	Index	E_{ads} (eV)	E_{strain} (eV)
S1	-5.77	0.50	S6	-5.80	0.62
S2	-6.00	0.34	S7	-5.84	0.43
S3	-5.85	0.43	S8	-5.96	0.55
S4	-5.81	0.46	S9	-5.80	0.51
S5	-5.90	0.44	—	—	—

Table 5.4: Adsorption energies and strain energies for a single pair of oxygen atoms adsorbing on the surface of Dh_{181} Ti nanoparticle. The corresponding configurations are in Fig. 5.3.

used to construct models for higher oxygen coverages on the surface of the nanoparticle.

5.2.1 One pair of oxygen atoms on the nanoparticle

An oxygen atom adsorbing on site 7 of the nanoparticle is the most stable configuration, thus, it should be the starting point for adsorption one pair of oxygen atoms on the same facet. There are many adsorption sites of two oxygen atoms on the surface of nanoparticle even if one oxygen is fixed on site 7. However, the calculations show that O_{ads}-Ti-O_{ads} configurations are the most stable (where the two adsorbed oxygen atoms share one Ti atom on the surface of the nanoparticle). Fig. 5.2 shows nine most energetically stable configurations of two oxygen atoms adsorption based on the site 7. Table 5.4 summarises the adsorption energies and the respective strain energies for 9 different configurations. Configuration S2 has the most stable adsorption energy ($E_{\text{ads}} = -6.00$ eV/atom) with the smallest strain energy ($E_{\text{strain}} = 0.34$ eV). Besides the strain effect, we calculate the distance between two oxygen atoms (O-O distance) as a function of adsorption energies to determine the stability for respective configurations. Fig. 5.3 shows the configuration with longer O-O distance has more stable adsorption energy indicating the stability of oxygen adsorption should take into account the repulsion between oxygen atoms.

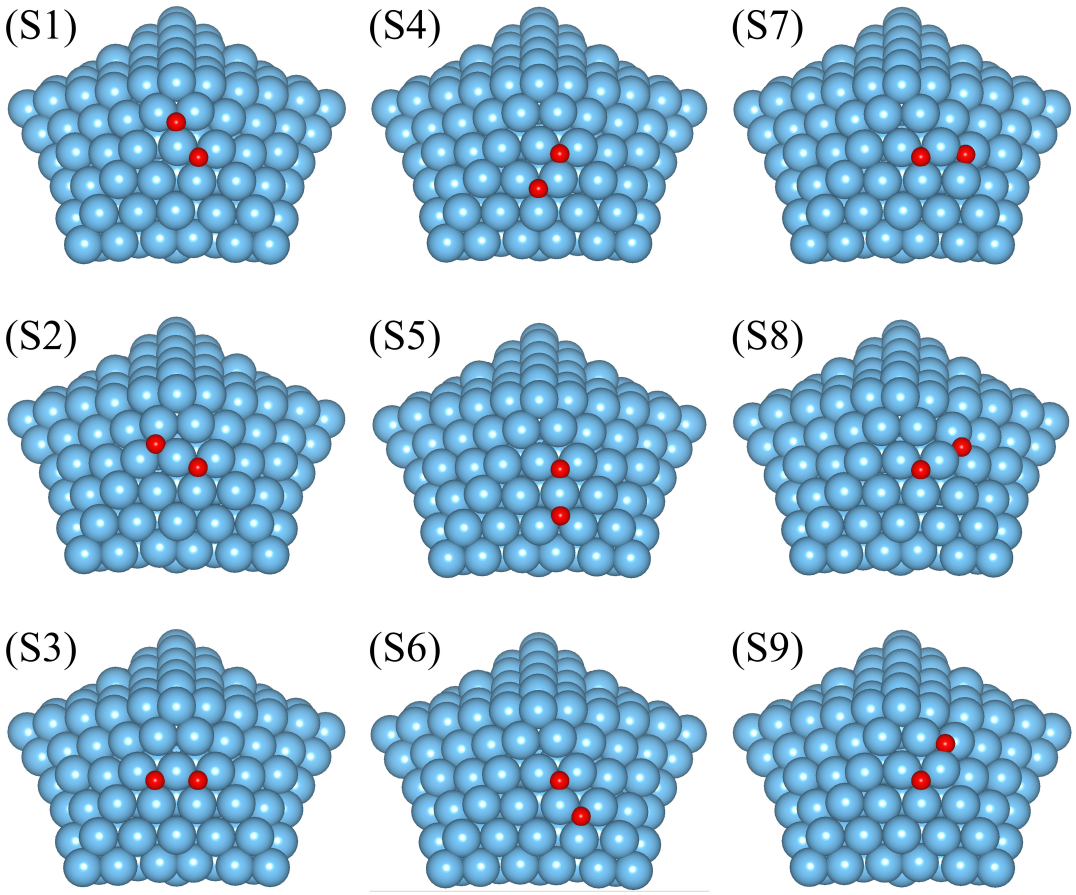

Figure 5.2: Nine optimised configurations of a single pair of oxygen atoms on the Dh_{181} surface. The O_{ads}-Ti-O_{ads} bond formation minimises the adsorption energies. The S2 configuration is the most stable structure in these calculations.

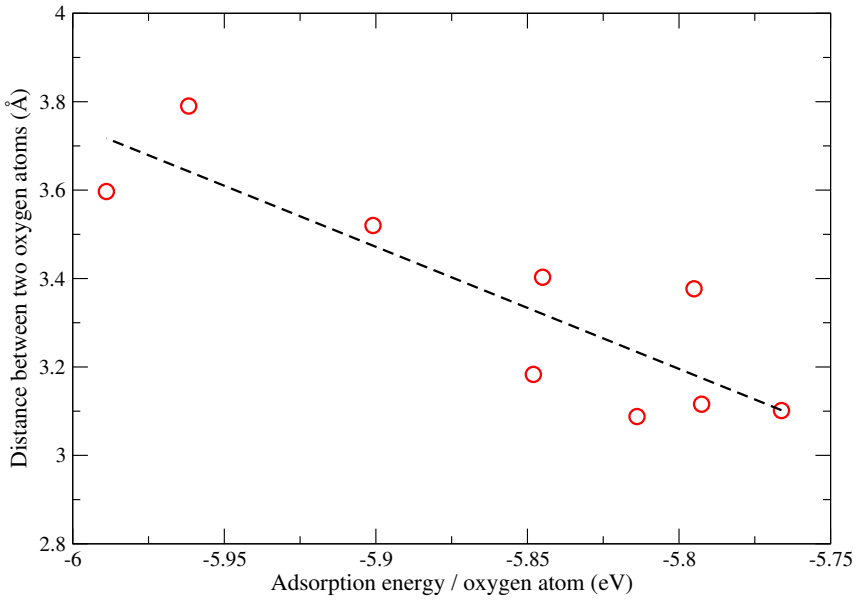

Figure 5.3: Variation of the interatomic distance between two adsorbed oxygen atoms with adsorption energy. The black-dashed line is a guide to the eye.

5.2.2 Two pairs of oxygen atoms on the nanoparticle

Fig. 5.4 demonstrates twelve optimised configurations of double pairs of oxygen atoms adsorbing on the same facet of the nanoparticle. The systematic investigation is based on the most stable single pair of oxygen atoms (configuration S2). Table 5.5 summarises the adsorption energies and strain energies corresponding to those configurations in Fig. 5.4. Configuration D1 maximises the number of O_{ads}-Ti-O_{ads} structures, hence it has the most stable adsorption energy per oxygen atom ($E_{ads} = -6.01$ eV) and the configuration possesses the smallest strain energy as well ($E_{strain} = 0.61$ eV).

5.2.3 Three pairs of oxygen atoms on the nanoparticle

Fig. 5.5 shows ten different configurations of triple pairs of oxygen atoms adsorbing on same facet of the nanoparticle. Table 5.6 summarises the adsorption energies and strain energies for the respective configurations in Fig. 5.5. Configuration T9 presents the most energetically stable structure with $E_{ads} = 6.02$ eV and the smallest strain energy ($E_{strain} = 0.73$ eV). In addition, configurations T2, T8 and T10 also demonstrate similar adsorption energies. However, their larger strain energy decreases the stability of oxygen

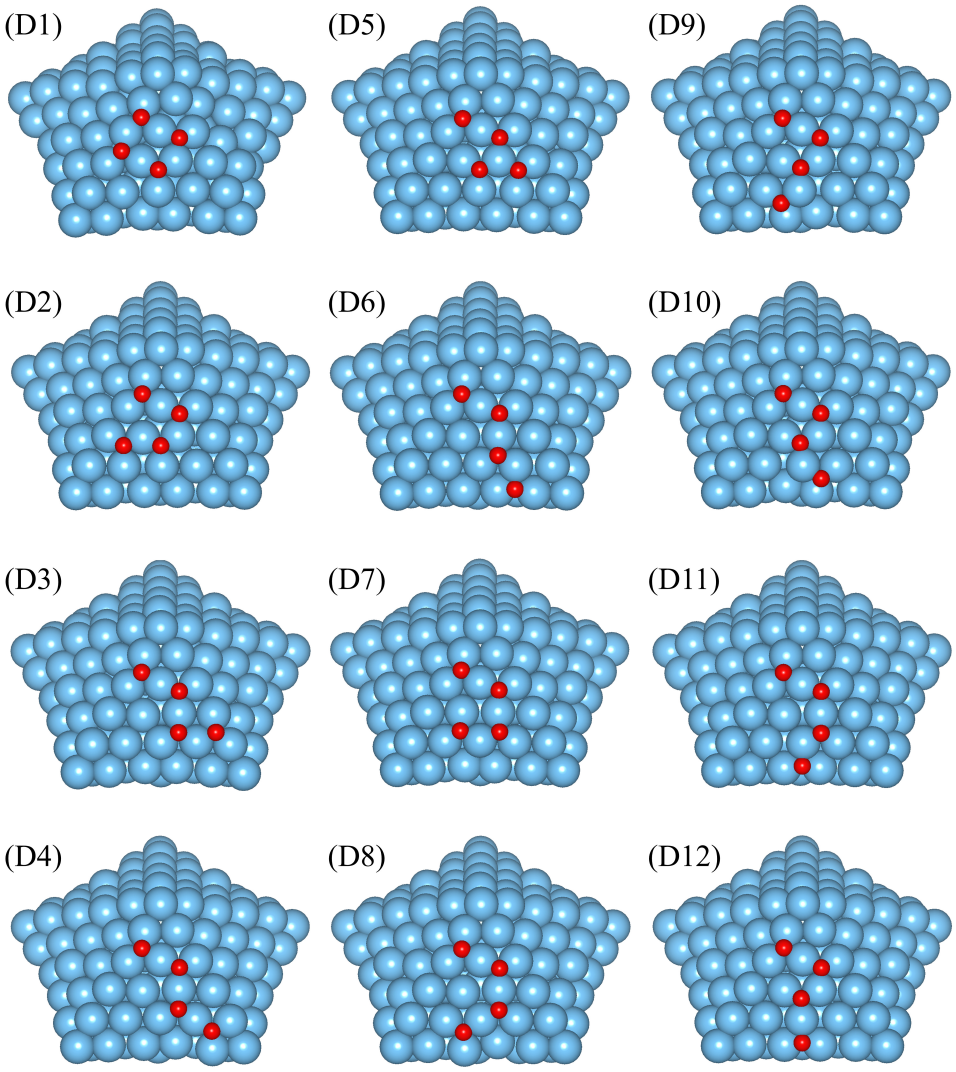

Figure 5.4: Twelve optimised configurations of double pairs of oxygen atoms on the same facet of the Dh_{181}. The D1 configuration is the most stable structure in these calculations.

Index	E_{ads} (eV)	E_{strain} (eV)	Index	E_{ads} (eV)	E_{strain} (eV)
D1	-6.01	0.61	D7	-5.89	0.87
D2	-5.86	1.07	D8	-5.94	1.129
D3	-5.87	0.80	D9	-5.81	0.86
D4	-5.88	1.07	D10	-5.83	0.73
D5	-5.89	1.10	D11	-5.84	1.07
D6	-5.87	1.01	D12	-5.85	1.13

Table 5.5: Adsorption energies and strain energies for double pairs of oxygen atoms adsorbing on the surface of Dh_{181} Ti nanoparticle. The corresponding configurations are in Fig. 5.4.

Index	E_{ads} (eV)	E_{strain} (eV)	Index	E_{ads} (eV)	E_{strain} (eV)
T1	-5.80	1.67	T6	-5.85	1.30
T2	-5.97	1.19	T7	-5.86	1.58
T3	-5.94	0.94	T8	-5.95	1.15
T4	-5.93	1.01	T9	-6.02	0.73
T5	-5.85	1.80	T10	-5.94	1.46

Table 5.6: Adsorption energies and strain energies for triple pairs of oxygen atoms adsorbing on the surface of Dh_{181} Ti nanoparticle. The corresponding configurations are in Fig. 5.5.

adsorption.

The above systematic investigation reveals that the most stable adsorption energies of single, double, and triple pairs of oxygen atoms are approximately 6.00 eV per oxygen atom. The stable configurations invariably constitute linear O_{ads}-Ti-O_{ads} structures and are also accompanied by small strain energy. The stability of two oxygen atoms sharing one Ti atom is a result of maximising the O_{ads}-O_{ads} distance. However, as the oxygen coverage increases, it is impossible to accommodate further linear O_{ads}-Ti-O_{ads} structures on the surface of the nanoparticle. Therefore, some of the adsorbed oxygen transfers into configurations where three oxygen atoms share a Ti atom. This transformation makes more adsorption sites available on the surface and also prevents oxygen atoms occupying the adjacent hcp and fcc site simultaneously.

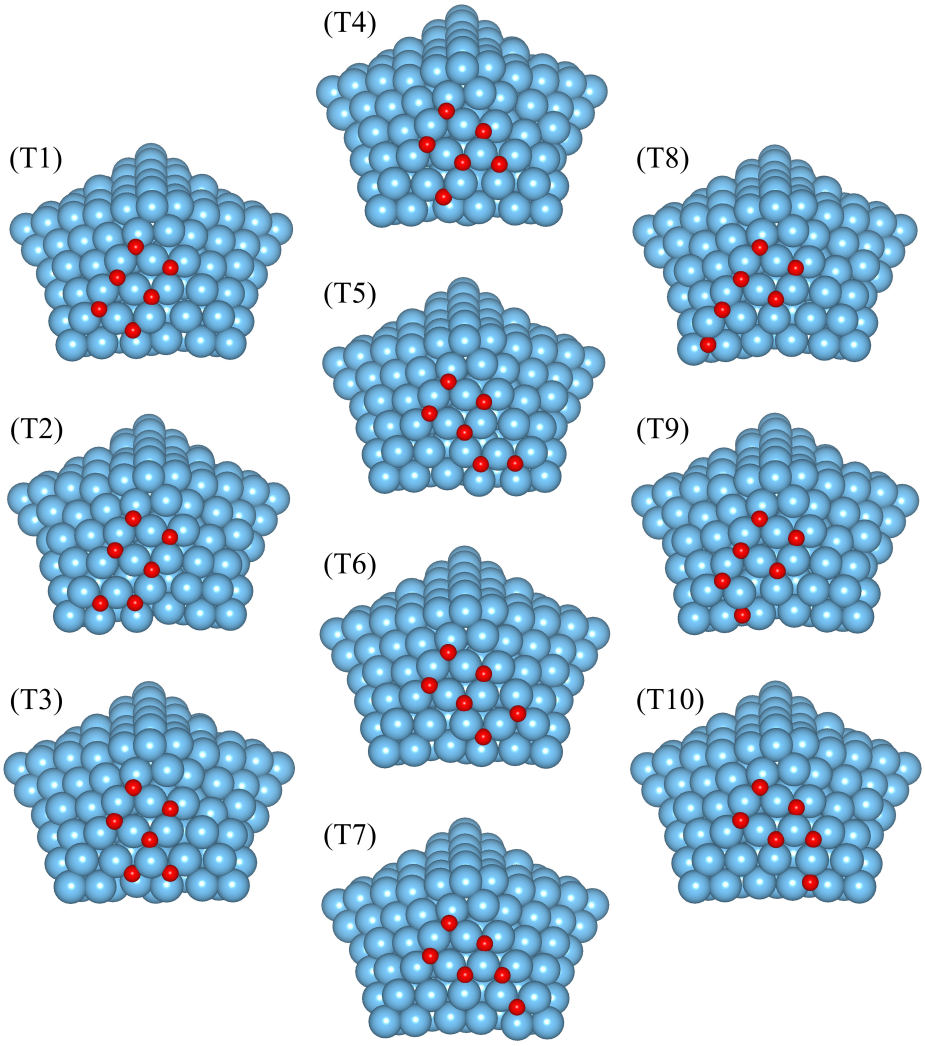

Figure 5.5: Ten optimised configurations of triple pairs of oxygen atoms on the same facet of the Dh_{181}. The T2 configuration is the most stable structure in these calculations.

5.2.4 Various oxygen coverages on the surface of the Dh_{181} nanoparticle

To understand the geometry and the stability of the oxidised Dh_{181} nanoparticle with increasing oxygen coverage, we calculate the total energies of different configurations of oxidised nanoparticle with various coverages. 20, 40, 60, 80, 100 and 150 oxygen atoms adsorbing on the surface of the nanoparticle are considered. For each coverage, we calculate 4, 11, 8, 4, 5 and 1 different oxygen configuration(s). In these calculation, the oxygen atoms are equally distributed on every facet of the nanoparticle, for example, each facet has 2 oxygen atoms for the calculation of 20 oxygen coverage. For the number of oxygen atoms, the calculations always employ an even number of adsorbed oxygen atoms corresponding to the adsorption and dissociation of an integer number of oxygen molecules [184]. Fig. 5.6 (figures on the left) demonstrate the most favourable structures of oxidised nanoparticles with 20 to 150 adsorbed oxygen atoms on the surface. The most stable configurations with 20 to 150 oxygen atoms adsorbing on the nanoparticle surface are denoted as C20 to C150. The point group symmetries for C20 to C80, C100, and C150 are C_{5h}, D_5, and D_{5h}, respectively [185]. The average oxygen adsorption energies of C20, C40, C60, C80, C100, and C150 are 5.79, 5.84, 5.88, 5.81, 5.75, and 5.48 eV per oxygen atom. The most stable adsorption energy is observed at C60 configuration since the configuration maximises the number of linear O_{ads}-Ti-O_{ads} structures on the surface. Table 5.7 summarises the calculated average Ti-Ti bond length on the surface and the average Ti-O bond length.

The surface Ti-Ti bond length is increased as a function of oxygen coverage, whereas the Ti-O bond length is maintained at 1.95 Å for all coverages. In order to assess the surface distortion with respect to variation of oxygen coverage, the surface strain of each oxidised nanoparticle is calculated relative to the pure Dh_{181} nanoparticle. The result indicates that some Ti-Ti bonds on the surface are expanded and others are contracted in C20, C40, C60 and C80 configurations. However, almost all surface Ti-Ti bond lengths are dilated by oxygen adsorption in C100 and C150 configurations. The average strain of the surface Ti-Ti bonds for C20 to C150 are 2.0, 2.5, 3.7, 5.6, 6.5, and 8.2 %, which are shown in Fig. 5.6 (figures on the right).

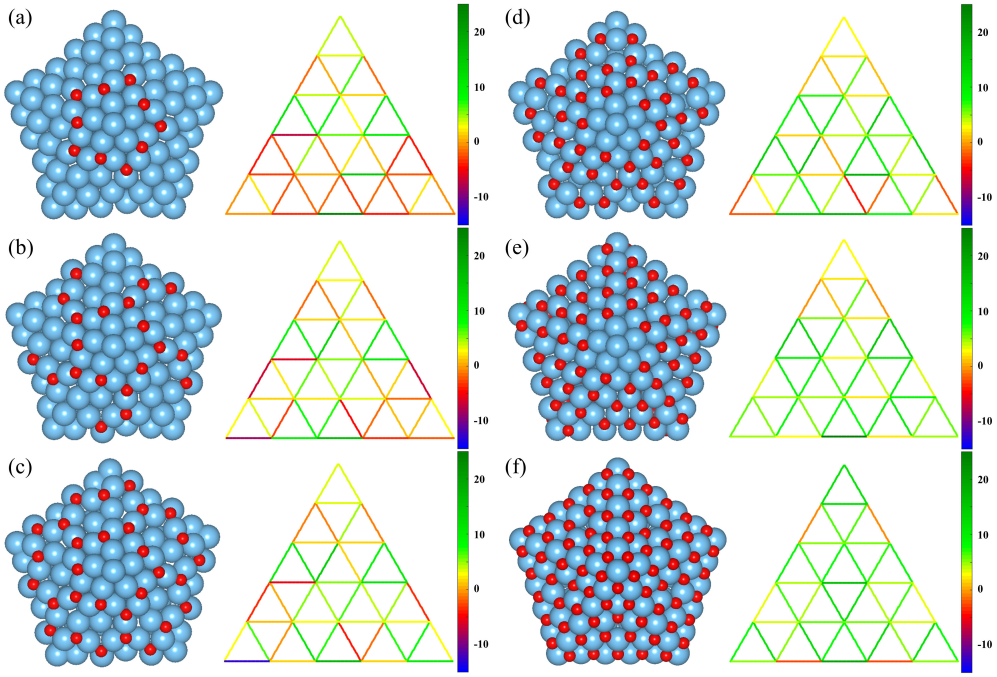

Figure 5.6: Structures (figures on the left) and surface strain (figures on the right) of (a) C20, (b) C40, (c) C60, (d) C80, (e) C100, and (f) C150 nanoparticle structures. The triangular grids are the Ti-Ti bonds on the surface, and the color of the bonds represent the value of the strain relative to the pristine Ti nanoparticle.

Coverage	Bare NP	C20	C40	C60	C80	C100	C150
Ti-Ti bond length (Å)	2.84	2.87	2.89	2.90	2.93	2.94	3.03
Ti-O bond length (Å)	—	1.95	1.95	1.95	1.95	1.95	1.95

Table 5.7: Surface Ti-Ti bond length and Ti-O bond length for the oxidised Ti nanoparticle with different oxygen coverages.

5.3 Oxygen Diffusion on the Ti Nanoparticle

For the further oxidation of Ti nanoparticles, there are two possible scenarios. One is the surface Ti atom diffuses outward through the oxide shell forming an inner void in the nanoparticle [186]. The other is that oxygen atoms on the surface penetrate inside the nanoparticle then incorporate at the octahedral interstitial sites in the subsurface. To certify the feasibility of the two penetrations, we systematically examine many diffusion pathways with either a Ti atom or an O atom each time. For the former situation, one surface Ti is relocated to one of the outermost adsorption sites of oxygen atoms (including three-fold hollow, bridge and top sites). However, the relocated configurations are always found to be less stable than the original one. Therefore, the result suggests Ti atoms do not have a strong trend for diffusion outside the oxide shell. Next, we consider displacement of a surface oxygen atom to an octahedral interstitial site and calculate the total energy change for each oxygen coverages. The result demonstrates the oxygen atoms do not favourably penetrate into the pure Dh_{181} nanoparticle, C20, C40 or C60 configurations. However, the C80 and C100 structures provide a number of more energetically stable structures with one oxygen atom incorporated into the subsurface of the nanoparticle. We do not discuss the oxygen diffusion pathways for the C150 structure, since displacement of an oxygen into the subsurface region results in several surface oxygen ions incorporating into subsurface sites after optimisation. The situation makes it difficult to identify energy barriers for individual oxygen atom diffusion processes. However, this observation suggests that the high-coverage C150 structure is quite unstable, and the penetration of oxygen atoms into the subsurface layer is promoted.

In order to assess the possibility of oxygen penetration into the nanoparticle, we calculate the energy barriers of many possible diffusion pathways for the C80 and C100 configurations. In these calculations, the oxygen atoms are always relocated into the octahedral interstitial sites which are adjacent to the original adsorption sites. Fig. 5.7 demonstrates the possible diffusion pathways and the corresponding energy barriers. With reference to Fig. 5.1 for the definition of the adsorption sites, the C80 structure has the following pathways: (A) 8 $\rightarrow$ U3 and (B) 13 $\rightarrow$ U4. Pathways for the C100 structure are (A) 8 $\rightarrow$ U3, (B) 13 $\rightarrow$ U4, (C) $2' \rightarrow$ U$2'$, and (D) $3' \rightarrow$ U$3'$. The path-A and -B are the direct diffusion pathway, while path-C and -D are indirect ones. The smallest energy barrier (in

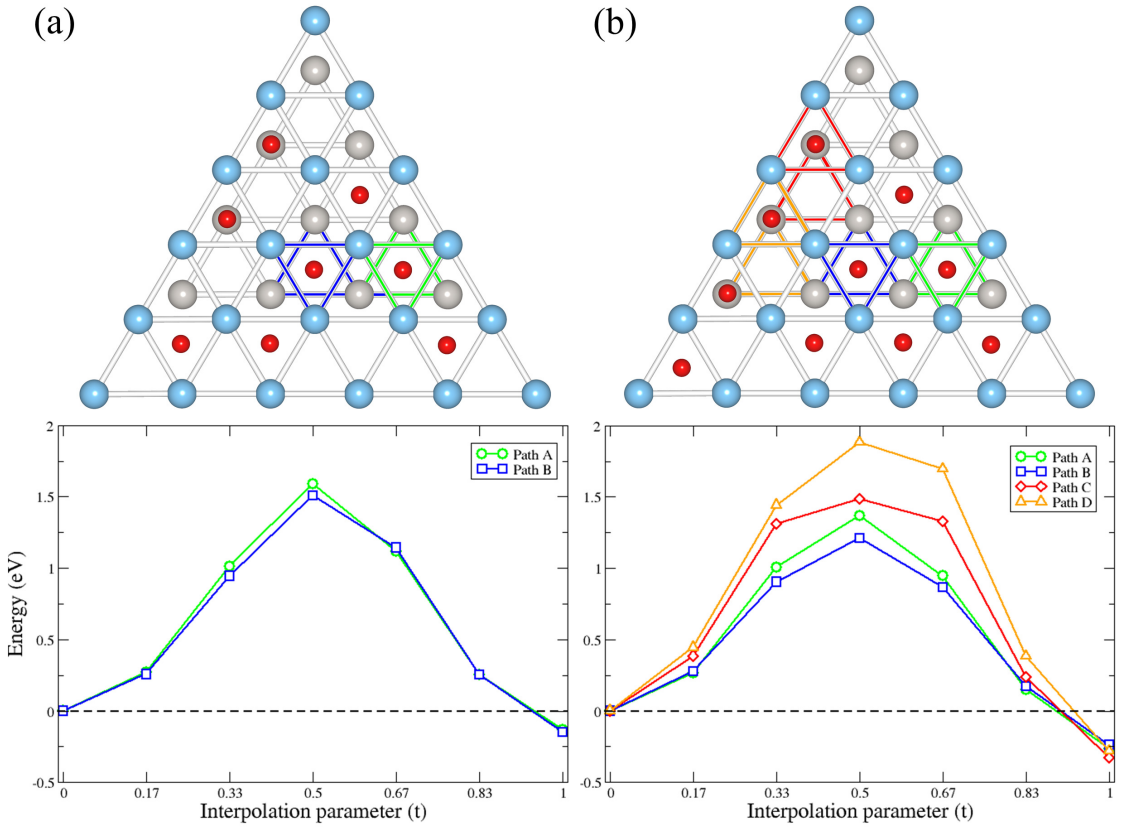

Figure 5.7: Oxygen atom diffusion pathways (top panels) and the respective energy barriers (bottom panels) on (a) C80 and (b) C100 configuration. Surface and subsurface Ti atoms are represented as blue and grey spheres and oxygen atoms as red spheres. The coloured triangles indicate the start- and end-points for the diffusion pathways (A to D)

Fig. 5.7) to oxygen diffusion for the C80 and C100 configurations are 1.50 and 1.21 eV, respectively. In both cases the oxygen atom preferentially penetrates into the nanoparticle in the middle of the facets. The result also implies the barrier of direct diffusion is lower than the indirect pathway.

The results presented above illustrate that increasing oxygen coverage decreases the energy barrier for oxygen diffusion from the surface to the subsurface. Fig. 5.6 also indicates the surface strain is gradually expanded with the increased oxygen coverage. To assess a relation between surface strain and energy barrier, we additionally calculate the energy barriers for C20, C40 and C60 configurations with one oxygen atom penetrated into the centre of the facet. However, there are no oxygen atoms adsorbed on site 13 for the C20, C40 and C60 configurations. Therefore, we relocate an oxygen atom to site

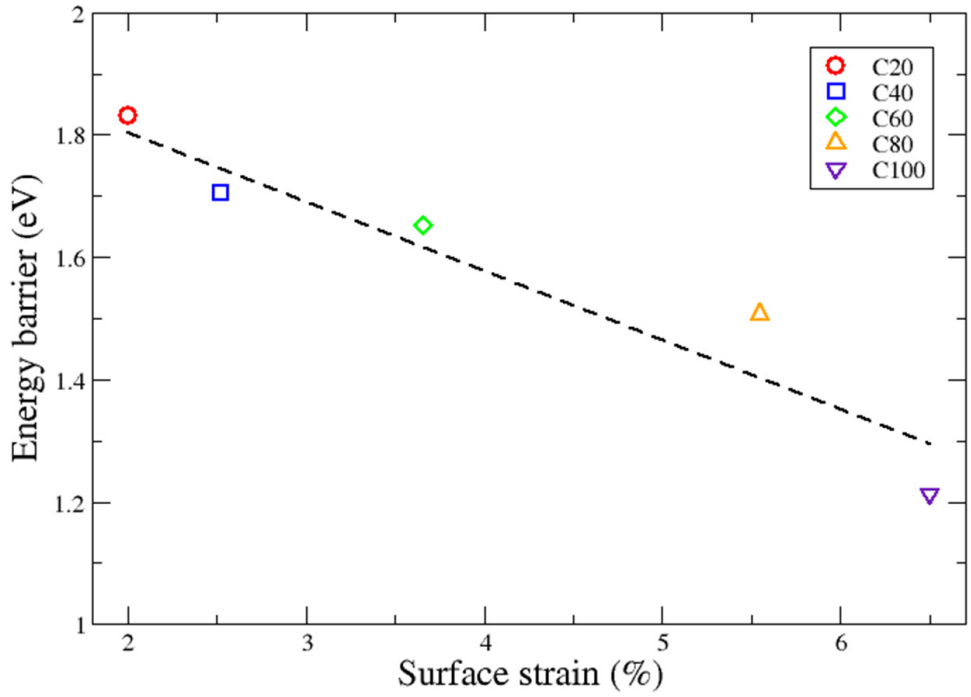

Figure 5.8: Variation of the barrier for oxygen diffusion from surface to subsurface as a function of surface strain of the oxidised Ti nanoparticle. The dashed line is a guide to the eye indicating the strong linear correlation.

13 for all three structures (only for one facet) for this purpose. The relocated oxygen atom is on site 7 for C20 structure, while the displaced oxygen atom is on site 11 for C40 and C60 configurations. The energy difference between the modified structure and the original structure is -0.06, -0.03 and 0.26 for the C20, C40 and C60 configurations. The small energy difference indicates the relocation does not significant influence the adsorption except for C60 structure. The relatively large change in adsorption energy for C60 configuration is because it already has the maximum number of linear O_{ads}-Ti-O_{ads} structures. Fig. 5.8 shows the diffusion barrier as a function of surface strain. An increase of 1 % in the surface strain is shown to decrease the diffusion barrier by 0.1 eV. For predicting the diffusion frequency of oxygen atoms from surface to subsurface of the nanoparticle, we simple use Arrhenius equation with typical vibrational frequency prefactor of 10^{13} Hz. We estimate a relatively high diffusion rate of 0.2 Hz can be achieved at temperatures as low as 700 K for the C100 structure. These results suggests that the surface strain dominates the oxidation of Ti nanoparticles.

5.4 Atomic Arrangements of TiPt Nanoparticle under Oxidation

In the previous sections, we investigated the influence of oxygen adsorption on a pure Ti nanoparticle and analysed the configurations, surface strain and diffusion barriers. In this section, we consider a TiPt bimetallic nanoparticle and study its atomic arrangement for different oxygen concentrations adsorbed on the nanoparticle. TiPt bimetallic nanoparticles are promising catalysts for the polymer electrolyte membrane (PEM) fuel cells [48, 86]. TiPt nanoparticles are usually exposed to an oxygen-rich environment (such as air and water) for applications. Although experimental observations show the TiPt nanoparticles form core-shell structure with single and multiple Pt core(s), the mechanism is not clear [86]. Therefore we use DFT calculation to provide insight into the atomic arrangement of oxidised TiPt nanoparticles. There are six morphologies of nanoparticles normally found in experiments: octahedron (Oh), truncated-octahedron (t-Oh), decahedron (Dh), Ino-decahedron (I-Dh), Marks-decahedron (M-Dh), and icosahedron (Ih) [187]. In order to rearrange the Ti and Pt atoms efficiently, we consider a TiPt nanoparticle in a high-symmetrical icosahedral (Ih) shape. The Ih nanoparticle consists of twenty triangular close-packed (111) facets with twelve vertices. The magic number for the most stable nanoparticle of Ih shape are 13, 55, 147, 309, etc. We consider a Ih nanoparticle with 147 atoms for modelling oxygen adsorption. The selected nanoparticle provides sufficient size for modelling with computationally feasibility. Since the ratio between Ti and Pt in the nanoparticle is approximately 13:1 in the experimental observation [86], we divided the 147 atoms into 134 Ti and 13 Pt atoms (hereafter $TiPt_{147}$), respectively. The number of Pt atoms is equal to the first magic number for the nanoparticles of Ih shape. This means it can form a highly symmetric single core in the centre of the $TiPt_{147}$ nanoparticle. Alternative highly symmetric configurations, such as 12 Pt atoms located at the 12 vertices and 1 Pt atom is located in the centre of the nanoparticle are also possible.

In order to investigate the stability of different atomic arrangements in various oxidation states, we first consider 5 different types of atomic arrangements of the bare $TiPt_{147}$ nanoparticle: (I) Pt and Ti atoms randomly distributed throughout the nanoparticle (random), (II) 12 Pt atoms at each of the vertex sites and 1 Pt atom in the central core site (vertex) (shown in Fig. 5.9(a)), (III) all Pt atoms in a single Ih core in the centre of

the nanoparticle (single-core) (shown in Fig. 5.9(g)), (IV) Pt atoms forming two cores inside the the nanoparticle (double-core) and (V) Pt atoms forming three cores inside the nanoparticle (triple-core) (shown in Fig. 5.9(d)). We consider 3, 1, 1, 2 and 3 different configuration(s) for each of the above types of arrangement, respectively. Four different oxygen adsorptions are applied on the $TiPt_{147}$ nanoparticle, which are 0 ML, 0.5 ML, 1 ML and 2 ML (where ML stands for monolayer). 0 ML corresponds to the bare $TiPt_{147}$ nanoparticle. 1 ML configuration is determined by the highest concentration of oxygen adsorption on the surface of the nanoparticle, with 120 oxygen atoms are located on all available hcp adsorption sites of the nanoparticle surface similar to the configuration shown in Fig. 5.6. 60 oxygen atoms adsorb on the surface fcc sites of the nanoparticles for the 0.5 ML adsorption coverage. According to the investigation on the Ti nanoparticle oxidation, oxygen atoms preferentially adsorb on the octahedral interstitial sites in the subsurface. Hence, 2 ML coverage represents 120 and 60 oxygen atoms on the surface hcp sites and in subsurface octahedral interstitial sites, respectively. Table 5.8 summarises the calculated binding energies of the above 10 atomic arrangements of the nanoparticle with 4 oxidation states (40 configurations in total). The binding energy is defined as,

$$E_{\mathrm{b}} = E_{\mathrm{tot}} - N_{\mathrm{Ti}} E_{\mathrm{Ti}}^{\mathrm{hcp}} - N_{\mathrm{Pt}} E_{\mathrm{Pt}}^{\mathrm{fcc}} - \frac{1}{2} N_{\mathrm{O}} E_{\mathrm{O}_2}, \tag{5.1}$$

where E_{tot} is the total energy of the bare or oxidised TiPt nanoparticle. N_{Ti}, N_{Pt} and N_{O} represents the number of Ti, Pt and O atoms. $E_{\mathrm{Ti}}^{\mathrm{hcp}}$ and $E_{\mathrm{Pt}}^{\mathrm{fcc}}$ are the total energies of a bulk Ti and Pt atom. E_{O_2} is the total energy of an oxygen molecule.

The result of the calculations show that the vertex arrangement of Pt atoms (Fig. 5.9(a)) is the most energetically stable configuration in the absence of oxygen adsorption, but the random configurations also have similar binding energy. The binding energy difference between the more stable configuration (the vertex arrangement) and the less stable one (the random arrangements) is less than 0.002 eV per nanoparticle in vacuum. However, the energy difference significantly increases to about 0.065 eV per nanoparticle when oxygen atoms adsorb on the surface of the nanoparticles. Hence, the $TiPt_{147}$ nanoparticle in the vertex arrangement is the most stable configuration with 0.5 ML oxygen coverage shown in Fig. 5.9(b). As the oxygen coverage increases to 1 ML, the most stable configuration transforms into the triple-cores arrangement (Fig. 5.9(c)). The double-cores arrangement with 1 ML oxygen coverage also shows similar binding energies ($\Delta E_{\mathrm{b}} = 0.011$ eV/nanoparticle) to the triple-cores arrangement. With the further oxidation to 2 ML,

Arrangements	0.0 ML	0.5 ML	1.0 ML	2.0 ML
Vertex	0.563	-1.330	-1.891	-2.431
Single-core	0.619	-1.265	-2.074	-2.648
Random-1	0.566	-1.265	-2.079	—
Random-2	0.565	-1.261	-2.070	-2.486
Random-3	0.570	-1.255	-1.980	-2.418
Double-cores-1	0.632	-1.255	-2.089	-2.539
Double-cores-2	0.603	-1.265	-2.088	-2.607
Triple-cores-1	0.605	-1.267	-2.091	-2.570
Triple-cores-2	0.602	-1.266	-2.070	-2.570
Triple-cores-3	0.591	-1.270	-2.100	-2.583

Table 5.8: Calculated binding energies with respect to 10 different atomic arrangements and 4 different oxygen adsorptions. The unit for these total energies are eV per atom.

Oxygen coverage (ML)	Arrangement	Diameter of nanoparticle (Å)	Average bond length (Å)			
			Ti-Ti	Ti-Pt	Pt-Pt	Ti-O
0.0	Vertex	15.58	2.85	2.73	—	—
0.5	Vertex	15.66	2.95	2.95	—	1.95
1.0	Triple-core-3	16.68	3.05	3.05	2.95	1.95
2.0	Single-core	16.75	3.05	2.75	3.05	2.15

Table 5.9: Calculated diameters and bond lengths for the $TiPt_{147}$ nanoparticles with the most energetically stable arrangement for different oxygen coverages.

the single-core arrangement dominates the configuration of the $TiPt_{147}$ nanoparticle (Fig. 5.9(e)). Table 5.9 summarises the diameters (excluding oxygen atoms) and the average bond length (specific atom pair) of the most energetically stable nanoparticles with respect to different oxygen coverages. The diameter is defined as the length of two diagonal vertices passing through the centre of the nanoparticle. Almost every parameter increases with increasing oxygen coverage, indicating the oxygen adsorption induces lattice expansion of the nanoparticle. One exception in the average Ti-Pt bond length, it becomes smaller for the 2.0 ML coverage than 1.0 ML coverage. The reduction is because the Pt atoms form a single-core making the structure more compact than other arrangements.

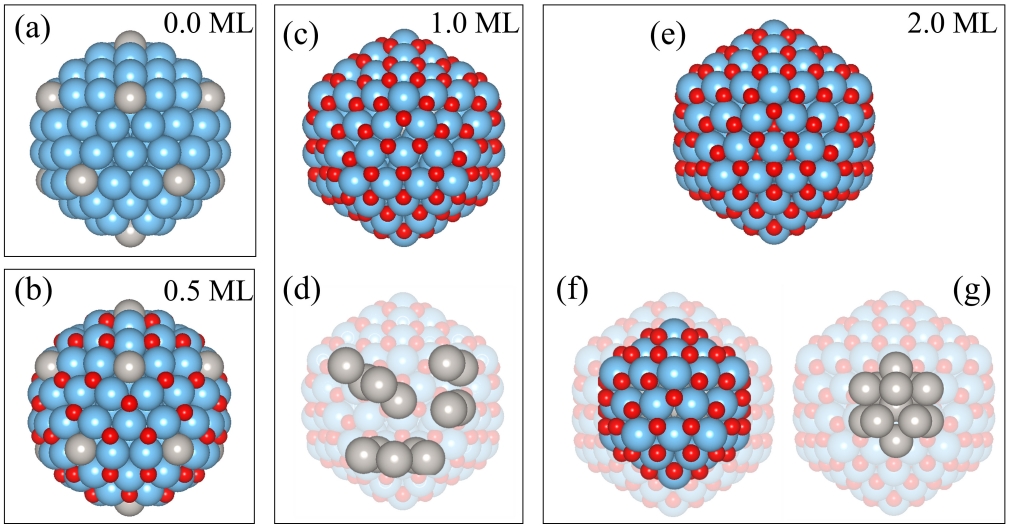

Figure 5.9: Atomic configurations of the $TiPt_{147}$ nanoparticle with different oxygen coverages. (a) The most stable structure of the bare $TiPt_{147}$ nanoparticle. (b) The most stable structure of the oxidised $TiPt_{147}$ nanoparticle with 0.5 of ML oxygen adsorbed. (c) The most stable arrangement with 1.0 ML of oxygen adsorbed and (d) illustrates the three Pt cores in the $TiPt_{147}$ nanoparticle. (e) The most stable single core arrangement for 2.0 ML oxygen coverage. (f) and (g) show the oxygen configuration in the sub-surface layer and the central Pt core, respectively. The silver, blue and red spheres represent the Pt, Ti and O atoms, respectively.

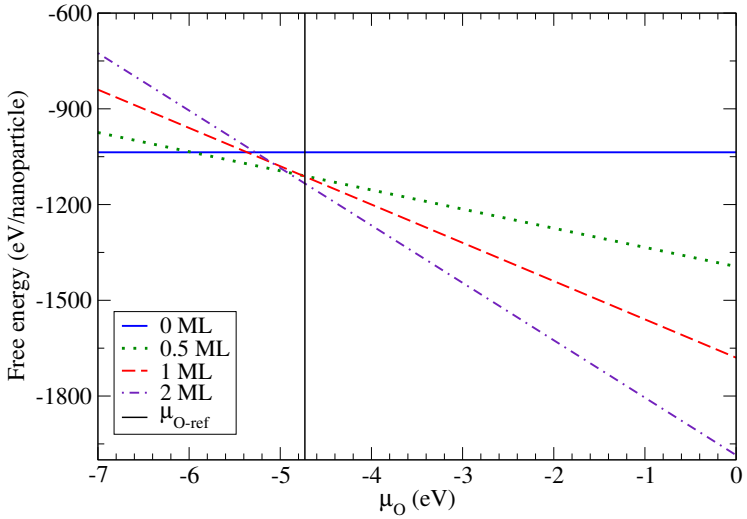

Figure 5.10: Free energy of the $TiPt_{147}$ nanoparticle for different oxygen coverages as a function of oxygen chemical potential.

In order to understand the continuous changing of the atomic arrangement of the $TiPt_{147}$ nanoparticle with oxygen exposure, we calculate the free energy as a function of the oxygen chemical potential. The free energies (Fig. 5.10) are calculated using the total energy with the most stable arrangements for the 4 different oxygen coverages listed in Table 5.9. The upper limit of the oxygen chemical potential is defined as half the energy of oxygen molecule ($\mu_O = E_{O_2}/2$). When $\mu_O < 6.0$ eV, the bare $TiPt_{147}$ nanoparticle in the vertex arrangement is the most stable configuration. For 6.0 eV $\leq \mu_O \leq$ 4.9 eV, the nanoparticle maintains the vertex arrangement with 0.5 ML of oxygen adsorbed on the surface. In terms of $\mu_O \geq 4.9$ eV, 2 ML of oxygen adsorbs on the nanoparticle forming a single-core in the centre. However, the nanoparticle with 1 ML oxygen coverage is not thermodynamically stable at any range of oxygen chemical potential. Fig. 5.10 also shows the chemical potential where metallic hcp-Ti is oxidised into rutile TiO_2. This reference chemical potential suggests the oxygen atoms are oxidised in the surface and subsurface of the nanoparticle easier than in bulk Ti. The above results indicate the oxygen adsorption on nanoparticles is able to modify the atomic arrangement of TiPt bimetallic nanoparticles. This is consistent with the experimental observation of 30 and 90 kDa Ti-Pt nanoparticles forming Pt core(s) with TiO_2 outer shells [86].

5.5 Discussion

Many factors may influence the accuracy of the results in this chapter. In this investigation, the PBE exchange-correlation potential is used for DFT calculations. Therefore, the band gap of the surface TiO_2 will be underestimated in these calculations. However, the PBE functional provides a good prediction for bond lengths (Ti-O, Ti-Ti and Pt-Pt) and the formation enthalpy compared to experiment and other theoretical calculation [188–190]. The band gap issue should not affect the prediction of the total energy or diffusion barriers. Therefore, we believe that the choice of PBE is reasonable for this investigation.

In the Ti nanoparticle investigation, we systematically considered oxygen adsorption in highly-symmetric configurations. The real situation may exhibit oxygen adsorption with much lower symmetry. However, modelling these configurations systematically is not computationally feasible. First-principles molecular dynamics (MD) simulation provides an alternative for assessing the configuration of adsorbed oxygen atoms, but the number of atoms and the degrees of freedom in the nanoparticle calculation is a huge challenge in both computational hardware and time scale. There are not many nanoparticle oxidation experiments that can offer a comparison to our results, but a STEM study found that the penetration of oxygen atoms into metallic nanoparticle is driven by the surface strain on the nanoparticle [191]. The investigation of iron nanoparticle oxidation also shows good agreement with our predicted trend. In addition, we also compare the calculated barrier with a previous theoretical study of the oxygen adsorption and diffusion on α-Ti(0001) surface. In order to compare the barrier energy, we also calculate the barrier for oxygen atom penetration from the surface to subsurface via path-B (see Fig. 5.7). The calculated barrier is comparable to the one obtained for the Ti(0001) surface (1.55 eV) [64]. However, there is a significantly different behaviour with the increasing oxygen coverage between the Ti nanoparticle and the Ti surface. As in section 5.3, the diffusion barrier decreases with increasing oxygen coverage on the nanoparticle surface. However, for the Ti(0001) surface, the barrier reaches a minimum value at 25 % oxygen coverage and a maximum at 75 % [64]. The different trend is due to the lower symmetry of the nanoparticle and the surface strain on the nanoparticle. Especially the strong interaction between oxygen and low-coordinated Ti atoms (such as vertex and edge atoms) on the nanoparticle drives the expansion on Ti-Ti bonds on the facets facilitating the penetration of oxygen atom from

surface to subsurface.

The adsorption geometry and arrangement issues are also presented for the TiPt nanoparticle calculations. We suggest that the systematic investigation of the atomic arrangements is sufficient to describe the number of cores and phase changing with total(free) energy. In the phase diagram calculation, the multiple cores arrangement is not found to be a thermodynamically stable structure over a significant chemical potential range for the small Ih nanoparticle. This is consistent with the experimental observation of different number of cores between larger and smaller TiPt nanoparticles. The TiPt nanoparticle including multiple Pt cores may result in the increased flexibility with larger nanoparticle size and their ability permit more strain associated with multiple cores in the TiPt nanoparticle.

5.6 Conclusions

In summary, we investigated the oxidation of Ti Dh_{181} and $TiPt_{147}$ nanoparticles using DFT calculations. For the former study, we found that the formation of linear O_{ads}-Ti-O_{ads} adsorption features on the metallic nanoparticle can stabilise the adsorption energy and the 40 % oxygen coverage (the C60 configuration) maximises this particular linear configuration. The adsorbing oxygen introduces surface strain and the surface strain gradually increases with the increasing oxygen coverage. Eventually, the Ti-Ti bonds on the nanoparticle facets reach over 8 % strain for a full monolayer coverage. Besides the study of the oxygen adsorption on the nanoparticle, we investigated the diffusion pathway and energy barrier of oxygen penetration from surface to subsurface. The result reveals the oxygen preferentially penetrates at the centre of the facets (surface) to the octahedral interstitial sites (subsurface). The diffusion barrier decreases from 1.83 to 1.21 eV as the increased oxygen coverage indicating the strong correlation between the surface strain and energy barrier. The predicted trend is different with the oxygen diffusion on Ti(0001) surface showing the strain on the nanoparticle plays an important role on the nanoparticle oxidation

For the study of TiPt nanoparticle, we found the similar trend of surface strain with

respect to oxygen coverage. The result demonstrates the atomic arrangement of TiPt bimetallic nanoparticle depending on the oxygen coverage. The bare TiPt nanoparticle presents the vertex (or random) configuration(s). As the oxygen coverage increases, the atomic arrangement transforms from the vertex configuration into the multiple Pt cores and then single Pt core. In addition, the number of Pt cores in the oxidised TiPt nanoparticle depends on both the extent of oxygen coverage and the size of the bimetallic nanoparticle. The latter indicates the larger bimetallic nanoparticles show high acceptance ability for internal strain. Overall, these studies provide atomistic insight into the oxidation of Ti and TiPt nanoparticles and highlight the dilative strain as an important role in metallic nanoparticle oxidation. Moreover, the exposed atoms on bimetallic nanoparticles can be controlled as a function of the pressure of oxygen.

Chapter 6

Au Nanoparticles Supported on ZnO for CO Oxidation

Oxidation of CO is a simple chemical reaction that reveals the beauty of heterogeneous catalysis. Therefore, many investigations use CO oxidation as a prototypical reaction to understand reactivity for heterogeneous structures [192]. Au nanoparticles supported on ZnO nanorods are one of the interesting systems for CO oxidation catalysis that has emerged in the last few decades [92]. In order to improve the catalytic performance of this system recent work reported that pretreating by heating to 500 K in an oxygen-rich environment for an hour gives a 40 % increase in the CO conversion rate compared to original catalytic performance [101]. STEM imaging indicates the Au nanoparticles become partly encapsulated by ZnO during pretreatment and that this may facilitate the CO oxidation. However, the origin of the enhanced performance is not well understood. In addition, although theoretical calculations modelled Au nanoparticles supported on ZnO surfaces for CO oxidation [145, 146], several crucial points have not been addressed including the structure of the interfaces between Au and ZnO or consideration of sufficiently large Au nanoparticles to provide enough adsorption sites for oxygen molecules. Therefore, here we provide more detailed modelling of the system (including more structural details and using larger Au nanoparticles) and calculate the reaction energy to provide deeper atomistic insight into the influence of ZnO encapsulation for CO oxidation on catalytic Au nanoparticles.

In this chapter, we study three main issues relating to Au nanoparticles supported on ZnO surfaces. First of all, section 6.1 and 6.2 detail the structure of Au nanoparticles and defective ZnO surfaces, respectively. Next, section 6.3 investigates various interfaces between Au and ZnO surfaces and predicts the morphology of supported Au nanoparticles. Finally, section 6.4 describes the atomic model of ZnO encapsulated Au nanoparticles on ZnO surfaces and investigates CO oxidation with different configurations of adsorbed oxygen.

6.1 Predicted Properties of Au and Au Nanoparticles

In order to predict the morphology of Au nanoparticles, we calculate the formation energy of low-index fcc Au surfaces for constructing the Au nanoparticle using the Wulff construction. The Au calculation is carried out using the PBE exchange-correlation potential, the primitive cell of fcc Au is optimised with a 13×13×13 MP grid for BZ sampling and the cut-off energy is 400 eV for expansion of the plane-wave wavefunction. The optimised lattice constant of bulk Au is predicted to be 4.14 Å which is consistent with other PBE calculations (4.17 Å) and experimental observations (4.08 Å)[94]. We consider three low-index surfaces, (001), (110) and (111), and calculate their formation energies to predict the equilibrium morphology of the free Au nanoparticles. The atomic structures of these surfaces are shown in Fig. 6.1. The dimensions of supercells for (001), (110) and (111) surface calculations are 4.15×4.15×30 $Å^3$, 4.15×2.93×30 $Å^3$ and 2.93×5.08×30 $Å^3$, respectively. These supercells contain a vacuum gap at least 10 Å normal to the surfaces in the z-direction. A 7×7×1 MP grid is used for BZ sampling to optimise the Au surface structures with 1 k-point in the direction normal to the surfaces. Table 6.1 summarises the calculated formation energies of the three optimised Au surfaces. The (111) surface is the most energetically stable surface with $\gamma_{111} = 0.656$ J/m^2, meanwhile (110) and (001) surfaces show similar formation energies of 0.87 J/m^2.

By using the Wulff construction, the predicted morphology of the Au nanoparticle is truncated-octahedral (t-Oh) as shown in Fig. 6.2(a) consisting of six (001) facets and eight (111) facets. The atomic model (shown in Fig. 6.2(b)) demonstrates the unsupported Au nanoparticle is a strained fcc structure. The area of the (111) facets accounts for 93

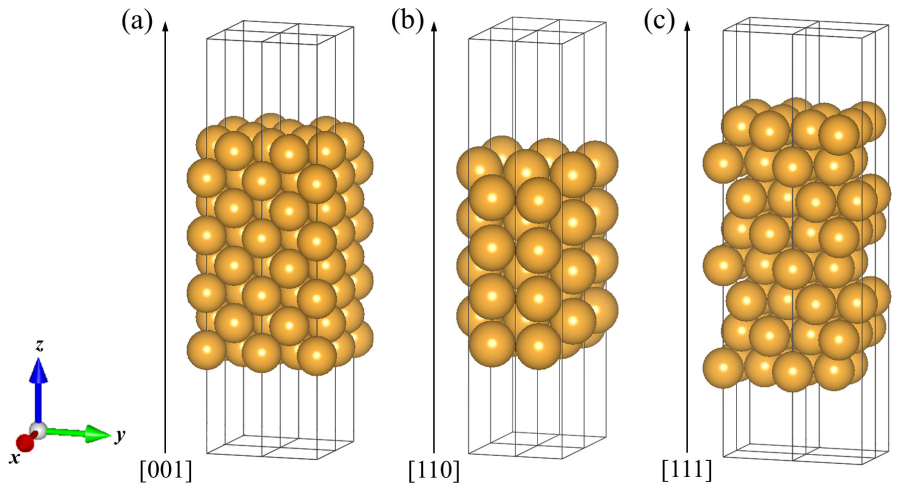

Figure 6.1: Surface supercells for (a) Au (001), (b) Au (110) and (c) Au (111) surfaces with at least 10 Å vacuum gap along z-axis. The dimensions of the supercells are 4.15×4.15×30, 4.15×2.93×30 and 2.93×5.08×30 Å^3, respectively.

Surface	Formation energy (J/m^2)	Other works (J/m^2)
(001)	0.869	0.873 [94]
(110)	0.872	0.900 [93]
(111)	0.656	0.734 [94]

Table 6.1: Calculated surface formation energies for the three low-index surfaces of fcc Au showing a good agreement with recent DFT calculations.

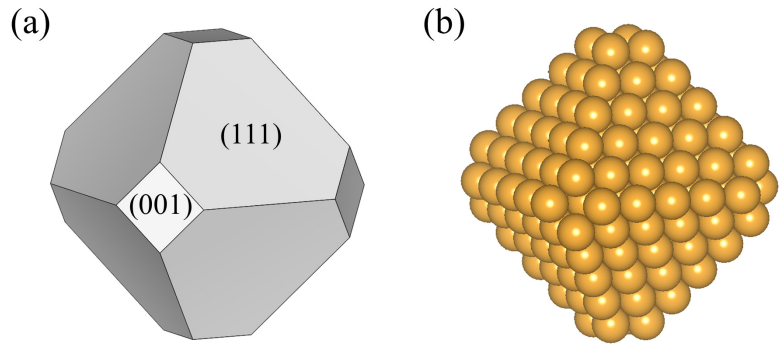

Figure 6.2: The predicted shape of the unsupported Au t-Oh nanoparticle obtained using the Wulff construction. (a) The predicted morphology and (b) an atomic structure consisting of 225 Au atoms.

% of the total area. The calculated proportion of (111) surface is in good agreement with a recent theoretical result, which predicted that the most energetically stable Au nanoparticle (within 20 nm) in t-Oh shape should consist of 90 % (111) facets using numerical minimisation of the total free energy [96].

6.2 Stabilities of Defects on Wurtzite ZnO Surfaces

For overcoming the well-known band gap problem in DFT calculations of ZnO, recent work introduced the GGA+NLEP+U method to successfully correct the issue self-consistently [108]. The GGA+NLEP+U method is described in section 3.3. However, the stability of native point defects in bulk ZnO using the GGA+NLEP+U method has not been considered. Therefore, we firstly study the stabilities of intrinsic defects in ZnO and then investigate the behaviour of possible defects on ZnO surfaces.

6.2.1 Fundamental properties of ZnO

For calculations of bulk wurtzite ZnO a 13×13×13 MP grid is used for BZ sampling. The empirical parameters, β, of the NLEP method are as follows: $\Delta V_{\mathrm{Zn},s} = +9.4$ eV, $\Delta V_{\mathrm{Zn},p} = -1.2$ eV, $\Delta V_{\mathrm{O},s} = -6.4$ eV and $\Delta V_{\mathrm{O},p} = -2.0$ eV. For the formulation of GGA+U, we consider the parametrisation of Ref. [108]. A U value of +7.0 eV is applied to the d-orbitals

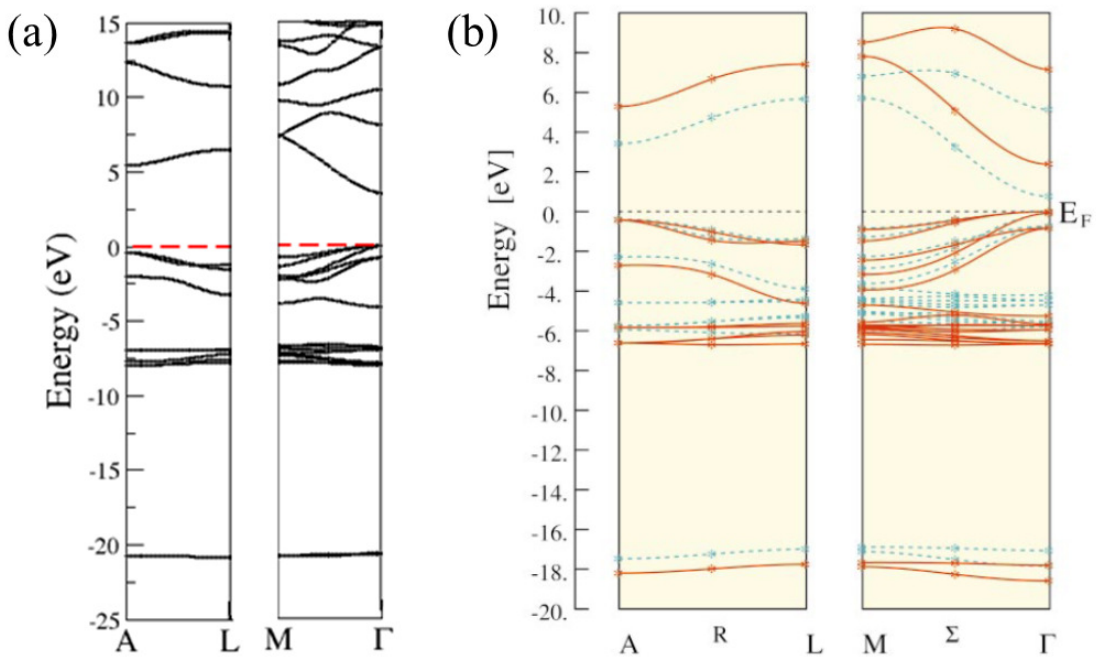

Figure 6.3: The calculated band structures of wurtzite ZnO. (a) GGA+NLEP+U method. The red-dashed line represents the Fermi level. (b) GW calculation (refers to ref. 193). The solid and dashed lines in figure (b) represent the results from GW calculation and LDA method.

of Zn. The calculated lattice constants a and c/a are 3.20 Å and 1.58 respectively and the calculated band gap is 3.20 eV at the Γ-point. These values are in good agreement with experiment (3.4 eV). In order to confirm the electronic structure is described accurately we calculate the band structure of wurtzite ZnO with GGA+NLEP+U method and compare to a previous all-electron GW calculation [193]. The calculated band structures are shown in Fig. 6.3. The results show that the core states (states between -5 to -10 eV and below -20 eV) are down shifted several eV compared to the GW calculations. However, valence electrons band structure (between -5 and 0 eV) are in very good agreement with the GW calculation. In addition, the result of conduction band from GGA+NLEP+U is consistent with the GW calculation as well. Thus, the GGA+NLEP+U method appears a reliable approach for modelling the electronic structure of ZnO.

6.2.2 Points defects in bulk ZnO

In order to ensure that the stability of native point defects in bulk ZnO obtained using the GGA+NLEP+U method is reliable, we compare the formation energy and transition level of several point defects to other theoretical results. The dimensions of the supercell used for defect calculations are 12.78×11.07×20.24 Å^3 (containing 64 primitive cells of ZnO). We consider oxygen vacancy (V_O), zinc vacancy (V_{Zn}) and zinc interstitial (Zn_i) defects and calculate their formation energy. Besides those neutral defects, we also calculate the formation energy of some charged defects. The negatively charged defects are V'_{Zn} and V''_{Zn}. The positively charged defects are $V^{\cdot}_{O}$, $V^{\cdot\cdot}_{O}$, $Zn^{\cdot}_{i}$ and $Zn^{\cdot\cdot}_{i}$. Thus, we consider nine defects in total for formation energy calculations. For predicting the precise formation energy of point defects in periodic systems, image charge correction and potential alignment are applied to the formation energies. Table 6.2 summarises the potential alignment correction for three defect types corresponding to different charge states. The calculated image charge correction for 0, 1+ (1-) and 2+(2-) charged supercell are 0, 0.13 and 0.53 eV, respectively. The static dielectric constant and Madelung constant used in image charge correction are 6.00 and 1.68, respectively. The static dielectric constant is obtained from the GGA+NLEP+U method and is consistent with a recent DFT calculation (7.24) [194].

Fig. 6.4 shows the most stable point defects as a function of Fermi level between the VBM and CBM of bulk ZnO in oxygen-poor and -rich conditions. The chemical potential of oxygen and zinc atoms for oxygen-poor condition are,

$$\mu_O = \frac{1}{2}E_{O_2} + \Delta E_{ZnO}, \quad \mu_{Zn} = E_{Zn}^{hcp}, \tag{6.1}$$

where E_{O_2} represents the total energy of an oxygen molecule, ΔE_{ZnO} is the formation enthalpy of wurtzite ZnO and E_{Zn}^{hcp} represents the total energy of bulk Zn in hcp structure. Meanwhile, the two chemical potentials under oxygen-rich condition are,

$$\mu_O = \frac{1}{2}E_{O_2}, \quad \mu_{Zn} = E_{Zn}^{hcp} + \Delta E_{ZnO}. \tag{6.2}$$

In this formulation, the chemical potential of an oxygen atom refers to half energy of the oxygen molecule. The calculated formation enthalpy (ΔE_{ZnO}) of ZnO is -4.75 eV per formula unit, while the experimental value of the formation enthalpy is -3.58 eV [129]. Fig. 6.4(a) demonstrates the both oxygen vacancy and zinc interstitial defects are most energetically stable defect depending on the Fermi level in oxygen-poor condition, whereas

	Potential alignment (eV)		
Charge state	0	1	2
V_O (+)	-0.01	0.11	0.18
V_{Zn} (-)	-0.06	-0.17	-0.26
Zn_i (+)	0.15	0.21	0.29

Table 6.2: The potential alignments of different defects and charge states with respect to the 4×4×4 supercell. The signs in parentheses indicate the defect is positively (+) or negatively (-) charged.

the zinc vacancy defect is the most stable under oxygen-rich conditions as shown in Fig. 6.4(b).

Table 6.3 summarises the transition levels of the defects, the energy reference (0 eV) is the Fermi level at the top of the VBM. V_O has transition levels $\varepsilon(2+/1+)$ and $\varepsilon(1+/0)$ at 1.8 and 1.5 eV below the CBM. This means this defect behaves as a deep n-type donor similar to the results of hybrid and GW calculations as well as experimental observation [121, 195]. The transition levels $\varepsilon(0/1+)$ and $\varepsilon(1+/2+)$ for V_{Zn} are 0.1 and 0.6 eV above the VBM, respectively, resulting in a shallow acceptor. The is again in good agreement with the experimental photoluminescence (PL) emission of 3.09 eV from the CBM to zinc vacancy [196]. The doubly charged zinc interstitial, $Zn_i^{\cdot\cdot}$, is most stable across the whole range of Fermi energies in the gap with the transition levels above the CBM. This result is also in agreement with hybrid calculations. Altogether these results indicate the GGA+NLEP+U method is a promising method for predicting the stability of native point defects in ZnO but much cheaper than hybrid or GW approaches.

6.2.3 Stability of periodic defects on ZnO surfaces

XRD and STEM observations indicate that ZnO nanorods are wurtzite structured, elongated in the [0001] direction and consist of $(10\bar{1}0)$ and $(11\bar{2}0)$ surfaces along their lengths. Fig 6.5 (top figures) show the supercells used to model the ZnO $(10\bar{1}0)$ and $(11\bar{2}0)$ surfaces which have unit cell dimensions ($x \times y$) of 3.19×5.06 and 5.53×5.06 Å^2, respectively. The bottom figures of Fig 6.5 show the side view of the ZnO surface supercells. The calculated

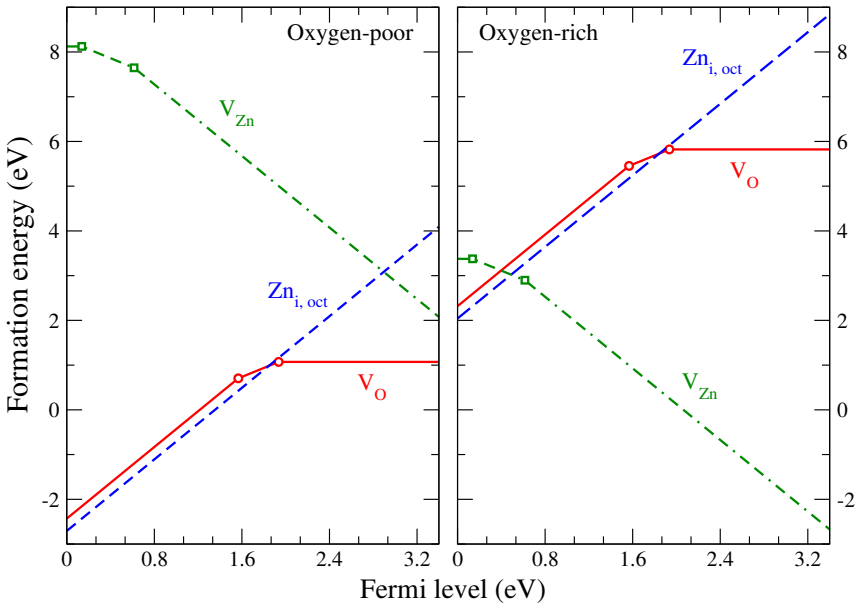

Figure 6.4: Calculated defect formation energies of selected intrinsic defects in ZnO. The nodes (red circles and green squares) represent transition levels.

formation energy for former and latter surfaces are 1.26 and 1.35 J/m^2, respectively. In order to assess the stability of possible defects on ZnO surfaces, we calculate the segregation energy of the defects. The segregation energy is defined as,

$$E_{\mathrm{s}} = E^{\mathrm{d}}_{\mathrm{surface}} - E^{\mathrm{d}}_{\mathrm{bulk}}, \tag{6.3}$$

where $E^{\mathrm{d}}_{\mathrm{surface}}$ and $E^{\mathrm{d}}_{\mathrm{bulk}}$ represent the total energy of ZnO slab with a defect on surface and in the bulk, respectively. In this calculation, we only consider oxygen vacancy and zinc interstitial defects (the stable defects for n-type ZnO). In addition, these two defects may provide Zn atoms which go on to form the ZnO encapsulation under oxygen-rich conditions.For n-type ZnO, the charge state of the defect should close to the CBM with respect to the Fermi level. Therefore, oxygen vacancy and zinc interstitial are selected as neutral and 2+ charge states, respectively. Fig. 6.6 shows the segregation energy of defects as a function of the thickness of the ZnO slabs. The result demonstrates V_O preferentially segregated to the surface with -0.55 eV segregation energy (Fig. 6.6(a)) on both ZnO surfaces. However, Fig. 6.6(b) shows $Zn_i^{\cdot\cdot}$ has the positive segregation energy suggesting $Zn_i^{\cdot\cdot}$ is more energetically stable in the bulk-like site. The result indicates the oxygen vacancy (V_O) is more likely to be present on ZnO surfaces, whereas the zinc interstitial ($Zn_i^{\cdot\cdot}$) is not.

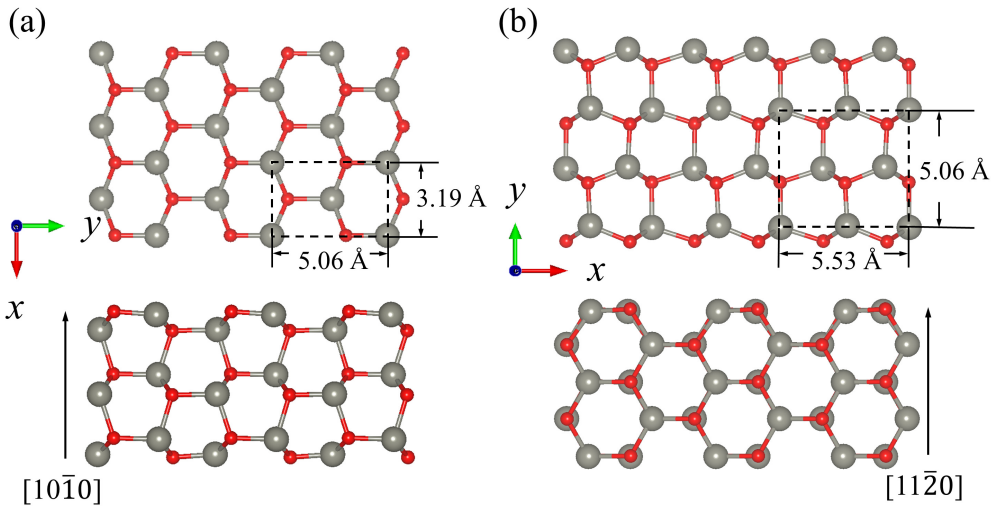

Figure 6.5: The atomic models and dimensions of (a) ZnO (10$\bar{1}$0) and (b) ZnO (11$\bar{2}$0) surfaces.

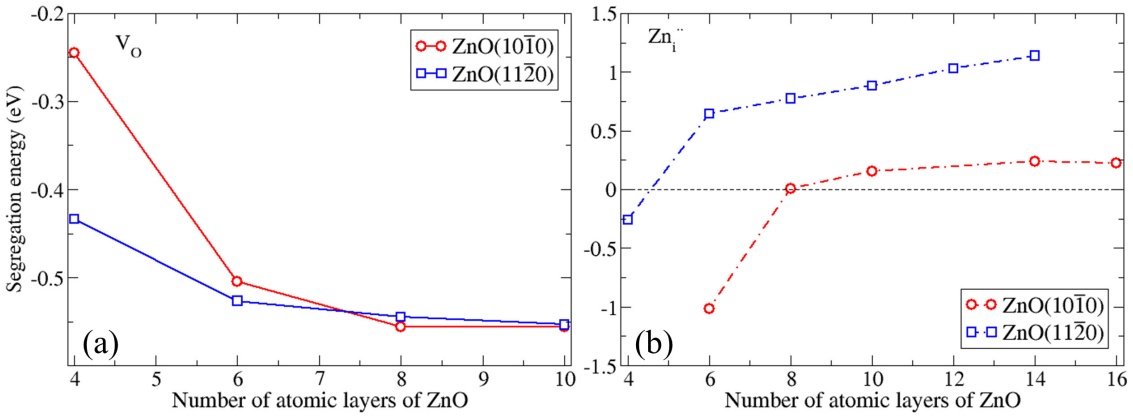

Figure 6.6: The segregation energy of defects as a function of thickness of ZnO slabs for ZnO (10$\bar{1}$0) and (11$\bar{2}$0) surfaces. (a) and (b) represent the segregation energy of V_O and $Zn_i^{\cdot\cdot}$ respectively.

Defect	q/q'	$\varepsilon(q/q')$	$\varepsilon(q/q')$
		This work	Previous work
V_O	2+/1+	1.6	–
	1+/0	1.9	–
	2+/0	–	1.4 (GW calculation) [195]
V_{Zn}	0/1-	0.1	0.3 (GGA+U), 0.22 (GGA) [125]
	1-/2-	0.6	1.1 (GGA+U), 0.75 (GGA) [125]
Zn_i	2+/1+	–	3.4 (HSE) [109]
	1+/0	–	3.4 (HSE) [109]

Table 6.3: Thermodynamic transition levels of point defects in ZnO. The transition level must be in the range between the CBM and VBM. The transition levels of zinc interstitial is above the VBM.

Before we calculate the adhesion energy of interfaces between Au and ZnO surfaces, it is necessary to understand the concentration of the possible defects on ZnO surfaces. The surface concentration can be predicted using the Langmuir-McLean equation [197],

$$\frac{n_\mathrm{s}}{n_\mathrm{b}} = e^{-E_\mathrm{s}/k_\mathrm{B}T}, \tag{6.4}$$

where n_s and n_b are the surface and bulk defect concentration and E_s is the segregation energy. We convert the defect concentration into an average separation between defects using the following relation,

$$n^{-1/3} = \ell, \tag{6.5}$$

where ℓ is the distance between two defects. Hence, Eq. 6.4 can be rewritten as,

$$\left(\frac{n_\mathrm{s}}{n_\mathrm{b}}\right)^{-1/3} = \frac{\ell_\mathrm{s}}{\ell_\mathrm{b}} = e^{E_\mathrm{s}/3k_\mathrm{B}T}. \tag{6.6}$$

Using a set of reasonable parameters (n_b=10^{17} cm^{-3} and T=600 to 900 K), the calculated surface concentration of the n-type defects (V_O) on ZnO surfaces is approximately 1 nm^{-2}.

6.3 Structures and Adhesion Energies of Au/ZnO Interfaces

6.3.1 Interfaces between Au and ZnO surfaces

In order to determine the morphology of Au nanoparticles on ZnO supports using the Wulff-Kaishew construction, we calculate the adhesion energy of the interface between Au and ZnO surfaces. In the interface calculation, we consider Au (001), (110) and (111) surfaces attaching on ZnO $(10\bar{1}0)$ and $(11\bar{2}0)$ surfaces. Hence, there are six different interfaces between Au and ZnO surfaces. Table 6.4 summaries the result for the optimised interfaces for the respective supercells. Each supercell includes at least 8 layers of ZnO and 8 layers of Au. The particular rotation (R) of several Au surfaces for the interface are also denoted in Table 6.4. The uniaxial lattice strain of the Au surfaces are in the range from 0 to 10 % depending on the interfaces, but the interface with the smallest strain does not necessary correspond to the most stable adhesion energy. The interface between Au (111) and the ZnO $(10\bar{1}0)$ surface shows the most stable adhesion with $E_{\mathrm{ad}} = -0.8$ J/m^2. The three interfaces between Au and ZnO $(11\bar{2}0)$ offer similar adhesion energies around -0.4 J/m^2. Fig. 6.7 shows the atomic structures of the six interfaces. Due to the lattice mismatch at the interface, the Au atoms of (001) and (110) surfaces are not aligned to specific sites of the ZnO surfaces. The Au atom can sit on the top of the oxygen (zinc), the hollow site of the hexagonal structure and the bridge site of two oxygen (zinc) atoms. However, for the interfaces between Au (111) and ZnO surfaces the Au atoms locate directly above the oxygen atoms as shown in Fig. 6.7(c) and (f). The Au-O bonding arrangement is more stable and decreases the adhesion energy. This stable bond formation also has been reported in the system of Au nanoparticles supported on MgO (001) surface [134].

In order to provide deeper insight into the interactions between Au and ZnO, we perform Bader analysis (as described in section 3.4.6) for each slab. Fig. 6.8 shows both average distance (between the Au and ZnO surfaces) and adhesion energy as a function of the charge transfer. The trend shows that as the charge transfer increases the separation distance and adhesion energy decrease. However, the adhesion energy of Au surfaces supported on ZnO $(11\bar{2}0)$ is less sensitive to charge transfer compared to interfaces between Au and ZnO $(10\bar{1}0)$. We suggest the reason of the insensitivity is due

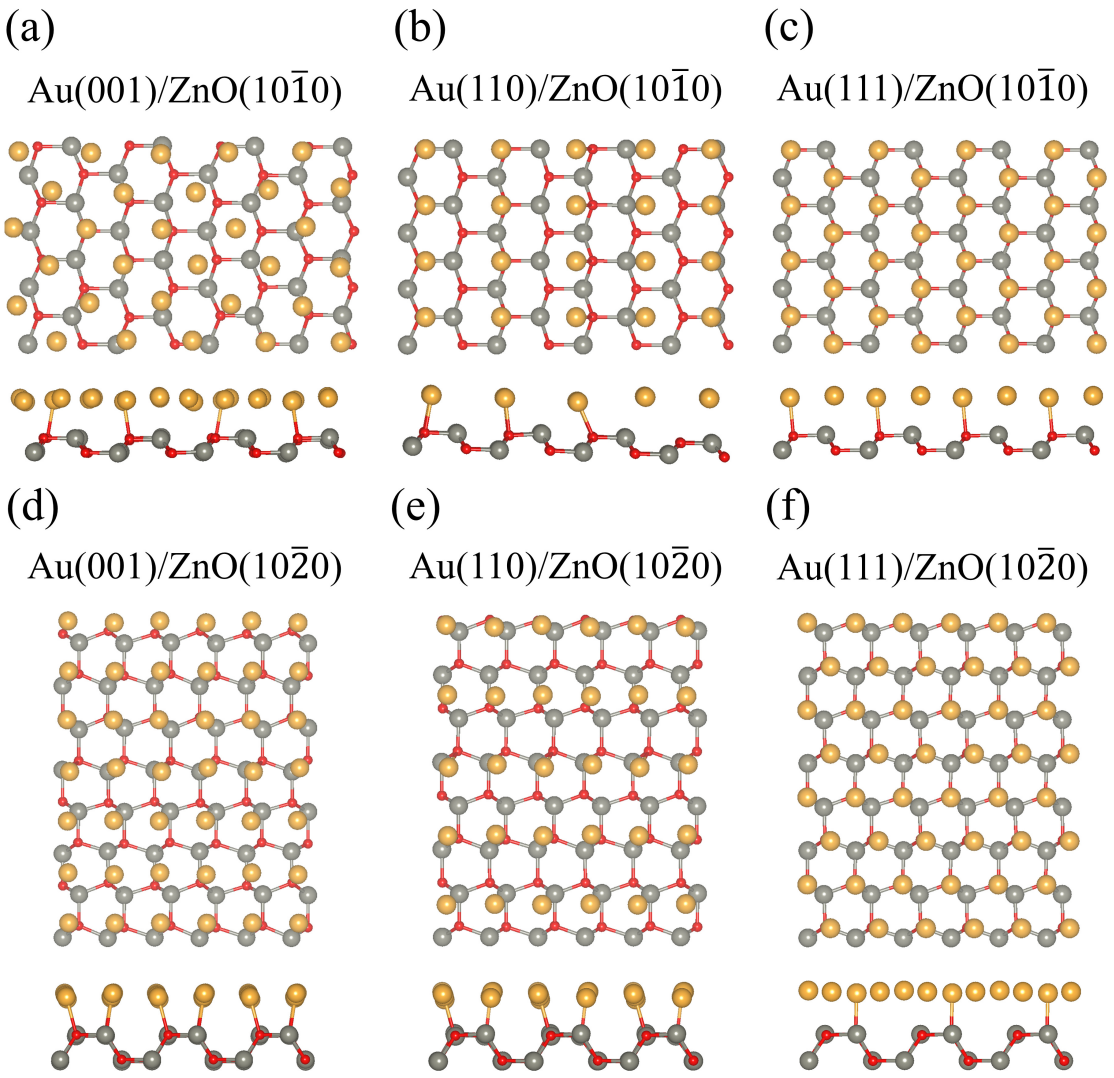

Figure 6.7: Atomic structure of the interfaces between Au and ZnO surfaces. The top and bottom of each panel show the top and side views respectively. The gold, grey and red spheres represent the Au, Zn and O atoms, respectively.

ZnO($10\bar{1}0$)	Au(001)	Au(110)	Au(111)
Size of supercell (Å^2)	12.78×20.24	3.19×20.24	3.19×5.06
Au(x,y)	3×5	1×5 R90	1×1
ZnO(x,y)	4×5	1×4	1×1
Lattice Strain of Au (x,y)	-3 %, 3%	-8 %, 2%	-9 %, 0%
E_{ad} (J/m^2)	-0.574	-0.717	-0.812
ZnO($11\bar{2}0$)	Au(001)	Au(110)	Au(111)
Size of supercell (Å^2)	5.53×15.18	5.53×20.24	5.53×5.06
Au(x,y)	2×5 R45	2×5 R90	2×1
ZnO(x,y)	1×3	1×4	1×1
Lattice Strain of Au (x,y)	5 %, -3%	5 %, 2%	5 %, 0%
E_{ad} (J/m^2)	-0.433	-0.421	-0.413

Table 6.4: Properties of the interfaces between Au and ZnO surfaces including the dimensions of supercells, the number of repeated unit cells of Au and ZnO surfaces, the lattice strain of Au surfaces and the adhesion energies. Apart from the adhesion energy, all of the properties are shown for both x and y directions. The unit cell of Au and ZnO surfaces are presented in Fig. 6.1 and Fig. 6.5, respectively.

to differences in the bond formation between interface Au atoms and the sub-surfaces of the ZnO surfaces. If we recall the ZnO atomic structure (side view in Fig. 6.5) the interplanar distance between ZnO bilayer (two topmost layers) is 0.85 and 1.56 Å for ZnO ($10\bar{1}0$) and ZnO ($11\bar{2}0$) surfaces, respectively. Consequently, the sub-surface of the ZnO ($10\bar{1}0$) has a stronger interaction with the interfacial Au atoms which further decreases the adhesion energy. Therefore, the calculation shows the Au surfaces deposition on ZnO ($10\bar{1}0$) surface is more stable than sputtering on ZnO ($11\bar{2}0$) surface.

6.3.2 The influence of defects at interfaces

Since the Au nanoparticles are deposited on the ZnO nanorods, surface defects may influence the interaction between Au and ZnO surfaces. Thus, in order to understand the change of morphology with respect to defects in the ZnO support, we calculate the adhesion energy for the six above interfaces. We only consider the interfaces with V_O between

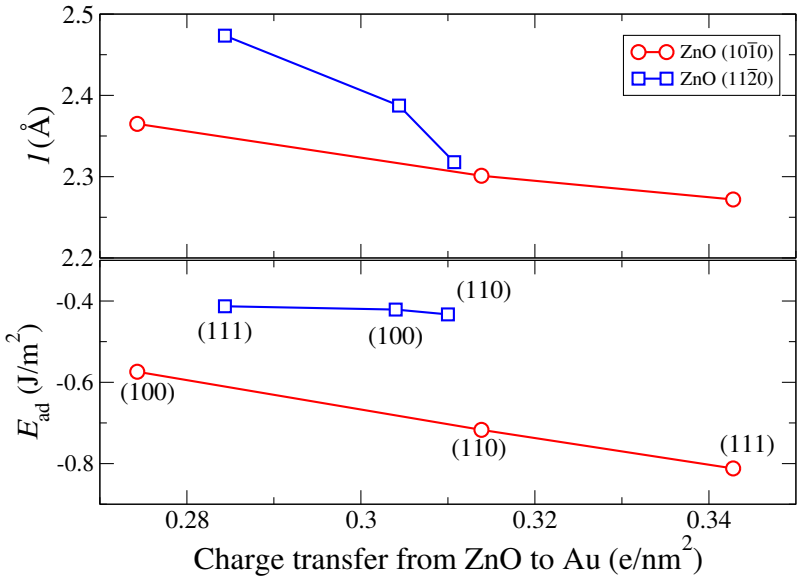

Figure 6.8: The average separation distance (between Au and ZnO surfaces) (top) and the adhesion energy (bottom) as a function of the charge transfer (from ZnO to Au surfaces).

the Au and ZnO surfaces since the $Zn_i^{\cdot\cdot}$ is unstable presenting on the surface of ZnO surfaces. Table 6.5 summaries the basic properties (similar to Table 6.4), including charge transfer and the concentration of the oxygen vacancy at the interfaces. The results demonstrate that the presence of oxygen vacancies at the interface decreases the adhesion energy and increases the charge transfer from ZnO to Au. Fig. 6.9 demonstrates the relation between adhesion energy, charge transfer and defect concentration. The figure shows an increase in the oxygen vacancy concentration of 1 nm^{-2} decreases the adhesion energy by 0.4 J/m^2 and increases the charge transfer by 1 e/nm^2. Overall, the result indicates oxygen vacancies strengthen the interaction between Au and the ZnO surface.

6.3.3 Stability of zinc interstitial at the interfaces between Au and ZnO

The positive segregation energy of $Zn_i^{\cdot\cdot}$ (shown in Fig. 6.6) indicates the positively charged defect is unstable to segregate to the surface of ZnO. However, when the Au surfaces is attached to the ZnO surface, the Au as an electron reservoir may change the stability of zinc interstitial. In order to assess the stability of zinc interstitial, we calculate the segregation energy of neutral zinc interstitials at the interface of Au (111) and ZnO surfaces (including (10$\bar{1}$0) and (11$\bar{2}$0) surfaces). The cubic dimensions of the supercell used are

ZnO($10\bar{1}0$)	Size of supercell (A^2)	Au (x,y)	ZnO (x,y)	Strain (x,y)	Conc. (nm^{-2})	q (e/nm^2)	E_{ad} (J/m^2)
Au (001)	12.78×20.24	3×5	4×5	-3 %, 3%	1.2	1.4	-0.96
Au (110)	9.59×20.24	3×5 R90	3×4	-8 %, 2%	1.0	1.3	-1.04
					2.1	2.2	-1.35
Au (111)	9.59×10.12	3×2	3×2	-9 %, 0%	1.0	1.2	-1.1
					2.1	2.2	-1.38
ZnO($11\bar{2}0$)	Size of supercell (A^2)	Au (x,y)	ZnO (x,y)	Strain (x,y)	Conc. (nm^{-2})	q (e/nm^2)	E_{ad} (J/m^2)
Au (001)	11.06×15.18	4×5 R45	2×3	8 %, 3%	1.2	0.8	-0.87
Au (110)	11.06×20.24	2×5 R90	2×4	-8 %, 2%	0.9	1.1	-0.60
					1.8	2.0	-0.95
Au (111)	11.06×10.12	4×2	2×2	5 %, 0%	0.9	1.2	-0.77
					1.8	2.0	-1.17

Table 6.5: Properties of Au/ZnO interface with oxygen vacancies present at the surface.

9.59×10.12×33.00 and 11.06×10.12×33.00 $Å^3$ for Au (111) supported on ZnO ($10\bar{1}0$) and ($11\bar{2}0$) surfaces, respectively. Both supercells consist of 6 layers of Au (111) structure and 8 layers of ZnO. Table 6.6 summarises the segregation energy, formation energy and strain energy of Zn_i at interfaces of Au(111)/ZnO. The result shows the defect is energetically stable in the Au(111)/ZnO interfaces rather than incorporation in bulk ZnO. Theformation energy and stain energy show the zinc interstitial providing similar stability at these two Au/ZnO interfaces. In addition, Bader analysis shows that the charge state for zinc interstitials is approximately -1 e at these interfaces, which is as same as zinc atoms in bulk ZnO.

6.3.4 Morphologies of Au nanoparticles on ZnO supports

The morphology of the supported Au nanoparticles are determined by the shape of the free nanoparticle and the adhesion energy of the interfaces between Au and ZnO surfaces. By using the Wulff-Kaishew construction, the predicted morphologies of supported Au nanoparticles are shown in Fig. 6.10. Fig. 6.10(a), (b) and (c) represent the Au nanopar-

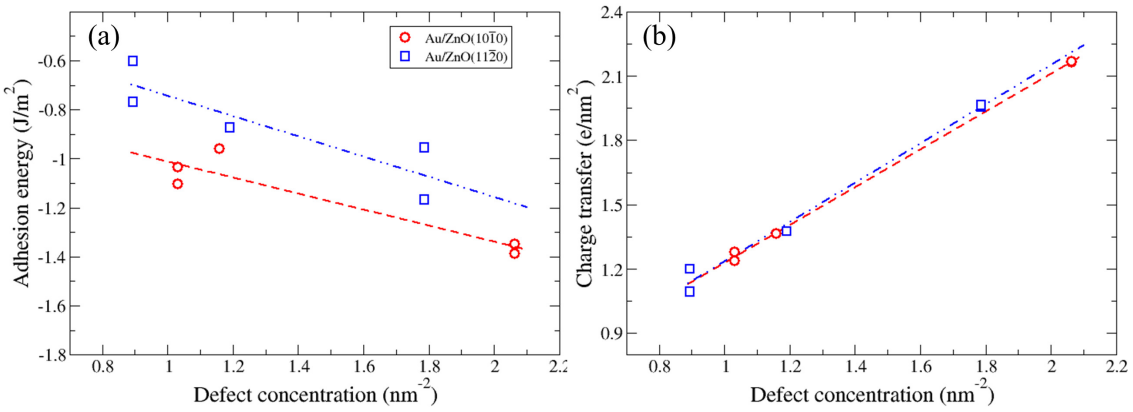

Figure 6.9: Variation of (a) adhesion energy and (b) charge transfer from ZnO to Au surfaces with oxygen vacancy concentration. The red circles and blue squares represent Au surfaces attaching on the ZnO (10$\bar{1}$0) and (11$\bar{2}$0) surface, respectively. The dashed line is the guide to the eye highlighting the linear correlation.

	Au(111)/ZnO(10$\bar{1}$0)	Au(111)/ZnO(11$\bar{2}$0)
charge state	0	0
E_{seg}(eV)	-3.2	-1.6
E_{f} (eV)	0.81	0.70
E_{s} (eV)	1.86	2.09

Table 6.6: The formation energy, strain energy and segregation energy with respect to zinc interstitials at two different interfaces.

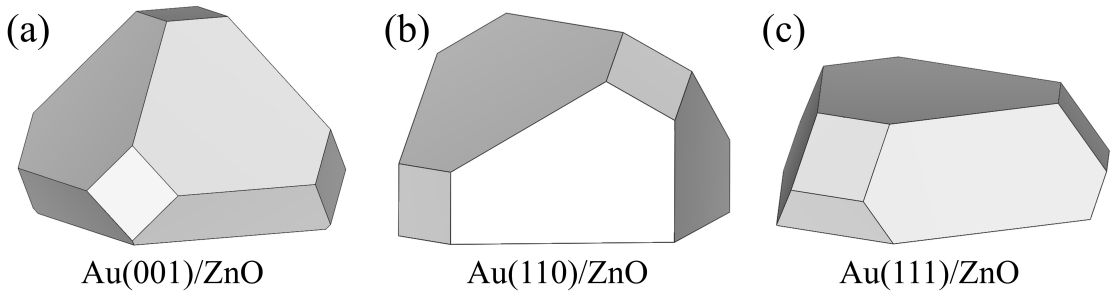

Figure 6.10: Three different morphologies of the supported Au nanoparticles on ZnO surfaces. (a), (b) and (c) represent the Au (001), (110) and (111) surfaces depositing on both ZnO surfaces (includes $(10\bar{1}0)$ and $(11\bar{2}0)$), respectively.

ticles with supported facets of Au (001), (110) and (111) on ZnO surfaces, respectively. In addition, the orientation of ZnO support is independent of the equilibrium morphology of supported Au nanoparticle, which only influences the height and the contact angle of the nanoparticle by changing the formation energy of the interfaces ($\gamma + E_{\mathrm{ad}}$). For example, the height of nanoparticle supported on ZnO $(10\bar{1}0)$ surface is lower than the one on ZnO $(11\bar{2}0)$. We note that the predicted morphologies can all be found in experimental STEM observations of ZnO supported Au nanoparticles [138].

In order to determine the most stable morphology of supported Au nanoparticle, we calculate the total surface free energy of supported Au nanoparticles to assess the stability. The total surface free (TSF) energy of a nanoparticle is defined as,

$$E_{\mathrm{TSF}} = \sum_{(ijk)} A_{(ijk)}\gamma_{(ijk)}, \tag{6.7}$$

where A_{ijk} and γ_{ijk} represent the area and the formation energy of the specific (ijk) facets, respectively. Fig. 6.11 shows the surface free energy of supported Au nanoparticles (corresponding to Fig. 6.10) as a function of diameter (d) of the Au nanoparticles. While $d = \sigma^{1/3}$ and σ represents the volume of a nanoparticle. The range of diameters for the calculated nanoparticles is from 1 to 6 nm. For ZnO $(10\bar{1}0)$ support, the result (Fig. 6.11(a)) shows that the nanoparticles with interfaces between the Au (111) facet and the ZnO $(10\bar{1}0)$ surface provide the smallest total free energy in the given volume (between 1 to 216 nm^3). However, Fig. 6.11(b) demonstrates the similar total surface energy among three different morphologies of nanoparticles on ZnO $(11\bar{2}0)$ support. The different behaviour between the nanoparticles on two ZnO supports is due to the forma-

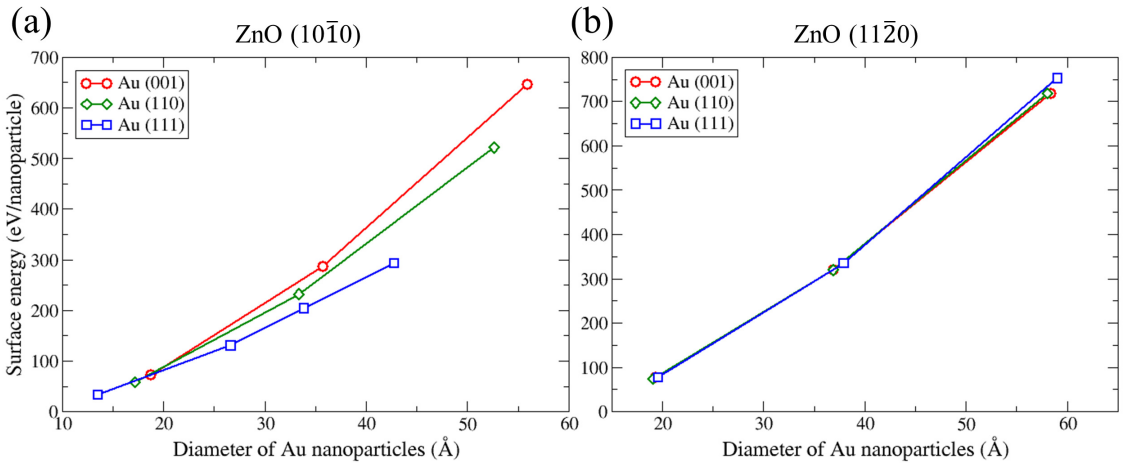

Figure 6.11: The total surface energy as a function of diameter of the Au nanoparticles. (a) and (b) represent the Au nanoparticles supported on ZnO (10$\bar{1}$0) and (11$\bar{2}$0) surfaces with different interfaces, respectively.

tion energy of the interfaces. The smaller formation energy at the interface provides the smaller total surface energy. Although the calculated total surface energy demonstrates the different stability to the nanoparticles, the energy difference per Au atom is less than 10^{-2} eV. Therefore, we suggest these morphologies are all thermodynamically stable in room temperature with nm size.

6.4 O_2 Adsorption and CO Oxidation Reaction on Au NPs supported on ZnO

6.4.1 Au nanoparticles on ZnO supports

In order to study the CO oxidation reaction on Au nanoparticles supported on ZnO, we construct supercells containing Au nanoparticle on the ZnO surfaces and optimise their structure as shown in Fig. 6.12. We focus on two nanoparticle structures that are predicted to be the most stable based on the results of the previous sections. These are interfaces formed between the Au (111) facets of the nanoparticle and the ZnO(10$\bar{1}$0) and ZnO(11$\bar{2}$0) surfaces (Fig. 6.12). The dimensions of the supercells, number of Au atoms and number of ZnO atoms are summarised in Table 6.7. To prevent distortion of the ZnO slab during

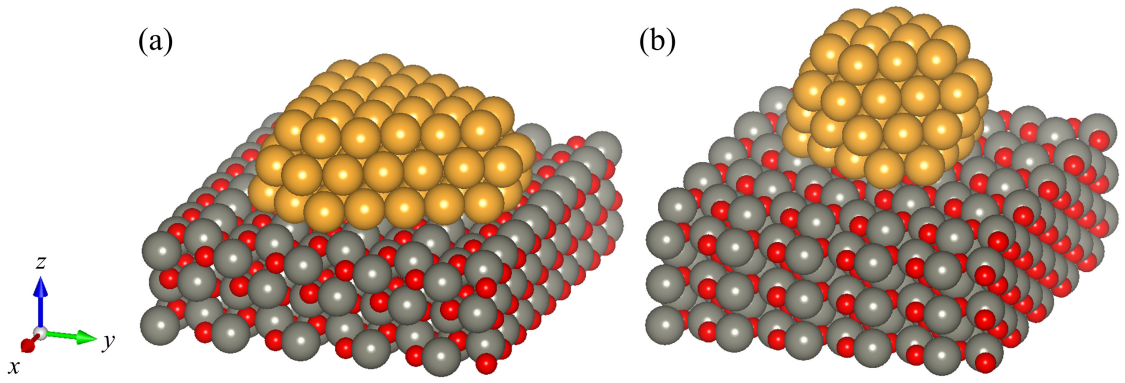

Figure 6.12: The atomic structures of Au nanoparticles supported on (a) ZnO($10\bar{1}0$) and (b) ZnO($11\bar{2}0$) surfaces. The gold, grey and red spheres represent the Au, Zn and O atoms, respectively.

	Au_{NP}/ZnO($10\bar{1}0$)	Au_{NP}/ZnO($11\bar{2}0$)
Size of supercell (Å^3)	28.75×25.30×23.00	27.66×25.30×30.00
Number of Au atoms	94	67
Number of ZnO atoms	540	600
Adhesion energy (J/m^2)	-1.16	-0.94
Average distance (Å)	2.29	2.42
Average lattice strain (%)	4.63	1.81
Charge transfer (e/nm^2)	0.81	0.79

Table 6.7: Calculated properties of ZnO supported Au nanoparticles.

geometry optimisation, the coordinates of the bottom layer of the ZnO slab is frozen (6 ZnO layers in total for both slabs). The initial geometry of the interfaces between Au nanoparticles and ZnO surfaces is such that Au atoms are directly located on top of the O atoms. Table 6.7 also summarises the calculated adhesion energy, average distance, lattice strain (in the interfacial Au layer) and charge transfer between the Au nanoparticle and ZnO supports. The calculation shows the adhesion energy and the average distance are reduced compared to the corresponding extended interfaces between Au and ZnO surfaces. The charge transfer is also twice larger than the slab systems. These above results indicate that the interaction between the Au and ZnO surfaces is enhanced for smaller nanoparticles which may be due to the reduced lattice strain of the interfacial Au atoms (reduced by 4.4 and 3.2 % for the ZnO ($10\bar{1}0$) and ($11\bar{2}0$) surfaces, respectively).

6.4.2 The formation of ZnO encapsulation

Experimental observations reported ZnO encapsulated Au nanoparticles can be produced by using the pretreatment in oxygen molecule stream at 500 K. In addition, the encapsulated Au nanoparticles provide higher catalytic activity for CO conversion. Since we found that the zinc interstitial can appear at the interface between Au and ZnO surfaces, we suggest that zinc atoms are the main source of the formation of ZnO encapsulation under oxygen-rich conditions. Fig. 6.13 (figure on the left) shows three possible sites for the zinc atom. Site A and B are the zinc interstitial at the interfaces between Au nanoparticles and ZnO support, respectively. The former zinc atom is in the middle of the interfaces and the latter is at the edge of the interfaces. Site C represents the zinc atom at the triple phase boundary out of the interfaces. In order to assess the stability of the zinc atom at different sites, we compare the total energy among sites A, B and C. The negative energy difference of $E_{\mathrm{B}} - E_{\mathrm{A}}$ (shown in right of Fig. 6.13) shows the zinc atom preferentially penetrates to the edge of the nanoparticles instead of the middle position. However, the 0.14 and 0.99 eV energies difference demonstrate the zinc atom is not able to locate at the triple phase boundary for either ZnO support. In other words the zinc atom at site C is unstable under oxygen-poor conditions. We next introduce an additional oxygen atom in the calculation to provide an oxygen-rich environment. In order to understand the formation of ZnO encapsulation, we use two systems to calculate the formation energy. The first system (figures on the top of Fig. 6.14) is the zinc atom located at the edge of the interfaces with a non-interacting oxygen atom, the total energy is expressed as $E_{\mathrm{Au_{NP}/ZnO}} + (1/2)E_{\mathrm{O_2}}$. The other system (figures on the bottom of Fig. 6.14) is the zinc atom at the triple phase boundary with an adsorbed oxygen atom (forming a ZnO molecule near the Au nanoparticle). The -2.1 and -1.2 eV formation energies shown in Fig. 6.14 indicate that the zinc atoms prefer to segregate to site C and form ZnO encapsulation around the nanoparticle. The bond length of the ZnO molecule is approximately 2.0 Å, which is consistent with the bond length of wurtzite ZnO. The result indicates that in the presence of zinc interstitials can lead to formation of ZnO near the edge of the Au nanoparticle leading to encapsulation.

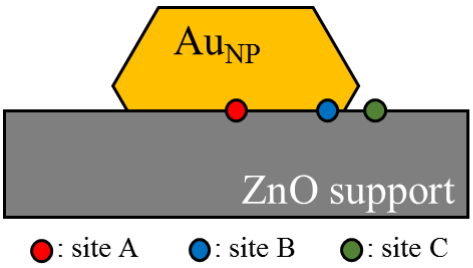

Supports	Energy difference (eV)	
	$E_B - E_A$	$E_C - E_B$
ZnO($10\bar{1}0$)	-1.66	0.14
ZnO($10\bar{1}0$)	-0.39	0.99

Figure 6.13: Figure on the left shows the different positions for the zinc atom and table on the right summaries the energy difference between the different zinc sites. The red, blue and green spheres represent the zinc location at the middle of the interfaces, the edge of the interfaces and the triple phase boundaries.

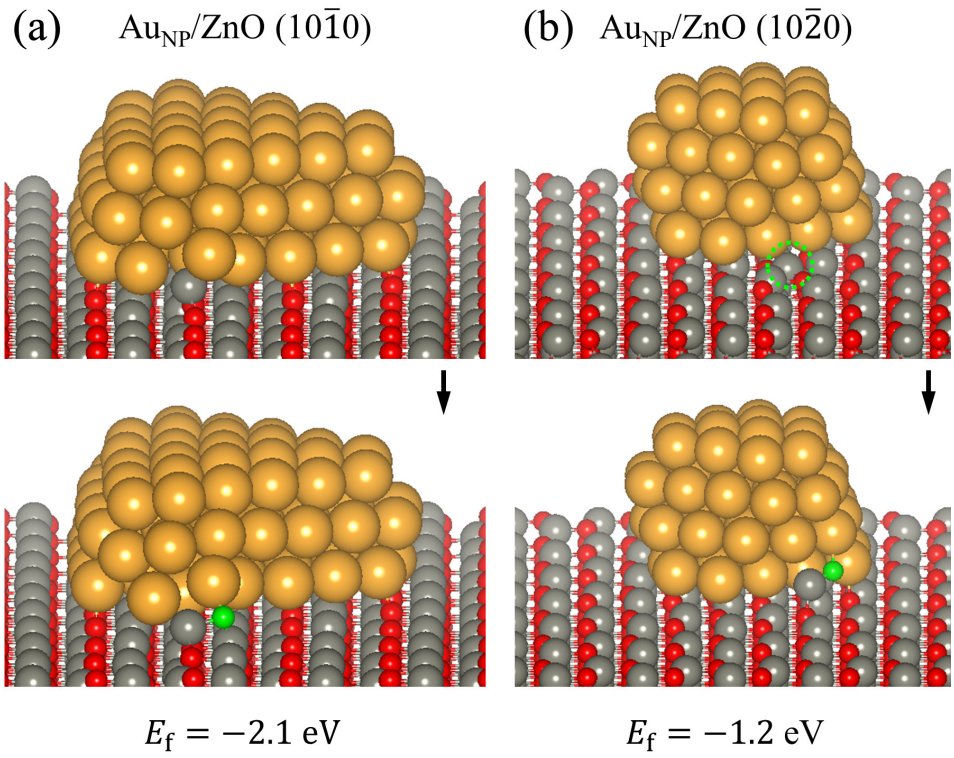

Figure 6.14: Atomic structure of formation of ZnO encapsulation on (a) ZnO ($10\bar{1}0$) and (b) ZnO ($11\bar{2}0$) surfaces and the formation energy of ZnO encapsulation. Figures on the top represent the zinc atom incorporating at the edge of the interfaces, while figures on the bottom show the formation of the ZnO encapsulation. The green-dashed circle indicates the unclear zinc atom at the interface between the Au nanoparticle and ZnO ($11\bar{2}0$) surface.

6.4.3 O_2 adsorption and CO oxidation reactivity

In order to understand how the ZnO encapsulation influences the CO oxidation reaction on Au nanoparticles supported on ZnO surfaces, we compute the reaction energy for different configurations of adsorbed oxygen. Many theoretical investigations indicate adsorption of CO on Au nanoparticles is energetically stable and the energy barrier of CO oxidation is about half an eV. Therefore in our modelling we do not include any explicit CO in the geometry optimisation [134, 144, 146, 198]. Instead, we use a simplified catalytic cycle on different adsorption sites to assess the possible reaction pathway:

$$\begin{aligned} \mathrm{O_{2(gas)}} &\rightarrow \mathrm{O_{2(ads)}} + E_{\mathrm{ads}}, \\ \mathrm{O_{2(ads)}} + \mathrm{CO_{(gas)}} + \Delta E_1 &\rightarrow \mathrm{O_{(ads)}} + \mathrm{CO_{2(gas)}}, \\ \mathrm{O_{(ads)}} + \mathrm{CO_{(gas)}} + \Delta E_2 &\rightarrow \mathrm{CO_{2(gas)}}. \end{aligned} \tag{6.8}$$

The first step is the adsorption of an oxygen molecule and the energy difference (E_{ads}) defines the stability of the oxygen adsorption. The second and third steps determine the reaction energies (ΔE_1 and ΔE_2) for two intermediate steps for CO oxidation. The shallow reaction energies potentially correspond to the larger energy barrier for catalytic reaction. Thus, the value of reaction energy indicates the difficulty of the CO oxidation reaction. In the calculation we first adsorb oxygen molecules at different sites (where each calculation only has one oxygen molecule present). After the geometry optimisation, we systematically remove one of the oxygen atoms. Finally, we calculate the adsorption energy and two reaction energies to understand the possible reaction pathways.

We consider several sites for oxygen molecule adsorption, the optimised structures for stable adsorption sites and their reaction energies are shown in Fig. 6.15 and Fig. 6.16. The former and latter figures are for the Au nanoparticles supported on ZnO $(10\bar{1}0)$ and $(11\bar{2}0)$ surfaces, respectively. The stable configurations of oxygen molecules fall into four types: (I) oxygen molecules adsorbed on top of Au atoms on (001) facets, (II) dissociative adsorption at bridge sites on the (001) facet, (III) oxygen molecule adsorption at the triple phase boundary forming bonds between Au atom and Zn atoms, and (IV) oxygen molecule adsorption at the zinc atom present due to the ZnO encapsulation (which also forms a bond with an Au atom). The bond lengths (l) shown in the figures only represent the specific atom pair, $l_{\mathrm{O-O}}$ is the distance between adsorbing oxygen atoms, $l_{\mathrm{O-Zn}}$ represents the distance between an adsorbing oxygen atom and the zinc atom and $l_{\mathrm{O-Au}}$

shows the bond length between an adsorbing oxygen atom and the adsorbed Au atom. In these calculations, the adsorbing oxygen molecule has a bond length of 1.3 Å, which is slightly larger than the 1.1 Å bond length of oxygen molecule in gas phase. In addition, oxygen atom adsorption on the bridge sites of the Au (001) facet is fully dissociative presenting an internal distance of 4.7 Å. The bond length between adsorbing oxygen atom and the adsorbed Au atom is in the range from 2.0 to 2.3 Å depending on the adsorption environment. The bond length between oxygen and the zinc atom in Fig. 6.15(c)-(d) and Fig. 6.16(b)-(c) is similar to the one of wurtzite ZnO. The adsorption energy shown in Fig. 6.15(e) and Fig. 6.16(d) demonstrates the adsorption with the zinc atom (also the ZnO encapsulation) provides better ability to capture the oxygen molecule due to the more stable potential energy. In addition, the reaction energy demonstrates the further oxidation process is energetically preferred. If we compare the second reaction energy between type III and IV of the Au nanoparticle supported on ZnO $(10\bar{1}0)$ surface, the latter reaction provide two times reaction energy than the former configuration. The larger reaction energy may provide a larger energy barrier for the CO oxidation and prohibit the cycle of the CO oxidation reaction. Therefore, we suggest that the zinc atom may form ZnO encapsulation first further promoting the catalytic reaction. Bader analysis shows the adsorbed Au atoms transfer 0.3 and 0.8 electron to the adsorbed oxygen molecule and dissociated oxygen atoms, respectively. The amount of the transferred charge is consistent with recent work presenting oxygen atoms adsorption on metallic nanoparticles [84]. The zinc atom (in type III and IV) transfers 1.0-1.2 electrons to the dissociatively adsorbed of oxygen atoms, giving a similar charge state to that of an oxygen atom in the bulk ZnO (-1.4 e). Meanwhile, the zinc atom and the Au atom transfer 0.7 and 0.6 electron to the molecular oxygen atoms.

In summary, the ZnO encapsulation is energetically stable under an oxygen-rich environment and the investigation suggests the zinc interstitial could form the ZnO encapsulation around Au nanoparticles. The calculations suggest ZnO encapsulation provides alternative sites for oxygen molecule adsorption and it enhances the catalytic performance for CO oxidation reaction due to increasing the number of reaction sites. This study provides an atomistic insight into the origin of enhanced CO conversion and shows a good agreement with the recent work demonstrating the reaction rate can be increased with increasing the density of the triple phase boundary [199].

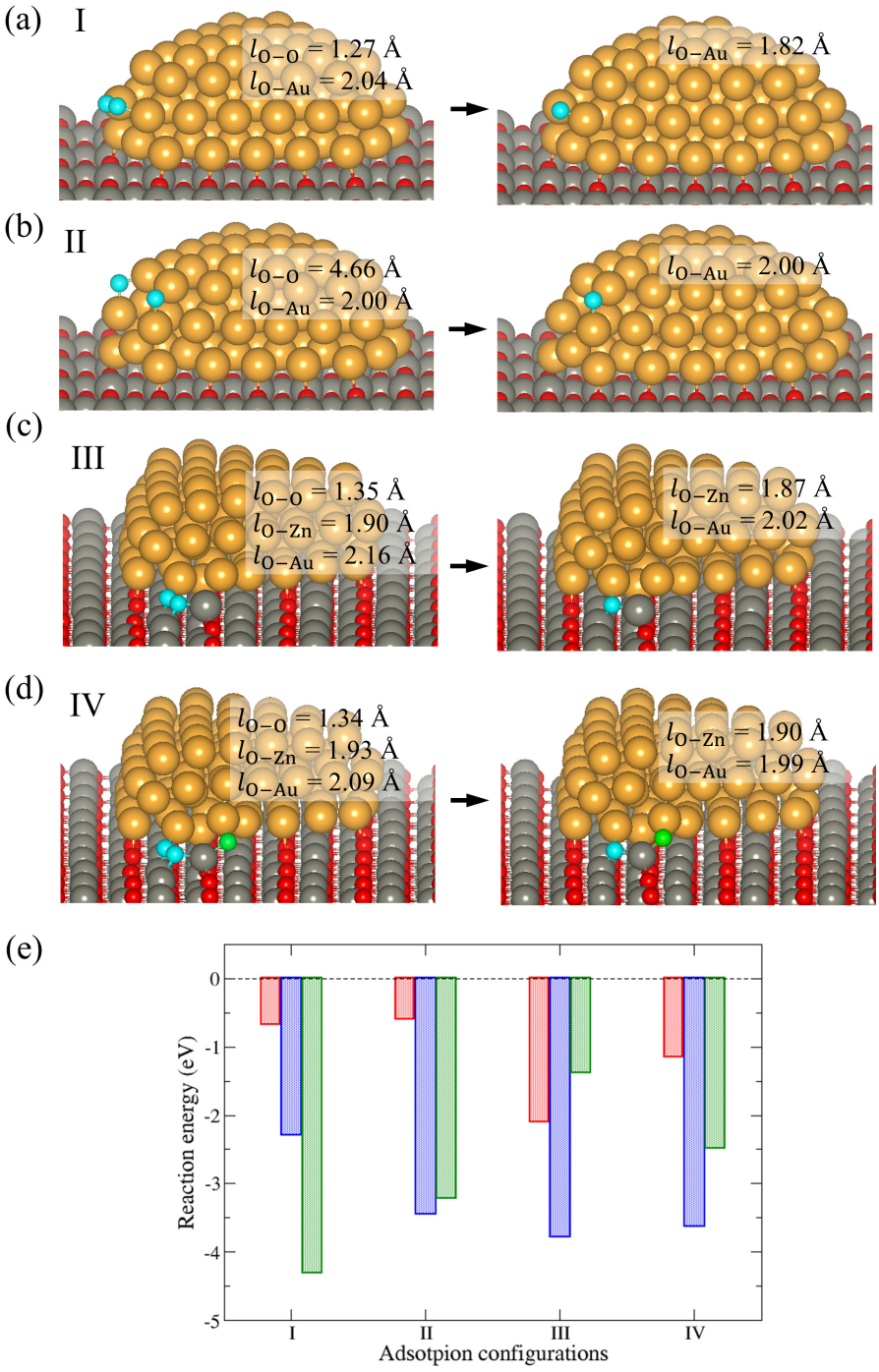

Figure 6.15: (a)-(d) Atomic structure of oxygen atoms (molecule) adsorbing on Au nanoparticles supported on ZnO $(10\bar{1}0)$ surfaces. (e) shows the reaction energies for oxygen adsorption and CO oxidation reactions. The green and blue spheres represent the oxygen atoms for adsorption and ZnO encapsulation respectively. The red, blue and green histograms represent the oxygen adsorption energy, first reaction energy and second reaction energy, respectively.

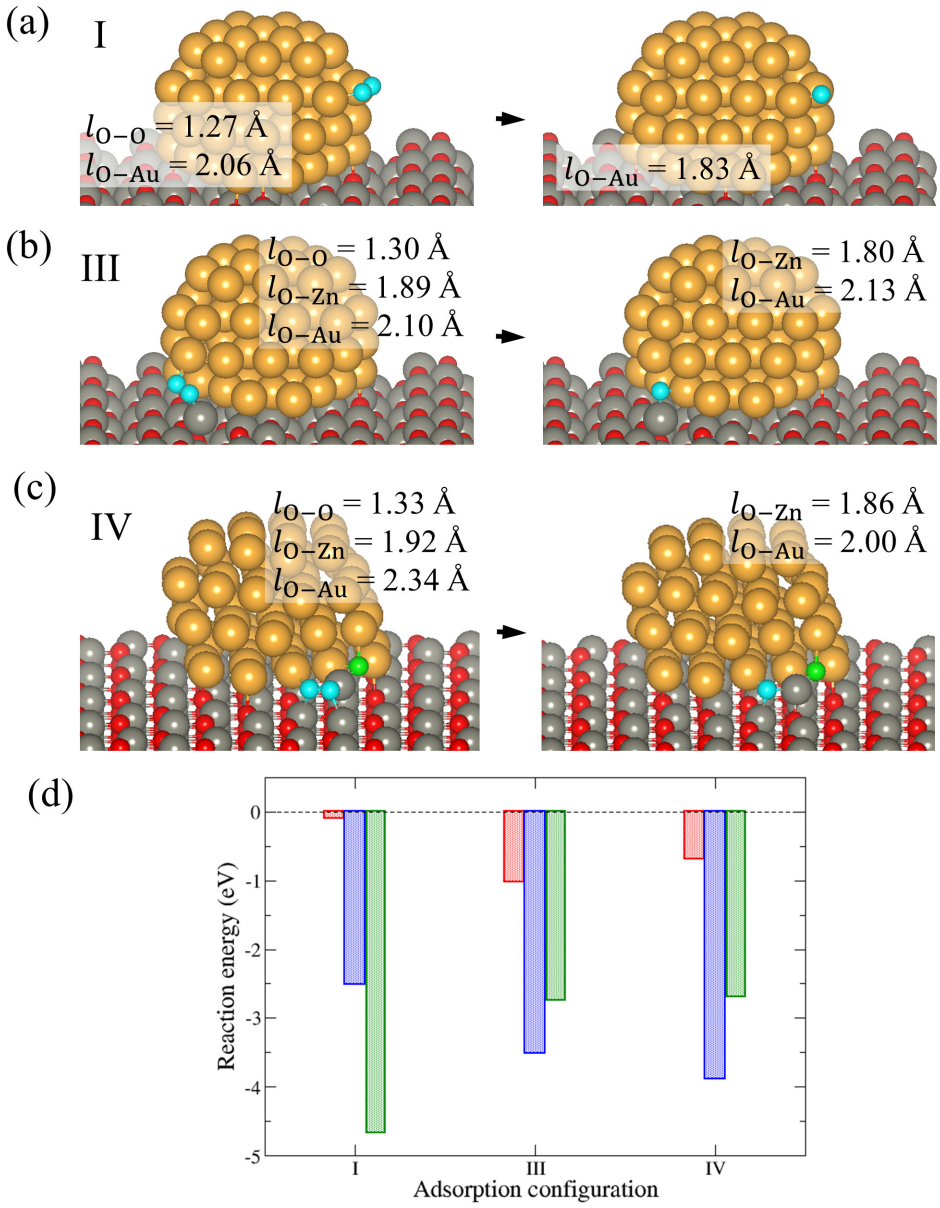

Figure 6.16: (a)-(c) Atomic structure of oxygen atoms (molecule) adsorbing on Au nanoparticles supported on ZnO $(11\bar{2}0)$ surfaces. (d) shows the reaction energies for oxygen adsorption and CO oxidation reactions. The green and blue spheres represent the oxygen atoms for adsorption and ZnO encapsulation respectively. The red, blue and green histograms represent the oxygen adsorption energy, first reaction energy and second reaction energy, respectively.

6.5 Discussion and Conclusions

Several factors may influence the accuracy of the results in this chapter. Firstly, the NLEP+U method is an empirical approach fitted to the experimental parameters (such as lattice constant and band gap). Although the formation enthalpy and surface formation energy of bulk ZnO are consistent with the experimental observation and hybrid calculation, we found the work functions of wurtzite ZnO and fcc Au predicted by the GGA+NLEP+U calculation is not in the correct order. The exact difference of work function between ZnO and Au should be 0.62 eV, but the calculated difference is -0.76 eV. Due to the non-linear correlation between work function and NLEP parameters, it is difficult to find parameters that describe all properties accurately. To make sure the work function does not significantly impact the results for the interface, we compared the calculated properties with the standard GGA functional. The standard GGA calculation shows good agreement with the GGA+NLEP+U method indicating the GGA+NLEP+U method is reliable. Although, the hybrid calculation may provide us more accurate result, the number of atoms in these systems means it is not computationally feasible.

The other main factor affecting accuracy is the limited number of oxygen adsorption configurations considered. Possible adsorption configurations are obtained by a systematic investigation, but the real situation may involve more varied modes of adsorption. Ab initio molecular dynamics (AIMD) simulation could be an alternative approach to model the adsorption to obtain more possible configurations, but the huge computational cost makes it unfeasible. In the calculation of CO oxidation reaction, we only involved the oxygen molecule in the optimisation rather than include CO molecule explicitly. The oxygen adsorption and dissociation may include many intermediate steps, such as oxygen molecule dissociation and oxygen atom diffusion. However, the precise dynamics of oxygen atoms during CO oxidation on Au nanoparticles supported on ZnO surface is beyond the scope of this work. Many recent works already provided many constructive results on the transition barriers for CO oxidation. Thus, it is not necessary to optimise all the structures with CO molecules included. Overall, the predictions carried out using the GGA+NLEP+U method are accurate enough and the configurations of atomic structures are representative to model the catalytic reaction of CO oxidation on the Au nanoparticles on ZnO nanorods.

In summary, we have investigated the morphology of Au nanoparticles using the formation energies of low-index Au surfaces and the adhesion energy of interfaces between Au and ZnO surfaces. The morphology of the free Au nanoparticle is truncated-octahedral, while the morphology of the supported Au nanoparticle demonstrates three different orientations along z-axis (including (001), (110) and (111)). The calculated adhesion energy demonstrates that the interface between Au (111) and ZnO $(10\bar{1}0)$ surfaces is the most energetically stable with $E_{\mathrm{ad}} = -0.8$ J/m^2. In addition, an increased in the concentration of oxygen vacancies at the interfaces of 1 nm^{-2} decreases the adhesion energy by around $0.3 - 0.4$ J/m^2. The zinc interstitial in ZnO is energetically stable and can lead to formation of ZnO encapsulation around the Au nanoparticles under oxygen-rich conditions. The reaction energy of CO oxidation shows that the ZnO encapsulation provides an alternative pathway for the CO oxidation reaction and the increased number of adsorption sites for oxygen molecules enhances the catalytic performance. Overall, this study provides atomistic insight into the formation of ZnO encapsulation due to zinc interstitial defects and the role it plays in the CO oxidation reaction.

Chapter 7

Conclusion

In summary, this thesis has investigated the modification of the structure and properties of metallic nanoparticles by their environment. In chapter 4, we studied granular $L1_0$ ordered FePt deposited on different $Mg_{(1-x)}Ti_xO$ substrates (x = 0.2, 0.4, 0.6, 0.8 and 1.0). The Ti-Fe bond formation at the interfaces was found to decrease the adhesion energy with increased substitutional TiO layers from -1.29 (pure MgO) to -2.35 J/m^2 (pure TiO). Bader analysis demonstrated that the charge transfers from TiO layers to the spin-down d-channel of interfacial Fe atoms, which reduces the magnetisation of the Fe atoms. In addition, the decreased adhesion energy hinders the growth of FePt nanoparticle along [001] direction. Although the incorporation of Ti atoms offers the MgTiO substrate electric conductivity, the decreased magnetisation introduces a lower coercivity for HAMR media. Our calculations suggests additional three layers of deposited MgO layers on the top of MgTiO substrates can passivate the Ti-Fe interaction.

In Chapter 5, we investigated a Ti nanoparticle and a bimetallic TiPt nanoparticle with different oxygen coverages. For Ti we showed that oxygen adsorbs to form linear O_{ads}-Ti-O_{ads} structures on the surface of Ti nanoparticle in order to minimise the adsorption energy. Increased oxygen coverages in the range of 13 to 100 % of coverage dilate the surface Ti-Ti bonds from 2 to 8 %. In addition, the expanded surface strain facilitates an oxygen atom penetration from surface to subsurface in the middle of the facets. 1 % of increased surface strain approximately decreases of 0.1 eV for the diffusion barrier. For TiPt we shows that the atomic arrangement of TiPt bimetallic nanoparticle (consisting

of 134 Ti and 13 Pt atoms) can be controlled by the degree of oxygen coverages. For 0.0 ML and 0.5 ML oxygen coverage, the nanoparticle is in the arrangement with Pt atoms at the vertices. The atomic configuration transforms into the triple and single Pt core(s) arrangements with 1.0 ML and 2.0 ML oxygen coverage, respectively. In free energy calculation, only the vertex and the single Pt core arrangements are thermodynamically stable. We suggest the multiple cores arrangement is not thermodynamically stable due to the lower degree of freedom of the $TiPt_{147}$ nanoparticle.

Finally, in Chapter 6 we used the GGA+NLEP+U method to study Au nanoparticles supported on ZnO supports and activity for CO oxidation. The results of the GGA+NLEP+U method for native point defect in ZnO show good arrangement with other works, such as hybrid calculations. The segregation energy shows that the zinc interstitial preferentially incorporates at the interface between Au and ZnO instead of bulk-like site. In addition, the zinc atom (interstitial) can lead to the formation of ZnO encapsulation near the Au nanoparticles under oxygen-rich conditions. We show oxygen molecules preferentially adsorb on the Au (001) facet and at the ZnO encapsulation layer. The calculated reaction energy for CO oxidation indicates the ZnO encapsulation layer provides an alternative reaction pathway with comparable catalytic ability compared to original Au_{NP}/ZnO.

The investigations in this thesis show how computational calculations can be used to model modification of nanoparticles by adsorbed molecules or supports providing deeper insight into atomistic processes. These predictions are consistent with experimental observations where available. However, some of the theoretical predictions await further experimental studies. We hope this thesis can inspire other people developing new projects to find more knowledge for materials science.

Bibliography

[1] M. Grätzel, "Photoelectrochemical cells," *Nature*, vol. 414, no. 6861, p. 338, 2001.

[2] G. Shen, Y. Chen, and C. Lin, "Corrosion protection of 316 L stainless steel by a TiO_2 nanoparticle coating prepared by sol–gel method," *Thin Solid Films*, vol. 489, no. 1-2, pp. 130–136, 2005.

[3] J. C. Hulteen, C. J. Patrissi, D. L. Miner, E. R. Crosthwait, E. B. Oberhauser, and C. R. Martin, "Changes in the shape and optical properties of gold nanoparticles contained within alumina membranes due to low-temperature annealing," *J. Phys. Chem. B*, vol. 101, no. 39, pp. 7727–7731, 1997.

[4] F. Baletto and R. Ferrando, "Structural properties of nanoclusters: Energetic, thermodynamic, and kinetic effects," *Rev. Mod. Phys.*, vol. 77, pp. 371–423, 2005.

[5] J. Yang, V. Frøseth, D. Chen, and A. Holmen, "Particle size effect for cobalt fischer–tropsch catalysts based on in situ co chemisorption," *Surf. Sci.*, vol. 648, pp. 67–73, 2016.

[6] I. Lee, M. A. Albiter, Q. Zhang, J. Ge, Y. Yin, and F. Zaera, "New nanostructured heterogeneous catalysts with increased selectivity and stability," *Phys. Chem. Chem. Phys.*, vol. 13, no. 7, pp. 2449–2456, 2011.

[7] J. Y. Park, Y. Zhang, S. H. Joo, Y. Jung, and G. A. Somorjai, "Size effect of rhpt bimetallic nanoparticles in catalytic activity of CO oxidation: Role of surface segregation," *Catal. Today*, vol. 181, no. 1, pp. 133–137, 2012.

[8] P. Geysermans, F. Finocchi, J. Goniakowski, R. Hacquart, and J. Jupille, "Combination of (100), (110) and (111) facets in MgO crystals shapes from dry to wet environment," *Phys. Chem. Chem. Phys.*, vol. 11, no. 13, pp. 2228–2233, 2009.

[9] Y. Zhou, Y. Zhu, Z.-Q. Wang, S. Zou, G. Ma, M. Xia, X. Kong, L. Xiao, X.-Q. Gong, and J. Fan, "Catalytic activity control via crossover between two different microstructures," *J. Am. Chem. Soc.*, vol. 139, no. 39, pp. 13740–13748, 2017.

[10] D. Weller and A. Moser, "Thermal effect limits in ultrahigh-density magnetic recording," *IEEE T. Magn.*, vol. 35, no. 6, pp. 4423–4439, 1999.

[11] S. Iwasaki and K. Ouchi, "Co-Cr recording films with perpendicular magnetic anisotropy," *IEEE T. Magn.*, vol. 14, no. 5, pp. 849–851, 1978.

[12] T. Klemmer, D. Hoydick, H. Okumura, B. Zhang, and W. Soffa, "Magnetic hardening and coercivity mechanisms in $L1_0$ ordered FePd ferromagnets," *Scripta Metall. Mater.*, vol. 33, no. 10-11, pp. 1793–1805, 1995.

[13] K. Barmak, J. Kim, L. Lewis, K. Coffey, M. Toney, A. Kellock, and J.-U. Thiele, "On the relationship of magnetocrystalline anisotropy and stoichiometry in epitaxial $L1_0$ CoPt (001) and FePt (001) thin films," *J. Appl. Phys.*, vol. 98, no. 3, p. 033904, 2005.

[14] O. Ivanov, "Determination of the anisotropy constant and saturation magnetization, and magnetic properties of powders of an iron-platinum alloy," *Phys. Met. Metallogr.*, vol. 35, no. 1, pp. 81–85, 1973.

[15] H. Li, K. Dong, J. Hu, T. Zhou, G. Chow, and J. Chen, "Lattice relaxation and its impact on magnetic properties of FePt thin film," *J. Phys. D Appl. Phys.*, vol. 46, no. 1, p. 015002, 2012.

[16] O. Gutfleisch, J. Lyubina, K.-H. Müller, and L. Schultz, "FePt hard magnets," *Adv. Eng. Mater.*, vol. 7, no. 4, pp. 208–212, 2005.

[17] R. Ristau, K. Barmak, L. Lewis, K. Coffey, and J. Howard, "On the relationship of high coercivity and $L1_0$ ordered phase in CoPt and FePt thin films," *J. Appl. Phys.*, vol. 86, no. 8, pp. 4527–4533, 1999.

[18] R. D. Rutledge, W. H. Morris, M. S. Wellons, Z. Gai, J. Shen, J. Bentley, J. E. Wittig, and C. M. Lukehart, "Formation of FePt nanoparticles having high coercivity," *J. Am. Chem. Soc.*, vol. 128, no. 44, pp. 14210–14211, 2006.

[19] A. Schleife, F. Fuchs, J. Furthmüller, and F. Bechstedt, "First-principles study of ground- and excited-state properties of MgO, ZnO, and CdO polymorphs," *Phys. Rev. B*, vol. 73, p. 245212, 2006.

[20] S. Heo, E. Cho, H.-I. Lee, G. S. Park, H. J. Kang, T. Nagatomi, P. Choi, and B.-D. Choi, "Band gap and defect states of MgO thin films investigated using reflection electron energy loss spectroscopy," *AIP Adv.*, vol. 5, no. 7, p. 077167, 2015.

[21] O. Taurian, M. Springborg, and N. Christensen, "Self-consistent electronic structures of MgO and SrO," *Solid State Commun.*, vol. 55, no. 4, pp. 351–355, 1985.

[22] J. Wang, S. Hata, Y. Takahashi, H. Sepehri-Amin, B. C. S. Varaprasad, T. Shiroyama, T. Schrefl, and K. Hono, "Effect of MgO underlayer misorientation on the texture and magnetic property of FePt–C granular film," *Acta Mater.*, vol. 91, pp. 41–49, 2015.

[23] J. J. Bean, M. Saito, S. Fukami, H. Sato, S. Ikeda, H. Ohno, Y. Ikuhara, and K. P. McKenna, "Atomic structure and electronic properties of MgO grain boundaries in tunnelling magnetoresistive devices," *Sci. Rep.*, vol. 7, p. 45594, 2017.

[24] T. Shima, K. Takanashi, Y. Takahashi, and K. Hono, "Preparation and magnetic properties of highly coercive FePt films," *Appl. Phys. Lett.*, vol. 81, no. 6, pp. 1050–1052, 2002.

[25] R. E. Rottmayer, S. Batra, D. Buechel, W. A. Challener, J. Hohlfeld, Y. Kubota, L. Li, B. Lu, C. Mihalcea, K. Mountfield, *et al.*, "Heat-assisted magnetic recording," *IEEE T. Magn.*, vol. 42, no. 10, pp. 2417–2421, 2006.

[26] L. Zhang, Y. Takahashi, A. Perumal, and K. Hono, "$L1_0$-ordered high coercivity (FePt) Ag–C granular thin films for perpendicular recording," *J. Magn. Magn. Mater.*, vol. 322, no. 18, pp. 2658–2664, 2010.

[27] K. Dong, H. Li, Y. Peng, G. Ju, G. Chow, and J. Chen, "Nanogranular TiN-ZrO_2 intermediate layer induced improvement of isolation and grain size of FePt thin films," *Sci. Rep.*, vol. 4, p. 5607, 2014.

[28] T. Seki, Y. Takahashi, and K. Hono, "Microstructure and magnetic properties of FePt-SiO_2 granular films with Ag addition," *J. Appl. Phys.*, vol. 103, no. 2, p. 023910, 2008.

[29] A. Perumal, Y. K. Takahashi, and K. Hono, "$L1_0$ FePt–C nanogranular perpendicular anisotropy films with narrow size distribution," *Appl. Phys. Express*, vol. 1, no. 10, p. 101301, 2008.

[30] A. Perumal, Y. Takahashi, and K. Hono, "FePt-C nanogranular films for perpendicular magnetic recording," *J. Appl. Phys.*, vol. 105, no. 7, p. 07B732, 2009.

[31] C. Platt, K. Wierman, E. Svedberg, R. Van de Veerdonk, J. Howard, A. Roy, and D. Laughlin, "$L1_0$ ordering and microstructure of FePt thin films with Cu, Ag, and Au additive," *J. Appl. Phys.*, vol. 92, no. 10, pp. 6104–6109, 2002.

[32] B. C. S. Varaprasad, Y. Takahashi, J. Wang, T. Ina, T. Nakamura, W. Ueno, K. Nitta, T. Uruga, and K. Hono, "Mechanism of coercivity enhancement by Ag addition in FePt-C granular films for heat assisted magnetic recording media," *Appl. Phys. Lett.*, vol. 104, no. 22, p. 222403, 2014.

[33] L. Zhang, Y. Takahashi, K. Hono, B. Stipe, J.-Y. Juang, and M. Grobis, "$L1_0$-ordered FePtAg–C granular thin film for thermally assisted magnetic recording media," *J. Appl. Phys.*, vol. 109, no. 7, p. 07B703, 2011.

[34] J. Wang, Y. Takahashi, H. S. Amin, and K. Hono, "Origin of in-plane component for $L1_0$-FePt granular films deposited on MgO single crystal substrate," in *2017 IEEE International Magnetics Conference (INTERMAG)*, pp. 1–2, IEEE, 2017.

[35] W. Zhu, H.-C. Ding, S.-J. Gong, Y. Liu, and C.-G. Duan, "First-principles studies of the magnetic anisotropy of the Cu/FePt/MgO system," *J. Phys. Condens. Mat.*, vol. 25, no. 39, p. 396001, 2013.

[36] R. Cuadrado and R. W. Chantrell, "Interface magnetic moments enhancement of FePt-$L1_0$/MgO(001): An ab initio study," *Phys. Rev. B*, vol. 89, p. 094407, 2014.

[37] R. Cuadrado and R. W. Chantrell, "Interaction potential of FePt with the MgO(001) surface," *Phys. Rev. B*, vol. 91, p. 075420, 2015.

[38] B. C. S. Varaprasad, Y. Takahashi, A. Ajan, and K. Hono, "Electrically conductive $(Mg_{0.2}Ti_{0.8})O$ underlayer to grow FePt-based perpendicular recording media on glass substrates," *J. Appl. Phys.*, vol. 113, no. 20, p. 203907, 2013.

[39] J. K. Burdett and T. Hughbanks, "Niobium oxide (NbO) and titanium oxide (TiO): a study of the structural and electronic stability of structures derived from rock salt," *J. Am. Chem. Soc.*, vol. 106, no. 11, pp. 3101–3113, 1984.

[40] D. Watanabe, J. Castles, A. Jostsons, and A. Malin, "The ordered structure of TiO," *Acta Crystallogr.*, vol. 23, no. 2, pp. 307–313, 1967.

[41] F. J. Morin, "Oxides which show a metal-to-insulator transition at the Neel temperature," *Phys. Rev. Lett.*, vol. 3, pp. 34–36, 1959.

[42] A. Dannenberg, M. E. Gruner, A. Hucht, and P. Entel, "Surface energies of stoichiometric FePt and CoPt alloys and their implications for nanoparticle morphologies," *Phys. Rev. B*, vol. 80, p. 245438, 2009.

[43] M. Müller, P. Erhart, and K. Albe, "Thermodynamics of $L1_0$ ordering in FePt nanoparticles studied by Monte Carlo simulations based on an analytic bond-order potential," *Phys. Rev. B*, vol. 76, p. 155412, 2007.

[44] B. Yang, M. Asta, O. Mryasov, T. Klemmer, and R. Chantrell, "Equilibrium Monte Carlo simulations of $A1$–$L1_0$ ordering in FePt nanoparticles," *Scripta Mater.*, vol. 53, no. 4, pp. 417–422, 2005.

[45] N. Poudyal, G. S. Chaubey, C.-b. Rong, and J. P. Liu, "Shape control of FePt nanocrystals," *J. Appl. Phys.*, vol. 105, no. 7, p. 07A749, 2009.

[46] M. Fichtner, O. Fuhr, O. Kircher, and J. Rothe, "Small Ti clusters for catalysis of hydrogen exchange in $NaAlH_4$," *Nanotechnology*, vol. 14, no. 7, p. 778, 2003.

[47] H. Chang and Y.-C. Hsu, "Fabrication and material properties of NiTi nanofluid," *J. Vac. Sci. Technol. B*, vol. 25, no. 3, pp. 935–939, 2007.

[48] P. C. Jennings, B. G. Pollet, and R. L. Johnston, "Theoretical studies of Pt–Ti nanoparticles for potential use as pemfc electrocatalysts," *Phys. Chem. Chem. Phys.*, vol. 14, no. 9, pp. 3134–3139, 2012.

[49] T. Schalow, M. Laurin, B. Brandt, S. Schauermann, S. Guimond, H. Kuhlenbeck, D. E. Starr, S. K. Shaikhutdinov, J. Libuda, and H.-J. Freund, "Oxygen storage at the metal/oxide interface of catalyst nanoparticles," *Angew. Chem. Int. Edit.*, vol. 44, no. 46, pp. 7601–7605, 2005.

[50] C.-N. Lok, C.-M. Ho, R. Chen, Q.-Y. He, W.-Y. Yu, H. Sun, P. K.-H. Tam, J.-F. Chiu, and C.-M. Che, "Silver nanoparticles: partial oxidation and antibacterial activities," *J. Biol. Inorg. Chem.*, vol. 12, no. 4, pp. 527–534, 2007.

[51] T. Reier, M. Oezaslan, and P. Strasser, "Electrocatalytic oxygen evolution reaction (OER) on Ru, Ir, and Pt catalysts: a comparative study of nanoparticles and bulk materials," *Acs Catal.*, vol. 2, no. 8, pp. 1765–1772, 2012.

[52] L. Lian, C.-X. Su, and P. B. Armentrout, "Collision-induced dissociation of Ti^+ n (n= 2–22) with Xe: Bond energies, geometric structures, and dissociation pathways," *J. Chem. Phys.*, vol. 97, no. 6, pp. 4084–4093, 1992.

[53] S.-R. Liu, H.-J. Zhai, M. Castro, and L.-S. Wang, "Photoelectron spectroscopy of Ti n-clusters (n= 1–130)," *J. Chem. Phys.*, vol. 118, no. 5, pp. 2108–2115, 2003.

[54] M. Castro, S.-R. Liu, H.-J. Zhai, and L.-S. Wang, "Structural and electronic properties of small titanium clusters: A density functional theory and anion photoelectron spectroscopy study," *J. Chem. Phys.*, vol. 118, no. 5, pp. 2116–2123, 2003.

[55] S.-Y. Wang, W. Duan, D.-L. Zhao, and C.-Y. Wang, "First-principles study of the stability of the icosahedral ti_{13}, ti_{13}^{-1}, and ti_{13}^{+1} clusters," *Phys. Rev. B*, vol. 65, p. 165424, 2002.

[56] S.-Y. Wang, J.-Z. Yu, H. Mizuseki, J.-A. Yan, Y. Kawazoe, and C.-Y. Wang, "First-principles study of the electronic structures of icosahedral Ti n (n= 13, 19, 43, 55) clusters," *J. Chem. Phys.*, vol. 120, no. 18, pp. 8463–8468, 2004.

[57] M. Salazar-Villanueva, P. H. Hernández Tejeda, U. Pal, J. F. Rivas-Silva, J. I. Rodríguez Mora, and J. A. Ascencio, "Stable Ti_n (n= 2- 15) clusters and their geometries: DFT calculations," *J. Phys. Chem. A*, vol. 110, no. 34, pp. 10274–10278, 2006.

[58] C. L. Cleveland and U. Landman, "The energetics and structure of nickel clusters: Size dependence," *J. Chem. Phys.*, vol. 94, no. 11, pp. 7376–7396, 1991.

[59] J. L. Elechiguerra, J. Reyes-Gasga, and M. J. Yacaman, "The role of twinning in shape evolution of anisotropic noble metal nanostructures," *J. Mater. Chem.*, vol. 16, no. 40, pp. 3906–3919, 2006.

[60] W. Zhang, Y. Liu, R. Cao, Z. Li, Y. Zhang, Y. Tang, and K. Fan, "Synergy between crystal strain and surface energy in morphological evolution of five-fold-twinned silver crystals," *J. Am. Chem. Soc.*, vol. 130, no. 46, pp. 15581–15588, 2008.

[61] J. Hu, L. Wu, K. A. Kuttiyiel, K. R. Goodman, C. Zhang, Y. Zhu, M. B. Vukmirovic, M. G. White, K. Sasaki, and R. R. Adzic, "Increasing stability and activity of core–shell catalysts by preferential segregation of oxide on edges and vertexes: Oxygen reduction on Ti–Au@Pt/C," *J. Am. Chem. Soc.*, vol. 138, no. 29, pp. 9294–9300, 2016.

[62] S. Patala, L. D. Marks, and M. Olvera de la Cruz, "Elastic strain energy effects in faceted decahedral nanoparticles," *J. Phys. Chem. C*, vol. 117, no. 3, pp. 1485–1494, 2013.

[63] P. Kofstad, P. Anderson, and O. Krudtaa, "Oxidation of titanium in the temperature range 800–1200 C," *J. Less Common Met.*, vol. 3, no. 2, pp. 89–97, 1961.

[64] J. Liu, X. Fan, C. Sun, and W. Zhu, "Oxidation of the titanium (0001) surface: diffusion processes of oxygen from DFT," *RSC Adv.*, vol. 6, no. 75, pp. 71311–71318, 2016.

[65] B. T. Jonker, J. F. Morar, and R. L. Park, "Surface states and oxygen chemisorption on Ti(0001)," *Phys. Rev. B*, vol. 24, pp. 2951–2957, 1981.

[66] H. Shih, F. Jona, D. Jepsen, and P. Marcus, "Leed structure analysis of a $p(2\times2)$ chemisorbed layer of CO on Ti(0001)," *J. Vac. Sci. Technol.*, vol. 15, no. 2, pp. 596–599, 1978.

[67] A. Hagsteöm, A. Platau, and S.-E. Kaelsson, "Adsorption of oxygen at room temperature on polycrystalline titanium studied by ultraviolet and X-ray photoelectron spectroscopy," *Phys. Status Solidi B*, vol. 83, no. 1, pp. 77–84, 1977.

[68] D. M. Hanson, R. Stockbauer, and T. E. Madey, "Photon-stimulated desorption and other spectroscopic studies of the interaction of oxygen with a titanium (001) surface," *Phys. Rev. B*, vol. 24, pp. 5513–5521, 1981.

[69] A. F. Carley, P. R. Chalker, J. C. Riviere, and M. W. Roberts, "The identification and characterisation of mixed oxidation states at oxidised titanium surfaces by

analysis of X-ray photoelectron spectra," *J. Chem. Soc. Farad. T. 1*, vol. 83, no. 2, pp. 351–370, 1987.

[70] I. Vaquila, M. C. G. Passeggi, and J. Ferrón, "Oxidation process in titanium thin films," *Phys. Rev. B*, vol. 55, pp. 13925–13931, 1997.

[71] G. Lu, S. L. Bernasek, and J. Schwartz, "Oxidation of a polycrystalline titanium surface by oxygen and water," *Surf. Sci.*, vol. 458, no. 1-3, pp. 80–90, 2000.

[72] I. Vaquila, M. Passeggi Jr, and J. Ferron, "Temperature effects in the early stages of titanium oxidation," *Appl. Surf. Sci.*, vol. 93, no. 3, pp. 247–253, 1996.

[73] J. Bignolas, M. Bujor, and J. Bardolle, "A study of the early stages of the kinetics of titanium oxidation by auger electron spectroscopy and mirror electron microscopy," *Surf. Sci. Lett.*, vol. 108, no. 2, pp. L453–L459, 1981.

[74] M. Martin, W. Mader, and E. Fromm, "Oxidation of iron, aluminium and titanium films in the temperature range 50–200 C," *Thin Solid Films*, vol. 250, no. 1-2, pp. 61–66, 1994.

[75] Y. Takakuwa, S. Ishidzuka, A. Yoshigoe, Y. Teraoka, Y. Yamauchi, Y. Mizuno, H. Tonda, and T. Homma, "Real-time monitoring of oxidation on the Ti(0001) surface by synchrotron radiation photoelectron spectroscopy and RHEED–AES," *Appl. Surf. Sci.*, vol. 216, no. 1-4, pp. 395–401, 2003.

[76] H. H. Wu and D. R. Trinkle, "Direct diffusion through interpenetrating networks: Oxygen in titanium," *Phys. Rev. Lett.*, vol. 107, p. 045504, 2011.

[77] G. Boureau, N. Capron, and R. Tétot, "A first-principles study of dilute solutions of oxygen in titanium," *Scripta Mater.*, vol. 59, no. 12, pp. 1255–1258, 2008.

[78] A. Chibisov, "Oxygen adsorption on small Ti clusters: A first-principles study," *Comp. Mater. Sci.*, vol. 82, pp. 131–133, 2014.

[79] Z. Liu, L. Ma, J. Zhang, K. Hongsirikarn, and J. G. Goodwin Jr, "Pt alloy electrocatalysts for proton exchange membrane fuel cells: A review," *Catal. Rev.*, vol. 55, no. 3, pp. 255–288, 2013.

[80] S. Kattel, Z. Duan, and G. Wang, "Density functional theory study of an oxygen reduction reaction on a Pt_3Ti alloy electrocatalyst," *J. Phys. Chem. C*, vol. 117, no. 14, pp. 7107–7113, 2013.

[81] E. Ding, K. L. More, and T. He, "Preparation and characterization of carbon-supported PtTi alloy electrocatalysts," *J. Power Sources*, vol. 175, no. 2, pp. 794–799, 2008.

[82] Y. Shao-Horn, W. Sheng, S. Chen, P. Ferreira, E. Holby, and D. Morgan, "Instability of supported platinum nanoparticles in low-temperature fuel cells," *Top. Catal.*, vol. 46, no. 3-4, pp. 285–305, 2007.

[83] T. Ioroi, T. Akita, M. Asahi, S.-i. Yamazaki, Z. Siroma, N. Fujiwara, and K. Yasuda, "Platinum–titanium alloy catalysts on a magnéli-phase titanium oxide support for improved durability in polymer electrolyte fuel cells," *J. Power Sources*, vol. 223, pp. 183–189, 2013.

[84] A. Mahata, P. Bhauriyal, K. S. Rawat, and B. Pathak, "Pt_3Ti (Ti_{19}@Pt_{60})-based cuboctahedral core–shell nanocluster favors a direct over indirect oxygen reduction reaction," *ACS Energy Lett.*, vol. 1, no. 4, pp. 797–805, 2016.

[85] C. Xirouchaki and R. Palmer, "Deposition of size-selected metal clusters generated by magnetron sputtering and gas condensation: a progress review," *Philos. T. R. Soc. Lond. A Math. Phys. Eng. Sci.*, vol. 362, no. 1814, pp. 117–124, 2004.

[86] C. E. Blackmore, N. V. Rees, and R. E. Palmer, "Modular construction of size-selected multiple-core Pt–TiO_2 nanoclusters for electro-catalysis," *Phys. Chem. Chem. Phys.*, vol. 17, no. 42, pp. 28005–28009, 2015.

[87] T.-W. Liao, A. Yadav, K.-J. Hu, J. van der Tol, S. Cosentino, F. D'Acapito, R. E. Palmer, C. Lenardi, R. Ferrando, D. Grandjean, *et al.*, "Unravelling the nucleation mechanism of bimetallic nanoparticles with composition-tunable core–shell arrangement," *Nanoscale*, vol. 10, no. 14, pp. 6684–6694, 2018.

[88] P. Schabes-Retchkiman, G. Canizal, R. Herrera-Becerra, C. Zorrilla, H. Liu, and J. Ascencio, "Biosynthesis and characterization of Ti/Ni bimetallic nanoparticles," *Opt. Mater.*, vol. 29, no. 1, pp. 95–99, 2006.

[89] E. Lewis, T. Slater, E. Prestat, A. Macedo, P. O'Brien, P. Camargo, and S. Haigh, "Real-time imaging and elemental mapping of AgAu nanoparticle transformations," *Nanoscale*, vol. 6, no. 22, pp. 13598–13605, 2014.

[90] H. Liu, G. Canizal, P. Schabes-Retchkiman, and J. Ascencio, "Structural selection and amorphization of small Ni-Ti bimetallic clusters," *J. Phys. Chem. B*, vol. 110, no. 25, pp. 12333–12339, 2006.

[91] P. O. Sharma, M. A. Abraham, and S. Chattopadhyay, "Development of a novel metal monolith catalyst for natural gas steam reforming," *Ind. Eng. Chem. Res.*, vol. 46, no. 26, pp. 9053–9060, 2007.

[92] E. Castillejos, R. Bacsa, A. Guerrero-Ruiz, I. Rodríguez-Ramos, L. Datas, and P. Serp, "Catalytic activity of gold supported on ZnO tetrapods for the preferential oxidation of carbon monoxide under hydrogen rich conditions," *Nanoscale*, vol. 3, no. 3, pp. 929–932, 2011.

[93] N. E. Singh-Miller and N. Marzari, "Surface energies, work functions, and surface relaxations of low-index metallic surfaces from first principles," *Phys. Rev. B*, vol. 80, p. 235407, 2009.

[94] M. Benoit, C. Langlois, N. Combe, H. Tang, and M.-J. Casanove, "Structural and electronic properties of the Au(001)/Fe(001) interface from density functional theory calculations," *Phys. Rev. B*, vol. 86, p. 075460, 2012.

[95] Ž. Crljen, P. Lazić, D. Šokčević, and R. Brako, "Relaxation and reconstruction on (111) surfaces of Au, Pt, and Cu," *Phys. Rev. B*, vol. 68, p. 195411, 2003.

[96] A. S. Barnard, X. Lin, and L. A. Curtiss, "Equilibrium morphology of face-centered cubic gold nanoparticles > 3 nm and the shape changes induced by temperature," *J. Phys. Chem. B*, vol. 109, no. 51, pp. 24465–24472, 2005.

[97] Q. Li, D. Yin, J. Li, and F. L. Deepak, "Atomic-scale understanding of gold cluster growth on different substrates and adsorption-induced structural change," *J. Phys. Chem. C*, vol. 122, no. 3, pp. 1753–1760, 2018.

[98] W. Zhan, Y. Shu, Y. Sheng, H. Zhu, Y. Guo, L. Wang, Y. Guo, J. Zhang, G. Lu, and S. Dai, "Surfactant-assisted stabilization of Au colloids on solids for heterogeneous catalysis," *Angew. Chem.*, vol. 129, no. 16, pp. 4565–4569, 2017.

[99] S. Tauster, "Strong metal-support interactions," *Accounts Chem. Res.*, vol. 20, no. 11, pp. 389–394, 1987.

[100] C.-J. Pan, M.-C. Tsai, W.-N. Su, J. Rick, N. G. Akalework, A. K. Agegnehu, S.-Y. Cheng, and B.-J. Hwang, "Tuning/exploiting strong metal-support interaction (SMSI) in heterogeneous catalysis," *J. Taiwan Inst. Chem. Eng.*, vol. 74, pp. 154–186, 2017.

[101] X. Liu, M.-H. Liu, Y.-C. Luo, C.-Y. Mou, S. D. Lin, H. Cheng, J.-M. Chen, J.-F. Lee, and T.-S. Lin, "Strong metal–support interactions between gold nanoparticles and ZnO nanorods in CO oxidation," *J. Am. Chem. Soc.*, vol. 134, no. 24, pp. 10251–10258, 2012.

[102] R. Das, A. Kumar, Y. Kumar, S. Sen, and P. M. Shirage, "Effect of growth temperature on the optical properties of ZnO nanostructures grown by simple hydrothermal method," *RSC Adv.*, vol. 5, no. 74, pp. 60365–60372, 2015.

[103] P. Erhart, A. Klein, and K. Albe, "First-principles study of the structure and stability of oxygen defects in zinc oxide," *Phys. Rev. B*, vol. 72, p. 085213, 2005.

[104] R. G. S. Pala and H. Metiu, "Modification of the oxidative power of ZnO $(10\bar{1}0)$ surface by substituting some surface Zn atoms with other metals," *J. Phys. Chem. C*, vol. 111, no. 24, pp. 8617–8622, 2007.

[105] B. Meyer and D. Marx, "Density-functional study of the structure and stability of ZnO surfaces," *Phys. Rev. B*, vol. 67, p. 035403, 2003.

[106] A. Janotti and C. G. Van de Walle, "Native point defects in ZnO," *Phys. Rev. B*, vol. 76, p. 165202, 2007.

[107] P. Erhart, K. Albe, and A. Klein, "First-principles study of intrinsic point defects in ZnO: Role of band structure, volume relaxation, and finite-size effects," *Phys. Rev. B*, vol. 73, p. 205203, 2006.

[108] S. Lany, H. Raebiger, and A. Zunger, "Magnetic interactions of Cr−Cr and Co−Co impurity pairs in ZnO within a band-gap corrected density functional approach," *Phys. Rev. B*, vol. 77, p. 241201, 2008.

[109] F. Oba, A. Togo, I. Tanaka, J. Paier, and G. Kresse, "Defect energetics in ZnO: A hybrid Hartree-Fock density functional study," *Phys. Rev. B*, vol. 77, p. 245202, 2008.

[110] B. Liu and H. C. Zeng, "Room temperature solution synthesis of monodispersed single-crystalline ZnO nanorods and derived hierarchical nanostructures," *Langmuir*, vol. 20, no. 10, pp. 4196–4204, 2004.

[111] J. Elias, R. Tena-Zaera, and C. Lévy-Clément, "Electrodeposition of ZnO nanowires with controlled dimensions for photovoltaic applications: Role of buffer layer," *Thin Solid Films*, vol. 515, no. 24, pp. 8553–8557, 2007.

[112] D. Montenegro, A. Souissi, C. Martínez-Tomás, V. Muñoz-Sanjosé, and V. Sallet, "Morphology transitions in ZnO nanorods grown by MOCVD," *J. Cryst. Growth*, vol. 359, pp. 122–128, 2012.

[113] J. Yu, B. Huang, X. Qin, X. Zhang, Z. Wang, and H. Liu, "Hydrothermal synthesis and characterization of ZnO films with different nanostructures," *Applied Surf. Sci.*, vol. 257, no. 13, pp. 5563–5565, 2011.

[114] A. Rivera, J. Zeller, A. Sood, and M. Anwar, "A comparison of ZnO nanowires and nanorods grown using MOCVD and hydrothermal processes," *J. Electron. Mater.*, vol. 42, no. 5, pp. 894–900, 2013.

[115] R. Rusdi, A. A. Rahman, N. S. Mohamed, N. Kamarudin, and N. Kamarulzaman, "Preparation and band gap energies of ZnO nanotubes, nanorods and spherical nanostructures," *Powder Technol.*, vol. 210, no. 1, pp. 18–22, 2011.

[116] Z. Bao, Y. Yuan, C. Leng, L. Li, K. Zhao, and Z. Sun, "One-pot synthesis of noble metal/zinc oxide composites with controllable morphology and high catalytic performance," *ACS Appl. Mater. Interface*, vol. 9, no. 19, pp. 16417–16425, 2017.

[117] D. C. Look, J. W. Hemsky, and J. R. Sizelove, "Residual native shallow donor in ZnO," *Phys. Rev. Lett.*, vol. 82, pp. 2552–2555, 1999.

[118] D. Han, D. West, X.-B. Li, S.-Y. Xie, H.-B. Sun, and S. B. Zhang, "Impurity doping in SiO_2: Formation energies and defect levels from first-principles calculations," *Phys. Rev. B*, vol. 82, p. 155132, 2010.

[119] C. G. Van de Walle and J. Neugebauer, "First-principles calculations for defects and impurities: Applications to III-nitrides," *J. Appl. Phys.*, vol. 95, no. 8, pp. 3851–3879, 2004.

[120] C. Freysoldt, B. Grabowski, T. Hickel, J. Neugebauer, G. Kresse, A. Janotti, and C. G. Van de Walle, "First-principles calculations for point defects in solids," *Rev. Mod. Phys.*, vol. 86, pp. 253–305, 2014.

[121] L. S. Vlasenko and G. D. Watkins, "Optical detection of electron paramagnetic resonance in room-temperature electron-irradiated ZnO," *Phys. Rev. B*, vol. 71, p. 125210, 2005.

[122] K. Vanheusden, C. Seager, W. t. Warren, D. Tallant, and J. Voigt, "Correlation between photoluminescence and oxygen vacancies in ZnO phosphors," *Appl. phys. lett.*, vol. 68, no. 3, pp. 403–405, 1996.

[123] A. R. Hutson, "Hall effect studies of doped zinc oxide single crystals," *Phys. Rev.*, vol. 108, pp. 222–230, 1957.

[124] D. C. Look, D. C. Reynolds, J. Sizelove, R. Jones, C. W. Litton, G. Cantwell, and W. Harsch, "Electrical properties of bulk ZnO," *Solid State Commun.*, vol. 105, no. 6, pp. 399–401, 1998.

[125] G.-Y. Huang, C.-Y. Wang, and J.-T. Wang, "Detailed check of the LDA+U and GGA+U corrected method for defect calculations in wurtzite ZnO," *Comp. Phys. Commun.*, vol. 183, no. 8, pp. 1749–1752, 2012.

[126] A. Janotti and C. G. Van de Walle, "Oxygen vacancies in ZnO," *Appl. Phys. Lett.*, vol. 87, no. 12, p. 122102, 2005.

[127] F. Oba, S. R. Nishitani, S. Isotani, H. Adachi, and I. Tanaka, "Energetics of native defects in ZnO," *J. Appl. Phys.*, vol. 90, no. 2, pp. 824–828, 2001.

[128] P. Erhart and K. Albe, "Diffusion of zinc vacancies and interstitials in zinc oxide," *Appl. phys. lett.*, vol. 88, no. 20, p. 201918, 2006.

[129] P. Erhart and K. Albe, "First-principles study of migration mechanisms and diffusion of oxygen in zinc oxide," *Phys. Rev. B*, vol. 73, p. 115207, 2006.

[130] Y. Xu and M. Mavrikakis, "Adsorption and dissociation of O_2 on gold surfaces: effect of steps and strain," *J. Phys. Chem. B*, vol. 107, no. 35, pp. 9298–9307, 2003.

[131] G. Mills, M. S. Gordon, and H. Metiu, "The adsorption of molecular oxygen on neutral and negative aun clusters (n= 2–5)," *Chem. Phys. Lett.*, vol. 359, no. 5-6, pp. 493–499, 2002.

[132] X. Ding, Z. Li, J. Yang, J. Hou, and Q. Zhu, "Adsorption energies of molecular oxygen on Au clusters," *J. Chem. Phys.*, vol. 120, no. 20, pp. 9594–9600, 2004.

[133] B. Yoon, H. Häkkinen, and U. Landman, "Interaction of O_2 with gold clusters: molecular and dissociative adsorption," *J. Phys. Chem. A*, vol. 107, no. 20, pp. 4066–4071, 2003.

[134] L. M. Molina and B. Hammer, "Theoretical study of CO oxidation on Au nanoparticles supported by MgO(100)," *Phys. Rev. B*, vol. 69, p. 155424, 2004.

[135] B. Salisbury, W. Wallace, and R. Whetten, "Low-temperature activation of molecular oxygen by gold clusters: a stoichiometric process correlated to electron affinity," *Chem. Phys.*, vol. 262, no. 1, pp. 131–141, 2000.

[136] W. Huang, H.-J. Zhai, and L.-S. Wang, "Probing the interactions of O_2 with small gold cluster anions (Au_n^-, n = 1 - 7): Chemisorption vs physisorption," *J. Am. Chem. Soc.*, vol. 132, no. 12, pp. 4344–4351, 2010.

[137] M. Valden, X. Lai, and D. W. Goodman, "Onset of catalytic activity of gold clusters on titania with the appearance of nonmetallic properties," *Science*, vol. 281, no. 5383, pp. 1647–1650, 1998.

[138] Z. Wang, H. Fu, Z. Tian, D. Han, and F. Gu, "Strong metal–support interaction in novel core–shell Au–CeO_2 nanostructures induced by different pretreatment atmospheres and its influence on CO oxidation," *Nanoscale*, vol. 8, no. 11, pp. 5865–5872, 2016.

[139] H. Ha, H. An, M. Yoo, J. Lee, and H. Y. Kim, "Catalytic CO oxidation by CO-saturated Au nanoparticles supported on CeO_2: Effect of CO coverage," *J. Phys. Chem. C*, vol. 121, no. 48, pp. 26895–26902, 2017.

[140] H. Tang, J. Wei, F. Liu, B. Qiao, X. Pan, L. Li, J. Liu, J. Wang, and T. Zhang, "Strong metal–support interactions between gold nanoparticles and nonoxides," *J. Am. Chem. Soc.*, vol. 138, no. 1, pp. 56–59, 2015.

[141] Y. Kuwauchi, H. Yoshida, T. Akita, M. Haruta, and S. Takeda, "Intrinsic catalytic structure of gold nanoparticles supported on TiO_2," *Angew. Chem. Int. Edit.*, vol. 51, no. 31, pp. 7729–7733, 2012.

[142] S. W. Sweeney, G. Roseman, C. P. Deming, N. Wang, T. A. Nguyen, G. L. Millhauser, and S. Chen, "Impacts of oxygen vacancies on the electrocatalytic activity of $AuTiO_2$ nanocomposites towards oxygen reduction," *Int. J. Hydrogen Energy*, vol. 41, no. 40, pp. 18005–18014, 2016.

[143] M. Gajdoš, A. Eichler, and J. Hafner, "CO adsorption on close-packed transition and noble metal surfaces: trends from ab initio calculations," *J. Phys. Condens. Mat.*, vol. 16, no. 8, p. 1141, 2004.

[144] N. Lopez and J. K. Nørskov, "Catalytic CO oxidation by a gold nanoparticle: A density functional study," *J. Am. Chem. Soc.*, vol. 124, no. 38, pp. 11262–11263, 2002.

[145] N. Guo, R. Lu, S. Liu, G. W. Ho, and C. Zhang, "High catalytic activity of Au clusters supported on ZnO nanosheets," *J. Phys. Chem. C*, vol. 118, no. 36, pp. 21038–21041, 2014.

[146] Y. Duan, Z. Li, Y. Li, Y. Zhang, L. Li, and J. Li, "New insight of the mars-van krevelen mechanism of the CO oxidation by gold catalyst on the ZnO(101) surface," *Comp. Theor. Chem.*, vol. 1100, pp. 28–33, 2017.

[147] N. W. Ashcroft and N. D. Mermin, *Solid State Physics*, ch. 5, p. 86. Holt, Rinehart, and Winston, New York, 1976.

[148] W. Setyawan and S. Curtarolo, "High-throughput electronic band structure calculations: Challenges and tools," *Comp. Mater. Sci.*, vol. 49, no. 2, pp. 299–312, 2010.

[149] L. H. Thomas, "The calculation of atomic fields," *Math. Proc. Cambridge*, vol. 23, no. 5, pp. 542–548, 1927.

[150] P. Hohenberg and W. Kohn, "Inhomogeneous electron gas," *Phys. Rev.*, vol. 136, no. 3B, p. B864, 1964.

[151] P. A. M. Dirac, "Note on exchange phenomena in the thomas atom," *Math. Proc. Cambridge*, vol. 26, no. 3, p. 376385, 1930.

[152] D. M. Ceperley and B. J. Alder, "Ground state of the electron gas by a stochastic method," *Phys. Rev. Lett.*, vol. 45, pp. 566–569, 1980.

[153] D. C. Langreth and M. J. Mehl, "Beyond the local-density approximation in calculations of ground-state electronic properties," *Phys. Rev. B*, vol. 28, pp. 1809–1834, 1983.

[154] F. Jensen, *Introduction to computational chemistry.* John wiley & sons, 2017.

[155] J. P. Perdew, K. Burke, and M. Ernzerhof, "Generalized gradient approximation made simple," *Phys. Rev. Lett.*, vol. 77, pp. 3865–3868, 1996.

[156] H. J. Monkhorst and J. D. Pack, "Special points for brillouin-zone integrations," *Phys. Rev. B*, vol. 13, pp. 5188–5192, 1976.

[157] D. Vanderbilt, "Soft self-consistent pseudopotentials in a generalized eigenvalue formalism," *Phys. Rev. B*, vol. 41, pp. 7892–7895, 1990.

[158] P. E. Blöchl, "Projector augmented-wave method," *Phys. Rev. B*, vol. 50, no. 24, p. 17953, 1994.

[159] T. C. Leung, C. T. Chan, and B. N. Harmon, "Ground-state properties of Fe, Co, Ni, and their monoxides: Results of the generalized gradient approximation," *Phys. Rev. B*, vol. 44, pp. 2923–2927, 1991.

[160] A. I. Liechtenstein, V. I. Anisimov, and J. Zaanen, "Density-functional theory and strong interactions: Orbital ordering in mott-hubbard insulators," *Phys. Rev. B*, vol. 52, pp. 5467–5470, 1995.

[161] S. L. Dudarev, G. A. Botton, S. Y. Savrasov, C. J. Humphreys, and A. P. Sutton, "Electron-energy-loss spectra and the structural stability of nickel oxide: An LSDA+U study," *Phys. Rev. B*, vol. 57, pp. 1505–1509, 1998.

[162] S. Lany and A. Zunger, "Accurate prediction of defect properties in density functional supercell calculations," *Model. Simul. Mater. Sci. Eng.*, vol. 17, no. 8, p. 084002, 2009.

[163] N. E. Christensen, "Electronic structure of GaAs under strain," *Phys. Rev. B*, vol. 30, pp. 5753–5765, 1984.

[164] L.-W. Wang, "Large-scale local-density-approximation band gap-corrected GaAsN calculations," *Appl. Phys. Lett.*, vol. 78, no. 11, pp. 1565–1567, 2001.

[165] J. C. Slater, "The theory of complex spectra," *Phys. Rev.*, vol. 34, pp. 1293–1322, 1929.

[166] A. D. Becke, "A new mixing of Hartree–Fock and local density-functional theories," *J. Chem. Phys.*, vol. 98, no. 2, pp. 1372–1377, 1993.

[167] J. P. Perdew, M. Ernzerhof, and K. Burke, "Rationale for mixing exact exchange with density functional approximations," *J. Chem. Phys.*, vol. 105, no. 22, pp. 9982–9985, 1996.

[168] M. Leslie and N. Gillan, "The energy and elastic dipole tensor of defects in ionic crystals calculated by the supercell method," *J. Phys. C Solid State*, vol. 18, no. 5, p. 973, 1985.

[169] G. Makov and M. C. Payne, "Periodic boundary conditions in ab initio calculations," *Phys. Rev. B*, vol. 51, pp. 4014–4022, 1995.

[170] S. Lany and A. Zunger, "Assessment of correction methods for the band-gap problem and for finite-size effects in supercell defect calculations: Case studies for ZnO and GaAs," *Phys. Rev. B*, vol. 78, p. 235104, 2008.

[171] L. Marks, "Experimental studies of small particle structures," *Rep. Prog. Phys.*, vol. 57, no. 6, p. 603, 1994.

[172] G. Henkelman, B. P. Uberuaga, and H. Jónsson, "A climbing image nudged elastic band method for finding saddle points and minimum energy paths," *J. Chem. Phys.*, vol. 113, no. 22, pp. 9901–9904, 2000.

[173] G. Henkelman, A. Arnaldsson, and H. Jónsson, "A fast and robust algorithm for bader decomposition of charge density," *Comp. Mater. Sci.*, vol. 36, no. 3, pp. 354–360, 2006.

[174] W. Tang, E. Sanville, and G. Henkelman, "A grid-based bader analysis algorithm without lattice bias," *J. Phys. Condens. Mat.*, vol. 21, no. 8, p. 084204, 2009.

[175] A. Dannenberg, M. E. Gruner, A. Hucht, and P. Entel, "Surface energies of stoichiometric FePt and CoPt alloys and their implications for nanoparticle morphologies," *Phys. Rev. B*, vol. 80, no. 24, p. 245438, 2009.

[176] R. Cuadrado and R. Chantrell, "Interface magnetic moments enhancement of FePt-$L1_0$/MgO(001): An ab initio study," *Phys. Rev. B*, vol. 89, no. 9, p. 094407, 2014.

[177] Z. Wang, M. Saito, K. P. McKenna, L. Gu, S. Tsukimoto, A. L. Shluger, and Y. Ikuhara, "Atom-resolved imaging of ordered defect superstructures at individual grain boundaries," *Nature*, vol. 479, no. 7373, pp. 380–383, 2011.

[178] H. Li, K. Dong, Y. Peng, G. Ju, G. Chow, and J. Chen, "High coercive FePt and FePt-SiN_x(001) films with small grain size and narrow opening-up of in-plane hysteresis loop by tin intermediate layer," *J. Appl. Phys.*, vol. 110, no. 4, p. 043911, 2011.

[179] M. Yan, X. Li, L. Gao, S. Liou, D. J. Sellmyer, R. Van de Veerdonk, and K. Wierman, "Fabrication of nonepitaxially grown double-layered FePt:C/FeCoNi thin films for perpendicular recording," *Appl. Phys. Lett.*, vol. 83, no. 16, pp. 3332–3334, 2003.

[180] C. L. Johnson, E. Snoeck, M. Ezcurdia, B. Rodríguez-González, I. Pastoriza-Santos, L. M. Liz-Marzán, and M. J. Hÿtch, "Effects of elastic anisotropy on strain distributions in decahedral gold nanoparticles," *Nat. Mater.*, vol. 7, no. 2, p. 120, 2008.

[181] F. Amano, O.-O. Prieto-Mahaney, Y. Terada, T. Yasumoto, T. Shibayama, and B. Ohtani, "Decahedral single-crystalline particles of anatase titanium (IV) oxide with high photocatalytic activity," *Chem. Mater.*, vol. 21, no. 13, pp. 2601–2603, 2009.

[182] M. J. Walsh, K. Yoshida, A. Kuwabara, M. L. Pay, P. L. Gai, and E. D. Boyes, "On the structural origin of the catalytic properties of inherently strained ultrasmall decahedral gold nanoparticles," *Nano Lett.*, vol. 12, no. 4, pp. 2027–2031, 2012.

[183] X. Zhang and G. Lu, "Computational design of core/shell nanoparticles for oxygen reduction reactions," *J. Phys. Chem. Lett.*, vol. 5, no. 2, pp. 292–297, 2013.

[184] O. R. Inderwildi, D. Lebiedz, O. Deutschmann, and J. Warnatz, "Coverage dependence of oxygen decomposition and surface diffusion on rhodium (111): A DFT study," *J. Chem. Phys.*, vol. 122, no. 3, p. 034710, 2005.

[185] A. S. Barnard and L. A. Curtiss, "Predicting the shape and structure of face-centered cubic gold nanocrystals smaller than 3 nm," *ChemPhysChem*, vol. 7, no. 7, pp. 1544–1553, 2006.

[186] C. M. Wang, D. R. Baer, L. E. Thomas, J. E. Amonette, J. Antony, Y. Qiang, and G. Duscher, "Void formation during early stages of passivation: Initial oxidation of iron nanoparticles at room temperature," *J. Appl. Phys.*, vol. 98, no. 9, p. 094308, 2005.

[187] K. P. McKenna, "Gold nanoparticles under gas pressure," *Phys. Chem. Chem. Phys.*, vol. 11, no. 21, pp. 4145–4151, 2009.

[188] J. K. Burdett, T. Hughbanks, G. J. Miller, J. W. Richardson Jr, and J. V. Smith, "Structural-electronic relationships in inorganic solids: powder neutron diffraction studies of the rutile and anatase polymorphs of titanium dioxide at 15 and 295 K," *J. Am. Chem. Soc.*, vol. 109, no. 12, pp. 3639–3646, 1987.

[189] G. Charlton, P. B. Howes, C. L. Nicklin, P. Steadman, J. S. G. Taylor, C. A. Muryn, S. P. Harte, J. Mercer, R. McGrath, D. Norman, T. S. Turner, and G. Thornton, "Relaxation of TiO_2(110)-(1×1) using surface X-ray diffraction," *Phys. Rev. Lett.*, vol. 78, pp. 495–498, 1997.

[190] A. Janotti, J. B. Varley, P. Rinke, N. Umezawa, G. Kresse, and C. G. Van de Walle, "Hybrid functional studies of the oxygen vacancy in TiO_2," *Phys. Rev. B*, vol. 81, p. 085212, 2010.

[191] A. Pratt, L. Lari, O. Hovorka, A. Shah, C. Woffinden, S. P. Tear, C. Binns, and R. Kröger, "Enhanced oxidation of nanoparticles through strain-mediated ionic transport," *Nat. mater.*, vol. 13, no. 1, p. 26, 2014.

[192] H.-J. Freund, G. Meijer, M. Scheffler, R. Schlögl, and M. Wolf, "CO oxidation as a prototypical reaction for heterogeneous processes," *Angew. Chem. Int. Edit.*, vol. 50, no. 43, pp. 10064–10094, 2011.

[193] M. Usuda, N. Hamada, T. Kotani, and M. van Schilfgaarde, "All-electron *GW* calculation based on the LAPW method: Application to wurtzite ZnO," *Phys. Rev. B*, vol. 66, p. 125101, 2002.

[194] A. Calzolari and M. B. Nardelli, "Dielectric properties and raman spectra of ZnO from a first principles finite-differences/finite-fields approach," *Sci. Rep.*, vol. 3, p. 2999, 2013.

[195] S. Lany and A. Zunger, "Many-body *GW* calculation of the oxygen vacancy in ZnO," *Phys. Rev. B*, vol. 81, p. 113201, 2010.

[196] S.-H. Jeong, B.-S. Kim, and B.-T. Lee, "Photoluminescence dependence of ZnO films grown on Si(100) by radio-frequency magnetron sputtering on the growth ambient," *Appl. Phys. Lett.*, vol. 82, no. 16, pp. 2625–2627, 2003.

[197] K. McKenna and A. Shluger, "The interaction of oxygen vacancies with grain boundaries in monoclinic HfO_2," *Appl. Phys. Lett.*, vol. 95, no. 22, p. 222111, 2009.

[198] K. P. McKenna and A. L. Shluger, "Shaping the morphology of gold nanoparticles by CO adsorption," *J. Phys. Chem. C*, vol. 111, no. 51, pp. 18848–18852, 2007.

[199] R. O'Hayre and F. B. Prinz, "The air/platinum/nafion triple-phase boundary: characteristics, scaling, and implications for fuel cells," *J. Electrochem. Soc.*, vol. 151, no. 5, pp. 756–762, 2004.